UNIVERSIDAD CARLOS III DE MADRID

Escuela Politécnica Superior - Leganés

DEPARTAMENTO DE TEORÍA DE LA SEÑAL Y COMUNICACIONES

DOCTORAL THESIS

COVERING THZ GAP USING PHOTOMIXERS TECHNOLOGIES: ARRAYS AND NEW ANTENNA TOPOLOGIES

AUTHOR

Alejandro Rivera Lavado

ADVISOR

Luis Enrique García Muñoz

CO-ADVISOR

Antti Räisänen

Tesis Doctoral: COVERING THZ GAP USING PHOTOMIXERS TECHNOLOGIES: ARRAYS AND NEW ANTENNA TOPOLOGIES

Autor: Alejandro Rivera Lavado

Director/es: Luis Enrique García Muñoz
Antti Räisänen

El tribunal nombrado para juzgar la tesis doctoral arriba citada, compuesto por los doctores

Presidente: Zoya Popovic

Vocal: Cyril Luxey

Secretario: Luis Emilio García Castillo

acuerda otorgarle la calificación de

Leganés, a 15 de Diciembre de 2016

A Domingo, Elisa, Óscar, Pilar, Sergio y Sofía:
Mi familia

Dejad que camine solo,
sin cometer pecado alguno,
con muy pocos deseos,
como los elefantes en el bosque.

in memoriam: J.M.O.M.

AGRADECIMIENTOS / ACKNOWLEDGEMENTS

Mi más sincero agradecimiento a mi tutor, Luis Enrique García, por su apoyo, su ayuda y su soporte no solo durante la realización de esta tesis doctoral, sino desde que comencé en el grupo de investigación. A Daniel Segovia, por su labor en el grupo, haciendo posible esta y otras tesis. Por ser una de las mejores personas que he tenido el privilegio de conocer. A Guillermo Carpintero, por su estrecha colaboración con nosotros y su ayuda.

A mis compañeros de laboratorio: los antiguos (Edu, Montero, Doñoro, Rosa, Adrián, Nacho y el Gato) y los nuevos (Ana, Gabriel Galindo, Gabriel Santamaría, Jose, Sergio y Kerlos). A mis compañeros del grupo de investigación: Luis Emilio, Sergio, Alejandro y Magadlena Salazar.

Mayte Dávila, Milagros Gómez y María Mercedes Lorenzo: Mil gracias por vuestra ayuda y vuestra infinita paciencia.

I would like to thank the people of Millilab/SMARAD, in Aalto, for their warm welcome during all the research stays I did with them. These would not have been possible without the help and support of Antti Räisänen and Dmitri Lioubtchenko.

Esta tesis no hubiera sido posible en modo alguno sin toda una cadena humana que comenzó con dos personas. Mi más sincero agradecimiento a la Guardia Civil, a los bomberos de la Comarca de la Sagra, a Elena y a sus compañeros, al inmejorable equipo humano del Hospital Virgen de la Salud de Toledo, a mis fisios, Miguel y Felipe, y a todos aquellos que nos brindaron un caluroso apoyo cuando más hizo falta. Estoy en deuda.

Giancarlo Pastor, Salla Kauppi, Jarkko Luoma... Kiitos!! To my roommates: Edmundas Andriuška, Nils de Boeck, Igor Karpov and Glen

Tan. To Stuart Campbell (I wrote this thesis in that laptop!), Florence Van Rompuy, Ana Fuster, Chema, Marine Guiot, Rebeca Telekuda, Boris, Lotte Hufkens, Jorge Lucío and all the friends who came to our *ovenparties* during my research stay in Aalto. Al *asturiano errante*, David Fernández, y a Jorge Cantero, paisanos en Otaniemi. Thanks to Andrey Generalov, Irina Nefedova, Vasilii Semkin and Subash Khanal, the students of the Millilab/SMARAD.

Durante la realización de esta tesis tuve el privilegio de participar como timbalero de mi asociación músical (¡La Asociación Musical "Manuel de Falla" de Illescas!) en dos certamenes de bandas: el IV Certamen Nacional de Bandas de Música "Ciudad de Cullera" y el VIII Certamen Internacional de Bandas de Música "Villa de DosBarrios". Obtuvimos sendos segundos premios interpretando la banda sonora de "Conan el Bárbaro" y la obra "Alonso Quijano", respectivamente. Hemos congregado a más de mil espectadores en repetidas ocasiones. Hemos hecho conciertos líricos y temáticos: desde un especial de procesiones en la cripta de la Catedral de la Almudena hasta un especial audiovisual benéfico sobre Star Wars, con la colaboración de la legión 501 y un coro participativo. La banda de música me ha acompañado durante los grandes hitos de mi vida: los buenos y los malos. Gracias a Miguel Sanz, nuestro actual director, he tenido el privilegio de tocar bajo la batuta de Luis Cobos, ser acosenjado por Rafa Mas y el maestro Balaguer, acompañar a grandes solistas, como Pilar Tejero, María Rodríguez, Carlos Silva, Carlos London y Enrique Martínez, entre otros. Fue gracias a él que conocí a la mejor de todas las sopranos. A Jesús Illescas, nuestro anterior director, y a Paco de la Rosa, mi primer profesor de percusión. Gracias a los cuales comencé mi faceta como percusionista.

A mis churumbeles de la percu: Seves, Nevado, Samu, Alejandro, Andrés, Sergio y Luismi: ¡gracias!. A mis compañeros músicos.

A Sara por ayudarme a comenzar y a terminar esta tesis con sus consejos. A Santi. A mis rudos: Viejo, Curi y Charly. Al Ferni, Esther, Jesús, Isa, el Mario, Lydia, Fátima, el Serra, Raquel, Tamara, Esther-Vane, el Gerson, las Heavies y todo aquellos que pulularon por *La Factory*, el *Stoner* y el *Chiringo del Charly*.

CONTENTS

RESUMEN

El objetivo de esta tesis es el diseño y construcción de generadores de señal de terahercios basados en fotomezcladores de bajo coste y que funcionen a temperatura ambiente. Como se explica en la introducción, existen muchas aplicaciones potenciales a frecuencias comprendidas entre los 100 GHz y 1.000 GHz. Propuestas en el campo de la seguridad, radioastronomía y medicina, entre otros, han sido consideradas y evaluadas. Algunas de ellas han comenzado a ser explotadas comercialmente, por ejemplo, en la detección de armas y explosivos ocultos en puestos de control y seguridad. No obstante, todavía existe un nicho, el de la electrónica de consumo (comunicaciones, entretenimiento, etc), en el que las frecuencias de esta banda no son utilizadas por su alto coste.

En una primera parte, se analizan distintos tipos de antenas planares que son especialmente atractivas para ser integradas con dispositivos fotomezcladores generadores de terahercios. El efecto de los sustratos semiconductores en sus propiedades de radiación es analizado en profundidad. Así mismo, se estudian las principales familias de dispositivos fotomezcladores.

A continuación, se propone el uso de antenas dieléctricas combinadas con este tipo de fuentes. Con esto, se pretende evitar el uso de lentes dieléctricas de alto costo sin reducir drásticamente la cantidad de potencia de terahercios radiada por la fuente. Se propone un diseño de antena dieléctrica que permitiría aprovechar el ancho de banda de este

tipo de generadores, comenzando en los 50-60 GHz hasta por encima del terahercio.

Este tipo de antenas dieléctricas ofrece la posibilidad de combinar varios generadores a fin de cumplir dos objetivos: incrementar la potencia disponible y escanear electrónicamente en uno o dos planos. Se propone el uso de nanotubos de carbono para la realización de desfasadores controlados electrónicamente, componente imprescidible para arrays de escaneo electrónico.

Finalmente, se estudia la capacidad de este tipo de antenas de actuar como acoplos de campo cercano en resonadores. Como ejemplo de aplicación, se propone su uso en un receptor de terahercios cuya sensibilidad, no limitada por el ruido térmico, llega al límite cuántico, esto es, la detección de fotones de terahercios.

ABSTRACT

The objective of this thesis is the design and manufacturing of room-temperature cost-affordable terahertz sources based on photomixing. As explained in the preface, there are many potential applications for frequencies between 100 GHz and 1 THz. Many of them, specially in the fields of security, radioastronomy, and medicine have been deeply studied and evaluated. Some of them have led to already available commercial products, e.g. in hidden weapons and explosives detection in security controls. Nevertheless, there are many consumer-oriented applications related with communication and entertainment industry that cannot be implemented because of the actual costs of terahertz systems.

Firstly, some planar antenna topologies appealing for photomixing sources are shown. The effect of the semiconductor substrates on its radiation properties is theoretically analyzed. Also, the main families of terahertz photomixing sources are described.

Secondly, the use of dielectric antennas in combination with photomixing sources is proposed. This allows to reduce costs without a drastic decrement of the radiated power. An ultra-wideband design that could allow us to take advantage of the photomixers bandwidth (from 50-60 GHz up to beyond the terahertz) is presented.

Thirdly, the combination of many sources in array configurations is proposed. It allows us to accomplish two objectives: increasing the

available terahertz power and 1D or 2D beam steering. A novel phase shifter made of carbon nanotubes is presented, since such component is critical for the development of a electronically steerable array.

Finally, the use of this family of dielectric antennas as a near field coupler for dielectric resonators is studied. A room temperature photon-counting teraherz receiver is proposed as an example of application. This receiver is limited only by a quantum limit, which gives the theoretical maximum achievable sensitivity for a receiver.

LIST OF TERMS

AE	antenna emitter
AEA	antenna emitter array
APD	avalanche photodiode
AUT	antenna under test
CMB	cosmic microwave background
CNC	computerized numerical control
CNR	carrier-to-noise
CNT	carbon nanotube
CVD	chemical vapor deposition
CW	continuous wave
DFG	difference frequency generation
DRW	dielectric rod waveguide
ESF	European Science Foundation
FF	far field
FSR	free spectral range
FWHM	full width at half maximum

GPIB	general purpose instrumentation bus
GREMA	Radiofrequency, Electromagnetics, Microwaves & antennas
GUI	graphical user interface
HF	hydrogen fluoride
HHI	Heinrich Hertz Institute
LAE	large area emitter
LAN	local area network
LAQD	large area quasi dipole
LT	low temperature
MBE	molecular beam epitaxy
MEMS	microelectromechanical systems
MVNA	millimeter vector network analyzer
NEP	noise equivalent power
NF	near field
PD	photodiode
PM	polarization maintaining
PO	physical optics
QCL	quantum-cascade laser
RIN	relative intensity noise
RTD	resonant tunneling diode
SEM	scanning electron microscope
SFG	sum frequency generation
SIS	superconductor-insulator-superconductor
SLL	sidelobe level
SMD	surface-mount device
SP	stationary phase
TCP	transmission control protocol
TE	transverse electric
TEC	thermo-electric cooler
TEM	transverse electromagnetic mode
TIR	total internal reflection

TM	transverse magnetic
USB	universal serial bus
UTC	uni-traveling-carrier
VNA	vector network analyzer
WGM	whispering gallery mode
WGMR	whispering gallery mode resonator
WPAN	wireless personal area network
XPD	cross-polar discrimination

PREFACE

I always wanted to be a researcher. Since I was a child, I enjoyed disassembling and re-assembling things, specially electronic devices. I remember how astonished I was in the way things are designed to solve problems and needs for the mankind. Every artificial object around us is the result of a creative process, which starts in a necessity or a desire. Curiosity can also become a powerful need that must be satisfied when the pruritus raises. Applied technology to sciences has seemed to me a consequence of the human nature which pushes us beyond known boundaries. I was lucky to be born in a time where both Sci-Fi inspiration and discarded consumer electronics started to be universally available as boosters for my motivation.

My affiliation with Carlos III University of Madrid Radiofrequency, Electromagnetics, Microwaves & antennas (GREMA) research group started in 2007, when I offered helping on “bringing to recycle” old and broken Hewlett-Packard instrumentation equipments. Those were components of two HP8410 modular network analyzers. Now, they are part of a modest personal collection which includes scopes, generators, spectrum analyzers, a logic analyzer, power sources, a vector signal analyzer, programmers, among other tools. They still serve me well for my own projects: a 2.5 km rural data radio link, a fully-automated orchard with moisture data gathering, ham experiments, etc. Eventually, they were useful during the experimentation carried out for this thesis.

Collecting all these old devices pointed me somehow as a candidate for a grant on which I started manufacturing RF circuits and antennas, both for teaching an research. After my bachelor studies, I enrolled as a Master and, afterwards, as a Ph.D student in the field of (initially) radiastronomy and (finally) terahertz antennas. Potential of terahertz waves [1, 2] in medical-related applications [3–8] aimed me to go into details of power generation. Nowadays, there is one mayor issue in this promising research field: the lack of high-power, continuous wave (CW), coherent, compact and room-temperature THz sources.

0.1 State of art

Fig. 1 summarizes the state-of-the-art in power generation in the so called "terahertz gap", it means, frequencies starting from 100 GHz to 10 THz. There are a wide variety of technologies in both microwave and infrared frequencies. Existent technologies for both regions of the spectrum cannot operate in the THz band without a significant reduction in power and/or efficiency.

At lower region of THz band, solid state devices, such as Gunn diodes, IMPATT diodes and resonant tunneling diodes (RTDs) have roll-offs of $1/f^2$ (straight function $Pf^2 = cte$ on Fig. 1) [9–15]. Frequency multipliers [10, 16] can improve the power lever but they are extremely inefficient. Starting for already available sources at tens of GHz they reach the THz range by series of doublers or triplers [2, 11, 17]. By increasing the number of concatenated frequency multipliers efficiency drastically decreases [16, 18]. Furthermore, these sources have a limited bandwidth and a poor noise performance. In a ideal frequency multiplier, the minimum carrier-to-noise (CNR) degradation ΔCNR in dB is [16]

$$\Delta CNR = 20log_{10}(n) \tag{1}$$

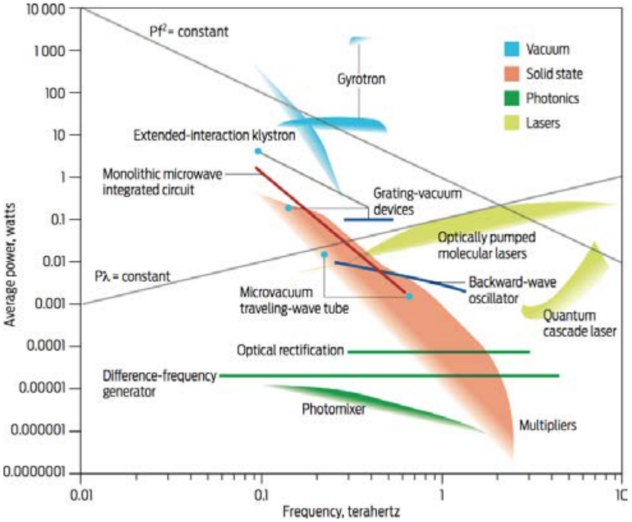

Figure 1: Main THz sources and their output power [9].

where n is the frequency multiplication factor. This makes this technology dependent on cryostat systems for applications where the noise level is critical.

On the other hand, lasers and optical down converters has been proposed as an approach from the higher region of the THz gap. Since there are not available materials with adequately small band gap energies (4.14 meV at 1 THz), unless considering artificial engineered materials [19, 20], only quantum-cascade lasers (QCLs) [19] or CO_2 [2, 21] lasers are able to reach terahertz frequencies with power levels of few hundreds of milliwatts [19]. For CO_2 lasers, frequency is limited both by resonant frequencies of the molecules and laser cavity. An CW output power above 1 W has been achieved [22].

QCLs can operate either in a pulsed or CW regime at cryogenic temperatures covering a frequency range of 0.84 THz to 5 THz [23–25]. Operation temperatures of 200°K at 3.2 THz has been achieved [26]. A QCL working at room temperature achieved a power 8.5 μW at 4 THz [27]. Tunability is usually limited by the QCL chip itself [28].

Optical down converters are able to achieve wide THz bandwidth [29].

Nonlinear crystals are used for obtaining tunable monochromatic sources with high spectral resolution by different techniques, such as difference frequency generation (DFG) or THz parametric oscillators [30–32]. It is also possible to generate THz waves by optical rectification. Achieved power level is low, but high tunability is feasible [29].

This thesis is devoted to CW photomixer-based terahertz sources. Despite their achieved power level is lower than other technologies (of few μW as seen in Fig. 1) they have appealing characteristics that turn photomixing into an enabling technology for many applications inside the THz gap. They can operate at room temperature [2], either in CW or pulsed regimes. They are potentially broadband, being able to achieve scanning ranges from 60 GHz to 1.8 THz what makes them suitable for wideband spectroscopy applications [33]. Even ranges of more than 5 octaves has been reported [34]. Since they are low noise sources [35] they are appealing for low-noise broadband local oscilators, as required in radioastronomy applications [35] and mm- and sub-mm wave high-rate data transceivers [36]. A superconductor-insulator-superconductor (SIS) receiver with a noise temperature of 170°K at 450 GHz is reported in [35]. Low-range wireless communications at data rates as high as 16 Gb/s (error-free) in the 300 GHz band has been reported [37] using uni-traveling-carrier (UTC) photodiodes (PDs). Low-cost opens the door to many consumer-oriented applications, such as local area networks (LANs), wireless personal area networks (WPANs), device-to-device communications, nano cells of ultra-high data rate, chip-to-chip communication, among others. Regulation and standardization efforts have been already initiated for this frequency range [36, 38].

The main goal of this thesis is to achieve a cost-affordable CW terahertz source that could enable applications mentioned above.

0.2 Introduction to photomixing

In a photomixer-based terahertz source (Fig. 2), two lasers of different wavelengths λ_1 and λ_2 and powers P_1 and P_2 are focused in the semiconductor device. Assuming $\lambda_1 < \lambda_2$ their frequencies can be expressed as $\nu_1 = \nu_0 + \nu_{THz}/2$ and $\nu_2 = \nu_0 - \nu_{THz}/2$, respectively, being ν_0 the central frequency and ν_{THz} the frequency difference that can be calculated with the following expression

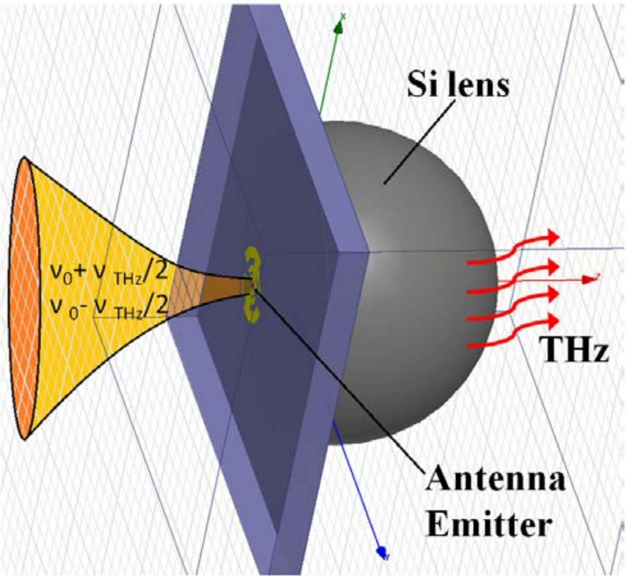

Figure 2: Schematic picture of an antenna emitter (AE). The two lasers beams (orange) are focused onto the small semiconductor device between the arms of a log-periodic antenna (pear). The THz radiation (red) is emitted into the wafer (blue-violet), transmitted into the hyper-hemispherical lens (gray) and, finally, radiated into the air.

$$\nu_{THz} = \frac{c(\lambda_2 - \lambda_1)}{\lambda_1 \lambda_2} \tag{2a}$$

$$\nu_0 = \frac{c(\lambda_2 + \lambda_1)}{2\lambda_1 \lambda_2} \tag{2b}$$

The lasers frequency ν must satisfy the inequality $\nu < E_G/h$ for being able to generate electron-hole pairs. E_G is the band gap energy and it depends on the material used for the photonics device. Table 1 shows an example of materials and their respective gap energies [39]. Minimum wavelength and frequency is calculated for each band gap energy. Relative permittivity ϵ_r is also provided [40–44]. These suitable for affordable 1550 nm telecom lasers are specially appealing, specially for low-cost electronics. h is the Planck constant.

Material	$E_G[eV]$	$\lambda[nm]$	$\nu[THz]$	ϵ_r
Si	1.11	1117	268.6	11.9
Ge	0.66	1879	159.7	16
InP	1.27	976	307.4	12.4
GaAs	1.42	874	343.3	13.1
InAs	0.36	3444	87.1	14.6
AlAs	2.15	577	519.9	10.1
LT-InAlAs/InGaAs	0.8	1550	193.5	10 - 14.6
$In_{0.53}Ga_{0.47}As$	0.74	1677	178.9	13.6

Table 1: List of materials and their band gap energies E_G. Equivalent wavelengths λ, frequencies ν and relative permitttivities ϵ_r are also shown

The lasers fields $\vec{E}_1(t)$ and $\vec{E}_2(t)$ are overlapped inside the device. Total field $\vec{E}_{tot}(t)$ can be expressed as

$$\begin{aligned} \vec{E}_{tot}(t) &= \vec{E}_1(t) + \vec{E}_2(t) \\ &= E_{1,0} e^{i(\omega_0 + \omega_{THz}/2)t} \hat{\rho}_1 + E_{2,0} e^{i(\omega_0 - \omega_{THz}/2)t - i\varphi} \hat{\rho}_2 \end{aligned} \tag{3}$$

where $E_{i,0}$ are field strengths, $\omega_i = 2\pi\nu_i$, are angular frequencies, φ is the relative phase between lasers, and $\hat{\rho}_i$ the normalized polarization vector. Therefore, the total optical intensity is

$$\left|\vec{E}_{tot}(t)\right|^2 = E_{1,0}^2 + E_{2,0}^2 + 2E_{1,0}E_{2,0}cos(\beta)cos(\omega_{THz}t + \varphi) \tag{4}$$

where $\beta = cos^{-1}\left|\hat{\rho}_1 \bullet \hat{\rho}_2\right|$ is the angle between both lasers polarizations. Typically, a polarization controller is used in at least one of the laser sources for maximizing $cos(\beta)$.

Power and field strength can be related inside the device with the electric semiconductor susceptibility χ according to the following expression

$$P_{tot}(t) = \epsilon_0 \sum_{n=1}^{\infty} \chi^{(n)} \left|E_{tot}(t)\right|^n \tag{5}$$

For THz power generation, the second order non-linearity $\chi^{(2)}$ of the device material is commonly used, so that $P_{tot}(t)$ has a component at the difference frequency ν_{THz}. Total optical power P_{opt} is given then by

$$P_{opt} = P_1 + P_2 + 2\sqrt{P_1P_2}cos(\beta)cos(\omega_{THz}t + \varphi) \tag{6}$$

Assuming loss-less semiconductor and a perfect absorption of the incident light, the total optical power leads to a photocurrent that, in ideal conditions, can be calculated as follows

$$I_{pd}^{id}(t) = \frac{eP_{opt}(t)}{h\nu_0} = I_{DC}^{id} + I_{THz}^{id} \tag{7}$$

e is the elementary charge. I_{DC}^{id} and I_{THz}^{id} are DC and AC components of the generated photocurrent, respectively. According to Eqs. (6)

and (7) they can be expressed as follows

$$I_{DC}^{id} = \frac{e(P_1 + P_2)}{h\nu_0} \tag{8a}$$

$$I_{THz}^{id} = \frac{2e\sqrt{P_1 P_2} cos\beta}{h\nu_0} \tag{8b}$$

The generated THz photocurrent I_{THz}^{id} is usually fed into a suitable antenna. The integration of a photomixer and a antenna is referred as AE. Considering a radiation resistance R_A it is possible to calculate the ideal level of radiated THz power P_{THz}^{id}

$$P_{THz}^{id} = \frac{1}{2} R_A \left(\frac{e}{h\nu_0} \right)^2 P_{opt} \tag{9}$$

Typically, the active region on which photocarriers are generated corresponds to an external thin volume. Planar antennas are printed in the surface, around the photomixer. Due to its high permittivity, most of this power is radiated into the semiconductor substrate. It is very common that chip thickness, imposed by external factors, such as manufacture process, packaging or economic issues, is in the range of several wavelengths. In such scenario most of the generated power is trapped inside the chip. This is usually mitigated by adding a high-permittivity dielectric lens, typically a silicon lens, down the AE (Fig. 2). Despite being efficient in terms of terahertz power radiated into the air it may not be suitable for low-cost applications, since lenses are usually in the hundreds of euros.

0.3 Outline

In this thesis, first chapters offers an approach of difficulties found when designing and using photomixing terahertz sources. First two chapters are focused in the THz power generation, both terahertz antennas and photomixing devices are considered. In Chapter 1, the performance of planar antennas printed on high-permittivity dielectric substrates is studied. Difficulties on simulating the electromagnetic problem for finite and semi-infinite substrates are discussed. Chapter 2 provides an overview of different kinds of optoelectronic terahertz sources inside the scope of this work. A brief explanation of the theoretical background of each type is provided. Chapter 3 explains all measurement setups used in the experimental part of this thesis. Both coherent and non-coherent 1550nm photomixing setups are constructed for evaluating radiation pattern measurement of the assembled terahertz sources. Assembling of an AE is also explained.

An alternative to expensive and electrically large silicon lenses is proposed in the second part of this thesis. dielectric rod waveguide (DRW) antennas are introduced in Chapter 4. Their performance in array configuration is analyzed in Chapter 5. The coherent combination of an arbitrary large number N of optoelectronic sources allows to accomplish two important goals: to increase the radiated power by N^2 and to enable electronic steerable antenna arrays.

Finally, an application on which DRW antennas beats silicon lenses is proposed in Chapter 6. Rods antennas are proposed as a near field (NF) couplers to dielectric resonators. A photon-counting THz receiver based on this application is then described, despite other applications, such as high-sensitivity sensors, THz switches, etc. are possible.

0.4 References

[1] Y.-S. Lee, *Principles of Terahertz Science and Technology.* Springer Science & Business Media, 2009, vol. 170.

[2] P. H. Siegel, “Terahertz technology,” *IEEE Transactions on Microwave Theory and Techniques*, vol. 50, no. 3, pp. 910–928, 2002.

[3] J.-H. Son, “Terahertz electromagnetic interactions with biological matter and their applications,” *Journal of Applied Physics*, vol. 105, no. 10, p. 102033, 2009.

[4] J.-H. Son, “Terahertz bio-imaging for medical applications,” in *Conference on Lasers and Electro-Optics/Pacific Rim.* Optical Society of America, 2013.

[5] K. W. Kim, H. Kim, J. Park, J. K. Han, and J.-H. Son, “Terahertz tomographic imaging of transdermal drug delivery,” *IEEE Transactions on Terahertz Science and Technology*, vol. 2, no. 1, pp. 99–106, 2012.

[6] L. Young, M. Gradziel, W. Lanigan, C. Sullivan, J. Murphy, R. Mahon, R. May, N. Trappe *et al.*, “Millimetre-wave and terahertz imaging systems with medical applications,” in *Joint 31st International Conference on Infrared Millimeter Waves and 14th International Conference on Teraherz Electronics, 2006. IRMMW-THz 2006.*, 2006, pp. 371–371.

[7] X. Yin, B. W.-H. Ng, J. A. Zeitler, K. L. Nguyen, L. F. Gladden, and D. Abbott, “Local computed tomography using a THz quantum cascade laser,” *IEEE Sensors Journal*, vol. 10, no. 11, pp. 1718–1731, 2010.

[8] K. Humphreys, J. Loughran, M. Gradziel, W. Lanigan, T. Ward, J. Murphy, and C. O’sullivan, “Medical applications of terahertz imaging: a review of current technology and potential applications in biomedical engineering,” in *Engineering in Medicine and Biology Society, 2004. IEMBS’04. 26th Annual International Conference of the IEEE*, vol. 1. IEEE, 2004, pp. 1302–1305.

[9] C. Armstrong, “The truth about terahertz,” *IEEE Spectrum*, vol. 9, no. 49, pp. 36–41, 2012.

[10] D. M. Pozar, *Microwave Engineering.* John Wiley & Sons, 2009.

[11] T. W. Crowe, W. L. Bishop, D. W. Porterfield, J. L. Hesler, and R. M. Weikle, "Opening the terahertz window with integrated diode circuits," *IEEE Journal of Solid-State Circuits*, vol. 40, no. 10, pp. 2104–2110, 2005.

[12] R. J. Trew, "High-frequency solid-state electronic devices," *IEEE Transactions on Electron Devices*, vol. 52, no. 5, pp. 638–649, 2005.

[13] H. Eisele, "InP gunn devices for 400-425 GHz," *Electronics Letters*, vol. 42, no. 6, pp. 358–359, 2006.

[14] H. Eisele and R. Kamoua, "Submillimeter-wave InP Gunn devices," *IEEE Transactions on Microwave Theory and Techniques*, vol. 52, no. 10, pp. 2371–2378, 2004.

[15] N. Orihashi, S. Suzuki, and M. Asada, "One THz harmonic oscillation of resonant tunneling diodes," *Applied Physics Letters*, vol. 87, no. 23, p. 233501, 2005.

[16] S. A. Maas, *Nonlinear Microwave and RF Circuits.* Artech House, 2003.

[17] A. Maestrini, J. Bruston, D. Pukala, S. Martin, and I. Mehdi, "Performance of a 1.2 THz frequency tripler using a GaAs frameless membrane monolithic circuit," in *IEEE MTT-S International Microwave Symposium Digest (MTT)*, vol. 3. IEEE, 2001, pp. 1657–1660.

[18] J. Manley and H. Rowe, "Some general properties of nonlinear elements-part i. general energy relations," *Proceedings of the IRE*, vol. 44, no. 7, pp. 904–913, 1956.

[19] B. S. Williams, "Terahertz quantum-cascade lasers," *Nature Photonics*, vol. 1, no. 9, pp. 517–525, 2007.

[20] A. Davies, E. Linfield, and M. Johnston, "The development of terahertz sources and their applications," *Physics in Medicine and Biology*, vol. 47, no. 21, p. 3679, 2002.

[21] S. Jacobsson, "Optically pumped far infrared lasers," *Infrared Physics*, vol. 29, no. 5, pp. 853–874, 1989.

[22] G. Dodel, “On the history of far-infrared (fir) gas lasers: Thirty-five years of research and application,” *Infrared Physics & Technology*, vol. 40, no. 3, pp. 127–139, 1999.

[23] B. S. Williams, S. Kumar, Q. Hu, and J. L. Reno, “High-power terahertz quantum cascade lasers,” in *Conference on Lasers and Electro-Optics*. Optical Society of America, 2006, p. CTuT2.

[24] C. Worrall, J. Alton, M. Houghton, S. Barbieri, H. E. Beere, D. Ritchie, and C. Sirtori, “Continuous wave operation of a superlattice quantum cascade laser emitting at 2 THz,” *Optics Express*, vol. 14, no. 1, pp. 171–181, 2006.

[25] C. Walther, M. Fischer, G. Scalari, R. Terazzi, N. Hoyler, and J. Faist, “Quantum cascade lasers operating from 1.2 to 1.6 THz,” *Applied Physics Letters*, vol. 91, no. 13, p. 131122, 2007.

[26] S. Fathololoumi, E. Dupont, C. Chan, Z. Wasilewski, S. Laframboise, D. Ban, A. Mátyás, C. Jirauschek, Q. Hu, and H. Liu, “Terahertz quantum cascade lasers operating up to 200 K with optimized oscillator strength and improved injection tunneling,” *Optics Express*, vol. 20, no. 4, pp. 3866–3876, 2012.

[27] Q. Lu, N. Bandyopadhyay, S. Slivken, Y. Bai, and M. Razeghi, “Room temperature single-mode terahertz sources based on intracavity difference-frequency generation in quantum cascade lasers,” *Applied Physics Letters*, vol. 99, no. 13, p. 131106, 2011.

[28] G. Scalari, C. Walther, M. Fischer, R. Terazzi, H. Beere, D. Ritchie, and J. Faist, “THz and sub-THz quantum cascade lasers,” *Laser & Photonics Reviews*, vol. 3, no. 1-2, pp. 45–66, 2009.

[29] B. Ferguson and X.-C. Zhang, “Materials for terahertz science and technology,” *Nature Materials*, vol. 1, no. 1, pp. 26–33, 2002.

[30] M. Tonouchi, “Cutting-edge terahertz technology,” *Nature Photonics*, vol. 1, no. 2, pp. 97–105, 2007.

[31] K. Suizu and K. Kawase, “Monochromatic-tunable terahertz-wave sources based on nonlinear frequency conversion using lithium niobate crystal,” *IEEE Journal of Selected Topics in Quantum Electronics*, vol. 14, no. 2, pp. 295–306, 2008.

[32] W. Shi, Y. J. Ding, N. Fernelius, and K. Vodopyanov, “Efficient, tunable, and coherent 0.18–5.27-THz source based on GaSe crystal,” *Optics Letters*, vol. 27, no. 16, pp. 1454–1456, 2002.

[33] A. Roggenbuck, H. Schmitz, A. Deninger, I. C. Mayorga, J. Hemberger, R. Güsten, and M. Grüninger, “Coherent broadband continuous-wave terahertz spectroscopy on solid-state samples,” *New Journal of Physics*, vol. 12, no. 4, p. 043017, 2010.

[34] E. Brown, K. McIntosh, K. Nichols, and C. Dennis, “Photomixing up to 3.8 THz in low-temperature-grown GaAs,” *Applied Physics Letters*, vol. 66, no. 3, pp. 285–287, 1995.

[35] I. C. Mayorga, P. M. Pradas, E. Michael, M. Mikulics, A. Schmitz, P. van der Wal, C. Kaseman, R. Gusten, K. Jacobs, and M. Marso, “Terahertz photonic mixers as local oscillators for hot electron bolometer and superconductor-insulator-superconductor astronomical receivers,” *Journal of Applied Physics*, vol. 100, no. 4, p. 043116, 2006.

[36] T. Nagatsuma, “Terahertz communications: Past, present and future,” in *40th International Conference on Infrared, Millimeter, and Terahertz waves (IRMMW-THz), 2015*, 2015, pp. 1–2.

[37] H.-J. Song and T. Nagatsuma, “Present and future of terahertz communications,” *IEEE Transactions on Terahertz Science and Technology*, vol. 1, no. 1, pp. 256–263, 2011.

[38] T. Kürner and S. Priebe, “Towards THz communications-status in research, standardization and regulation,” *Journal of Infrared, Millimeter, and Terahertz Waves*, vol. 35, no. 1, pp. 53–62, 2014.

[39] C. Kittel, *Introduction to Solid State Physics.* Wiley, 2005.

[40] K. K. Ng, *Complete Guide to Semiconductor Devices.* McGraw-Hill, 1995.

[41] S. M. Sze and K. K. Ng, *Physics of Semiconductor Devices.* John wiley & sons, 2006.

[42] K. Brennan and K. Hess, “High field transport in GaAs, InP and InAs,” *Solid-State Electronics*, vol. 27, no. 4, pp. 347–357, 1984.

[43] S. Adachi, “Material parameters of in1- xgaxasyp1- y and related binaries,” *Journal of Applied Physics*, vol. 53, no. 12, pp. 8775–8792, 1982.

[44] J. Singh, *Physics of Semiconductors and their Heterostructures*. McGraw-Hill College, 1993.

CHAPTER 1

PLANAR ANTENNAS PRINTED ON DIELECTRIC SUBSTRATES

In this chapter, the performance of planar antennas lying on high-permittivity substrates is studied. First, the antenna topologies used in this thesis are described. Then, the effect of both semi-infinite and slab substrates are considered. Finally, the use of silicon lenses is considered.

In most scenarios, the generated THz power must be either radiated into free space or coupled to some structure, such as waveguides or resonators. As anticipated in the preface, most of the power is trapped in the high permittivity substrate due to the generation of unwanted surface modes [1]. It means that low overall efficiencies are achieved. This cannot be avoided by moving to lower permittivities materials due to the manufacturing restrictions: low temperature (LT) InGaAs/InGaAs multilayer stacks or $\mathrm{In_{1-x}Ga_xAs}$ ternally alloys requires lattice matching, so only a proper substrate, such as InP, must be chosen.

This issue is addressed by studying the performance of planar antennas printed in the surface of dielectrics. Hertzian dipoles parallel and normal to the interface are chosen for simplicity. First, semi-infinite substrates are studied. Then, infinite dielectric slab of finite thickness is considered as a substrate. Finally, the classical solution to this problem, silicon lenses, will be studied. A simulated estimation of efficiency is provided for comparison purposes with the proposed alternative in Chapter 4.

Despite considering dipoles in this chapter, this thesis make emphasis in the potential broadband of photomixing sources. Because of this, next chapters consider broadband antennas, such a bow tie, log-periodic and log-spiral instead of a dipole.

1.1 THz planar antennas

Many antenna topologies had been proposed and successfully used in the mm-wave range. They can be classified in two main groups: resonant and broadband antennas. This thesis focuses on broadband topologies, since with them it is possible to take advantage of the photomixing-based terahertz sources working band. Self-complementary topologies are of special interest to this application. They are antennas where the metallic and non-metallic areas have the same size and shape. Each one can be defined by rotation of the other. They have a frequency independent impedance, which can be calculated by

$$Z_{in} = \frac{Z_0}{2} \tag{1.1}$$

where Z_0 is the intrinsic impedance of the medium surrounding the antenna ($Z_0 = \eta = 120\pi\ \Omega$ for the vacuum). This family of antennas can achieve a bandwidth of more than one octave [2].

Despite they are resonant, dipoles are considered in this study because of their simplicity, which makes them convenient for theoretical discussions. Below, the antenna topologies used on this thesis are introduced.

- Dipole antennas

This is the most used resonant antenna in the terahertz band. An example of this topology is shown in Fig. 1.1. An RF filter prevents the THz power from going to the biasing pads.

For maximizing the radiated power, conjugate matching of antenna and photomixer impedances must be achieved for the dipole resonant frequency. The capacitance of the device can be compensated by choosing prover values for L_1 and L_2. Both the width and the gap of the dipole can also be adjusted to equate real parts of both impedances.

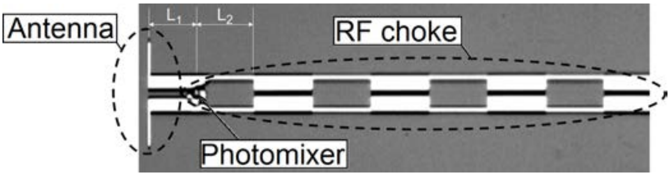

Figure 1.1: scanning electron microscope (SEM) picture of a dipole-based AE. The antenna, the RF choke and the photomixer are marked.

- Bow-tie antennas

The bow-tie antenna topology is sketched in Fig. 1.2. The width of its arms increase proportionally with the distance to the center. It becomes self-complementary when $\alpha = 90°$. Its minimum working frequency is related to the radius R_{OUT}. Upper frequency limitations are due to the gap size. For antenna emitters, this is related with the photomixer size, which is fitted in the antenna gap.

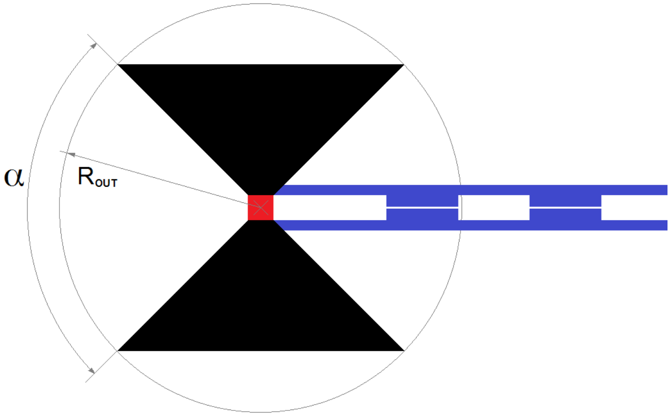

Figure 1.2: Sketch of a bow-tie AE. The antenna (black), the RF choke (blue) and the photomixer (red) are shown.

- Log-spiral antennas

Log-spiral antennas (Fig. 1.3) are self-complementary antennas when designed with specific parameters such as the proper arm lenght and width. The most important characteristic of these antennas is the frequency-independent theoretical input impedance [2].

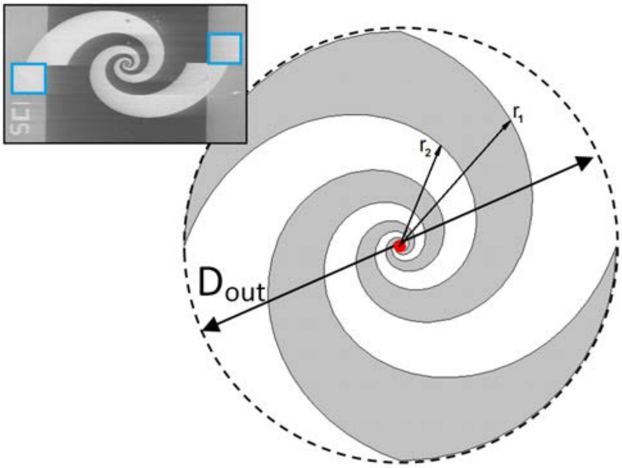

Figure 1.3: Sketch of a log-spiral AE. The antenna (grey), and the photomixer (red) are shown. The inset shows a manufactured log-spiral of diameter $D_{out} = 1.30$ mm. Biasing pads are marked in the inset (blue).

Obviously, a log-spiral should be of infinite extent to be rigorously self-complementary. Due to practical reasons they are always truncated, which leads to a frequency-dependent input impedance, both in the high and low band. At high frequencies, the limitations is due to the photomixer dimensions, which determines the truncation of the spiral. The diameter D_{out} has effects on the low frequency limit, where the size of the element is comparable to the wavelength and the energy spreads throughout all the structure. This lower frequency is determined approximately by $\lambda = D_{out}$. By increasing the arms beyond the bandwidth requirements, it is possible to use them as biasing pads (Fig. 1.3 inset, blue), which avoids the need of an RF choke.

A log-spiral arm surface can be determined by an inner (r_1) and an outer (r_2) radius

$$r_1 = ke^{a\varphi}, r_2 = ke^{a(\varphi-\delta)} \tag{1.2}$$

while sweeping the angle φ from φ_{min} to φ_{max}. Both limits define the spiral truncation points. The angle δ determines the arm width. a and k are constants, which controls the growth rate and the size of the terminal region, respectively.

- Log-periodic antennas

The log-periodic antenna [3, 4] has a log-periodic circular-toothed structure (Fig. 1.4). For the self-complementary case, tooth and bow angles (α and β, respectively) are equal. The ratio of the successive teeth, defined as $R_t = R_{n+1}/R_n$, is 0.5, while the size ratio of the tooth and anti-tooth $R_a = r_n/R_n$ is equal to $\sqrt{0.5}$.

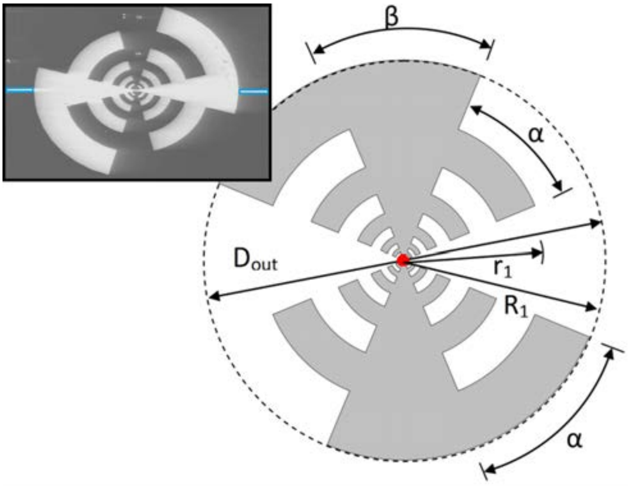

Figure 1.4: Sketch of a log-spiral AE. The antenna (grey), and the photomixer (red) are shown. The inset shows a SEM picture of a log-spiral of diameter $D_{out} = 0.74$ mm. Biasing lines are marked in the inset (blue).

Log periodic antennas possess a non-constant impedance, polarization and radiation pattern. On the other hand, they can achieve a high directivity over a wide frequency range. This topology is specially interesting for this thesis, since it is linear-polarized, which makes them suitable for exciting the fundamental mode in DRW antennas (see Chapter 4).

There are other types of antennas which are out of the scope of this analysis, such as dual-dipoles [5, 6], meander-dipoles [7], full-wavelength four-leaf-clover [8], its equivalent in a slot topology, among others.

1.2 Hertzian dipole lying on semi-infinite substrate

In this section, the radiation pattern of an electric dipole placed close to the interface between two semi-infinite different media is analytically obtained. Both are assumed to be isotropic, homogeneous and lossless dielectrics. When XY plane defines the interface, $z > 0$ corresponds to the medium with refractive index n_1 and $z < 0$ with n_2. Medium 1 corresponds to the semiconductor substrate ($n_1 = n_{SC} = \sqrt{\varepsilon_{SC}}$) and medium 2 corresponds to air ($n_2 = n_{AIR} \approx 1$).

Two different configurations, the vertical dipole (normal to the interface) and the horizontal one (parallel to the YX plane), are considered in Subsections 1.2.1 and 1.2.2, respectively. All other possible dipole orientations can be solved by superposition of these canonical cases.

1.2.1 Vertical dipole

The radiation intensity of a vertical dipole embedded in an infinite medium $U_v(\theta)$ is obtained with the following equation [9, 10]

$$U_v(\theta) = U_0 \sin^2(\theta) \tag{1.3}$$

where U_0 is the amplitude, which linearly depends on the THz radiated power P_{THz}^{id} calculated with equation (9).

Fig. 1.5 sketches the geometry of the hertzian vertical dipole embedded in a semi-infinite substrate. The distance between the dipole and the interface is z_0, which is assumed to be zero for this analysis. The generated fields are decomposed in both p- and s- polarized components. For this antenna orientation, s- component is zero. When evaluating the radiation intensity for all directions, it is determined where there is both reflected and transmitted rays in the interface (blue ray on Fig. 1.5) or not (red and black). Next, the calculation of the radiation intensity for z<0 (power radiated into the air) and z>0 (power radiated into the substrate) is summarized. The complete mathematical procedure is presented in [10–12].

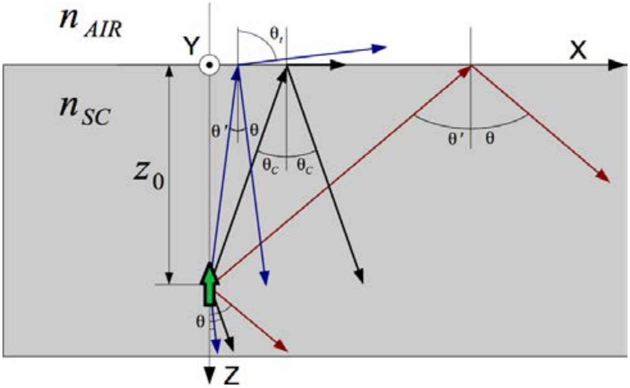

Figure 1.5: Direct, reflected and transmitted beams for a vertical dipole at a distance z_0 below the interface to air. Since this problems has radial symmetry only is necessary to consider one plane normal to the interface. For $0 < \theta' < \theta_C$ a transmitted beam exists (blue), for $\theta_C < \theta' < \pi/2$ total reflection occurs (red). $\theta' = \theta_C$ caso is also shown (black).

- Power radiated into the air

All the power radiated in the semiconductor towards the interface under the solid angle $d\Omega = \sin\theta d\theta d\phi$ is related to the power transmitted into the air under the solid angle $d\Omega_t = \sin\theta_t d\theta_t d\phi$ (blue ray in Fig. 1.5)

$$U_{AIR,v}(\theta_t)\Big|_p \cdot d\Omega_t = T(\theta)\Big|_p \cdot U_v(\theta)\Big|_p \cdot d\Omega \tag{1.4}$$

where $T(\theta)\Big|_p$ is the transmittance fo the p- polarized wave

$$T(\theta)\Big|_{p} = \frac{4\,\cos(\theta)\cos(\theta_t)}{\big(cos(\theta) + n_{_{SC}}\cos(\theta_t)\big)^2} \tag{1.5}$$

and the refraction angle θ_t is calculated with the Snell law

$$\theta_t = \arcsin(n_{_{SC}} sin(\theta')) \tag{1.6}$$

The angular distribution of the transmitted power to air is

$$U_{AIR,v}(\theta_t)\Big|_{p} = U_v(\theta)\cdot\frac{\cos^2(\theta_t)}{n_{_{SC}}\big(\cos\theta + n_{_{SC}}\cos\theta_t\big)^2} \tag{1.7}$$

- Power radiated into the substrate

The power radiated into the substrate is the superposition of both a directly emitted wave and the reflected one in the interface between semiconductor and air. If $r(\theta)\Big|_{p} = |r(\theta)|e^{i\delta(\theta)}$ is the complex reflection coefficient with modulus $|r(\theta)|$ and argument $\delta(\theta)$, calculated as

$$r(\theta)\Big|_{p} = \frac{\cos(\theta) - n_{_{SC}}\cos(\theta_t)}{\cos(\theta) + n_{_{SC}}\cos(\theta_t)} \tag{1.8}$$

the power radiated per unit solid angle $d\Omega$ in the semiconductor is

$$\begin{aligned} &U_{SC,v}(\theta)\Big|_{p}\cdot d\Omega = \\ &U_v(\theta)\cdot\Big[1 + |r(\theta)|^2 + 2|r(\theta)|\cos\Big(z_0\cos(\theta) + \delta(\theta)\Big)\Big]d\Omega \end{aligned} \tag{1.9}$$

The first and the second term in Eq. (1.9) are the direct and the reflected waves, respectively. The third one is the interference between them. For $\theta < \theta_c = \arcsin(1/\sqrt{\varepsilon_{_{SC}}})$ (blue ray on Fig. 1.5) the radiation pattern is

$$U_{SC,v}(\theta)\Big|_p = U_v(\theta)\cdot\frac{4\,\cos^2(\theta)}{\big(\cos\theta + n_{_{SC}}\cos\theta_t\big)^2} \tag{1.10}$$

For $\theta_c < \theta < 90°$, total internal refection occurs. The radiation pattern is found to be

$$U_{SC,v}(\theta)\Big|_p = U_v(\theta)\cdot\frac{4\,\cos^2(\theta)}{(n_{_{SC}}^2-1)\cdot\big[(1+n_{_{SC}}^2)\sin^2(\theta)-1\big]} \tag{1.11}$$

Fig. 1.6 shows the calculated radiation pattern for the vertical hertzian dipole normalized to the maximum power emitted by the embedded vertical dipole (Eq. (1.3)). A relative permittivity of $\varepsilon_{_{SC}} = 12.96$ is assumed (InGaAs). As expected, most of the power is radiated towards the high-permittivity substrate. The radiation pattern has a maximum at the critical angle $\theta_c = \arcsin(1/\sqrt{\varepsilon_{_{SC}}}) \approx 16°$. At this maximum, the radiation intensity is only a $4/n_{_{SC}}^2 \approx 31\%$ of the maximum value at $\theta = 90°$ for a vertical dipole embedded in a infinite medium.

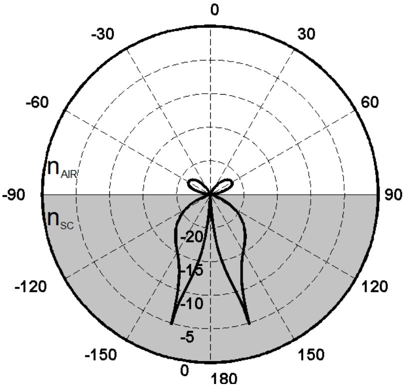

Figure 1.6: Radiation intensities for a vertical hertzian dipole lying on a semi-infinite substrate (shadowed).

1.2.2 Horizontal dipole

The dipole is now parallel to the XY plane. The radiated fields can be expressed as a combination of two p- and s- wave component. The p-wave is defined for each direction as the E-fields component contained in the plane perpendicular to XY plane. The s-wave is the E-field component parallel to the XY plane. Both radiation intensities components of the horizontal dipole embedded in an infinite substrate $U_h(\theta,\phi)$ are calculated from the following equations

$$U_h(\theta,\phi)\Big|_p = U_0\Big(\cos(\theta)\cos(\phi)\Big)^2 \tag{1.12a}$$

$$U_h(\theta,\phi)\Big|_s = U_0\sin^2(\phi) \tag{1.12b}$$

Fig. 1.7 sketches the geometry when considering a semi-infinite substrate. The radiation pattern depends on both θ and the azimuthal angle ϕ, so a 3D consideration is required. Both s- and p- components must be taken into account when considering reflections and transmissions in the semi-infinite substrate. Next, the calculation of the radiation intensity is outlined for $z < 0$ (air) and $z > 0$ (semiconductor). As in the case of vertical hertzian dipole, the detailed development is given in [10–12].

- <u>Power radiated into the air</u>

The procedure is similar that the vertical dipole one. However, both s- and p- polarization components must be considered, as stated above. By doing so, the transmission of power from the substrate to the air is defined as follows

$$U_{AIR,h}(\theta_t)\Big|_p \cdot d\Omega_t = T(\theta)\Big|_p \cdot U_h(\theta)\Big|_p \cdot d\Omega \tag{1.13a}$$

$$U_{AIR,h}(\theta_t)\Big|_s \cdot d\Omega_t = T(\theta)\Big|_s \cdot U_h(\theta)\Big|_s \cdot d\Omega \tag{1.13b}$$

where $T(\theta)\Big|_p$ is the transmittance fo the p- polarized wave, as defined in Eq. (1.5); and $T(\theta)\Big|_s$ is the transmittance for the s- polarized wave

$$T(\theta)\Big|_s = \frac{4\,\cos(\theta)\cos(\theta_t)}{\big(n_{SC}cos(\theta) + \cos(\theta_t)\big)^2} \tag{1.14}$$

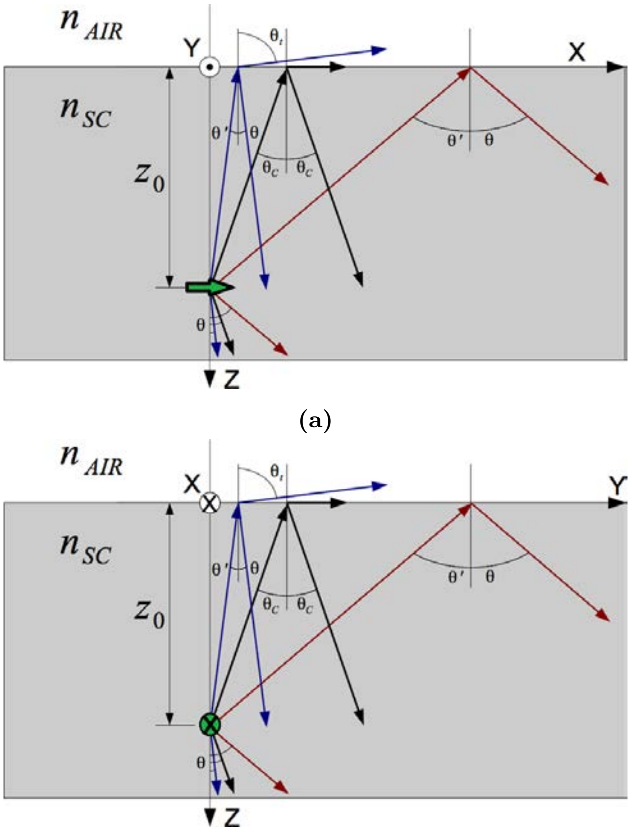

(a)

(b)

Figure 1.7: Direct, reflected and transmitted beams for a horizontal dipole in x direction at a distance z_0 below the interface to air. The radiation pattern depends on the azimuthal angle ϕ. Both XZ-Plane (a) and YZ-Plane (b) are shown. For $0 < \theta' < \theta_C$ a transmitted beam exists (blue), for $\theta_C < \theta' < \pi/2$ total reflection occurs (red). $\theta' = \theta_C$ caso is also shown (black).

The angular distribution of the transmitted power to air for the s- and -p waves is

$$U_{AIR,h}(\theta_t,\phi)\Big|_p = U_h(\theta,\phi)\Big|_p \cdot \frac{\cos^2(\theta_t)}{n_{SC}\big(\cos\theta + n_{SC}\cos\theta_t\big)^2} \tag{1.15a}$$

$$U_{AIR,h}(\theta_t,\phi)\Big|_s = U_h(\theta,\phi)\Big|_s \cdot \frac{\cos^2(\theta_t)}{n_{SC}\big(n_{SC}\cos\theta + \cos\theta_t\big)^2} \tag{1.15b}$$

The total distribution of radiated power to air is calculated by adding both components

$$U_{AIR,h}(\theta_t,\phi) = U_{AIR,h}(\theta_t,\phi)\Big|_p + U_{AIR,h}(\theta_t,\phi)\Big|_s \tag{1.16}$$

- Power radiated into the substrate

As for the vertical dipole, both a direct emitted wave and a reflected one must be taken into account. In this case, the reflection coefficients for both p- (Eq. (1.8)) and s- waves must be calculated

$$r(\theta)\Big|_s = \frac{n_{SC}\cos(\theta) - \cos(\theta_t)}{n_{SC}\cos(\theta) + \cos(\theta_t)} \tag{1.17}$$

Again, it is possible to calculate the power radiated per unit solid angle $d\Omega$ from the substrate to the air.

$$\begin{aligned} U_{SC,v}(\theta)\Big|_{p,s} d\Omega &= \\ = U_h(\theta)\Big|_{p,s} \cdot \Big[1 + |r(\theta)\Big|_{p,s}|^2 + 2|r(\theta)\Big|_{p,s}| \cos\Big(z_0\cos(\theta) + \delta(\theta)\Big|_{p,s}\Big)\Big] d\Omega \end{aligned} \tag{1.18}$$

Same interpretation as is Eq. (1.9) is applicable to Eq. (1.18). For $\theta < \theta_c$ the radiation pattern for both p- and s- waves is

$$U_{SC,h}(\theta,\phi)\Big|_p = U_h(\theta,\phi)\Big|_p \cdot \frac{4\,n_{_{SC}}^2 \cos^2(\theta_t)}{\left(\cos\theta + n_{_{SC}} \cos\theta_t\right)^2} \tag{1.19a}$$

$$U_{SC,h}(\theta,\phi)\Big|_s = U_h(\theta,\phi)\Big|_s \cdot \frac{4\,n_{_{SC}}^2 \cos^2(\theta)}{\left(n_{_{SC}} \cos\theta + \cos\theta_t\right)^2} \tag{1.19b}$$

For $\theta_c < \theta < 90°$ the radiation pattern is found to be

$$U_{SC,h}(\theta,\phi)\Big|_p = U_h(\theta,\phi)\Big|_p \cdot \frac{4\,n_{_{SC}}^2 \left(n_{_{SC}}^2 \sin^2(\theta) - 1\right)}{(n_{_{SC}}^2 - 1) \cdot \left[(1 + n_{_{SC}}^2) \sin^2(\theta) - 1\right]} \tag{1.20a}$$

$$U_{SC,h}(\theta,\phi)\Big|_s = U_h(\theta,\phi)\Big|_s \cdot \frac{4\,n_{_{SC}}^2 \cos^2(\theta)}{(n_{_{SC}}^2 - 1)} \tag{1.20b}$$

Again, the total distribution of radiated power to air is calculated by adding both components

$$U_{SC,h}(\theta,\phi) = U_{SC,h}(\theta,\phi)\Big|_p + U_{SC,h}(\theta,\phi)\Big|_s \tag{1.21}$$

Fig. 1.8 shows the calculated radiation pattern for a horizontal Hertzian dipole lying in a semi-infinite InGaAs substrate. It fits with the electrical dipole results shown in [13]. The maximum is found in the $\phi = 90°$ plane, at $\theta = \theta_c$. It is around 6 dB when normalized with the horizontal dipole embedded in a infinite substrate. In the $\phi = 0°$ plane there is a null at $\theta = \theta_c$.

1.2.3 Abnormalities in the radiation pattern

At this point, it is important to analyze the calculated radiation patterns for horizontal and vertical Hertzian dipoles. Both have a null at

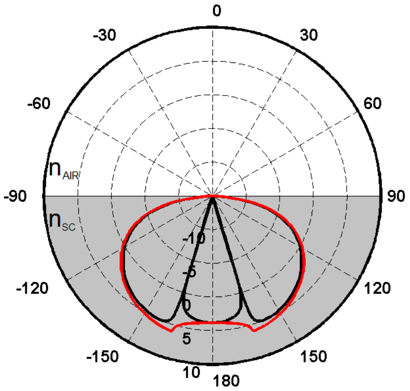

Figure 1.8: Radiation intensities for a horizontal hertzian dipole lying on a semi-infinite substrate (shadowed). Both $\phi = 0°$ (black) plane and $\phi = 90°$ (red) plane are shown. Back radiation is not appreciated, since it is below -20 dB.

the interface (XY plane), which is consistent with the discussion in [14]. The radiation pattern shown in Figs. 1.6 and 1.8 have its maximums at $\theta = \theta_c$, as said before. At these points, the radiation patterns are non-derivable. In this subsection, the meaningless of such peaks is discussed.

According to the Bernstein theorem [15], if we can define an upper limit F_1 of a radiation function $F(\tau)$, being $\tau = \sin(\theta)$, the derivative function of $F(\tau)$, $F(\tau)/d\tau$, must be bounded according to the following expression

$$\frac{1}{F_1}\frac{dF(\tau)}{d\tau} \leq 2\pi\upsilon_0 \tag{1.22}$$

where υ_0 bounds the $F(\tau)$ spectrum in the $[-\upsilon_0, \upsilon_0]$ interval and can be defined from the normalized dimension D of the antenna aperture

$$\upsilon_0 = \frac{D}{2\lambda} \tag{1.23}$$

This limitation must be taken into account when designing antennas with special slope requirements in the radiation pattern (eg. feeders for

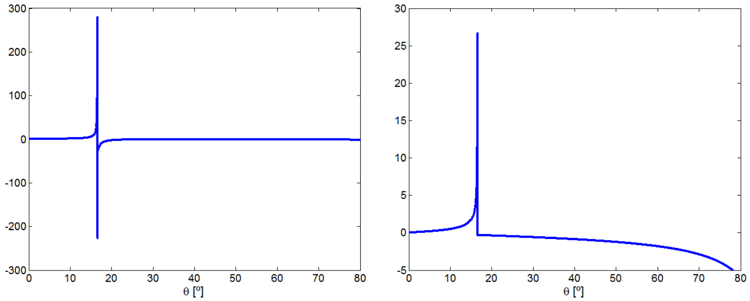

(a) **(b)**

Figure 1.9: First derivative from the $\phi = 90°$ radiation pattern of the vertical (a) and the horizontal (b) hertzian dipole.

reflectors). More generally, Bernstein's theorem limits all derivatives of bounded signals with bounded spectra

$$\frac{1}{F_1} F^{(n)}(\tau) \leq (2\pi\upsilon_0)^n \tag{1.24}$$

Fig. 1.9 shows the calculated derivative of the radiation patterns for both vertical (Fig. 1.9a) and horizontal (Fig. 1.9b) hertzian dipoles. Even when they are bounded and the theorem is satisfied, higher derivatives, such as second one, are not, which violates Bernstein's theorem.

Of course such radiation patterns cannot be correct, since the far field cannot have a slope discontinuity. If so, Maxwell's equations would not be satisfied, since and E-field with a slope discontinuity would produce a step function in H and, doing a curl on H to find E would lead to a delta function, which is clearly incorrect.

This anomaly happens because of the approximation used to derive the far-field expressions. The stationary phase (SP) approximation breaks down at the critical angle. The SP method has an integrand of the form $F(x)e^{-jkf(x)}$, where $F(x)$ is assumed to have a well-behaved phase near the stationary point. When considering two semi-infinite media, $F(x)$ goes from real to complex at the critical angle. This violates the phase assumption, which leads to the abrupt change in the radiation pattern slope.

This is also noticed in other antennas studies [16]. A careful application of the SP method should be taken into account.

1.3 Dipole lying on dielectric slabs

In [17], authors perform a theoretical study of a electrically small dipole embedded in a semi-infinite dielectric slab of finite thickness and refractive index $n_{SC} < n_{AIR} \approx 1$. A dipole lying in the ZX plane is assumed. Its moment $\hat{n}$ defines an arbitrary and fixed angle α with the Z-axis. The geometry of the problem is sketched in Fig. 1.10. For simplicity, only three parallel rays, a reflected in the upper interfase one I_r, a direct one II and its successive inner refection II_r, and the corresponding radiation towards $z > 0$ has been plotted. Since all are coherent between them, an interference pattern occurs. The total power resulting from the interference propagates towards the $z > 0$ interface under the solid angle $d\Omega = \sin\theta d\theta d\phi$. Part of this power is radiated towards the air under the solid angle $d\Omega_t = \sin\theta d\theta_t d\phi$.

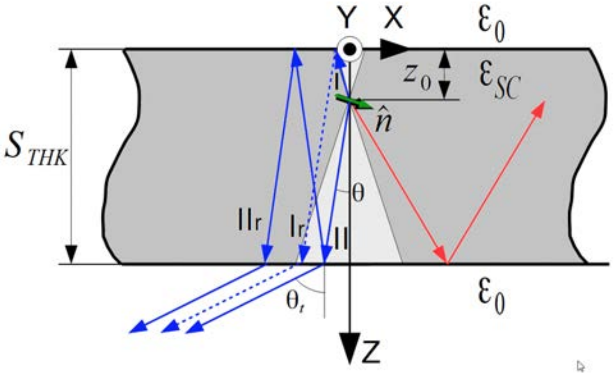

Figure 1.10: Antenna emitter lying on a infinite dielectric slab of thickness S_{THK}. All the rays radiated in the shadowed region (red) are totally internal reflected in both interfaces. Coherent interference between many different rays is produced for each radiation direction (θ_t, ϕ). Rays II and II_r (solid blue) are due to the dipole radiation in the (θ, ϕ) direction. The ray I_r is due to the radiation along $(180° - \theta, \phi)$ (dashed blue).

According to [17], for the dipole D, which has a radiation pattern described by

$$U(\theta,\phi)\Big|_{p} = U_0 \cdot \Big(\cos(\alpha)\sin(\theta) + \sin(\alpha)\cos(\theta)\cos(\phi)\Big)^2 \tag{1.25a}$$

$$U(\theta,\phi)\Big|_{s} = U_0 \cdot \sin^2(\alpha)\sin^2(\phi) \tag{1.25b}$$

when is inside an infinite medium, the radiation pattern when embedded in a dielectric slab can be calculated as follows

$$U_{z>0}(\theta_t,\phi)\Big|_{p} = Q(\theta,\phi)\Big|_{p} M(\theta)\Big|_{p} \hat{T}(\theta_t)\Big|_{p} \tag{1.26a}$$

$$U_{z>0}(\theta_t,\phi)\Big|_{s} = Q(\theta,\phi)\Big|_{s} M(\theta)\Big|_{s} \hat{T}(\theta_t)\Big|_{s} \tag{1.26b}$$

where $\theta_t = \arcsin(n_{_{SC}}\sin(\theta))$ and

$$\begin{aligned} Q(\theta,\phi)\Big|_{p} = U_0 \cdot \Big[&\cos^2(\alpha)\sin^2(\theta)\,W_+(\theta)\Big|_{p} \\ &+ \sin^2(\alpha)\cos^2(\theta)\cos^2(\phi)\,W_-(\theta)\Big|_{p} \\ &- \frac{1}{2}\sin(2\alpha)\cos(2\theta)\cos(\phi)T(\theta)\Big|_{p}\Big] \end{aligned} \tag{1.27a}$$

$$Q(\theta,\phi)\Big|_{s} = U_0 \cdot \sin^2(\alpha)\sin^2(\phi)\,W_+(\theta)\Big|_{s} \tag{1.27b}$$

which are the radiation pattern for the p- and s- polarizations of a dipole embedded in a semi-infinite substrate. $U_0 = 1$ is chosen for normalizing to the maximum power emitted by the same dipole in a infinite medium. If $z_0 = 0$ they become equivalent to the radiation pattern obtained in Section 1.2. The influence of the interference between II and I_r (solid and dashed blue rays in Fig. 1.10, respectively) is taken into account with the factors $W_\pm(\theta)\Big|_{p}$ and $W_\pm(\theta)\Big|_{s}$

$$\begin{aligned} &W_\pm(\theta)\Big|_{p,s} = \\ &= 1 + |r(\theta)\Big|_{p,s}|^2 \pm 2|r(\theta)\Big|_{p,s}| \cdot \cos\left[4\pi\frac{n_{_{SC}}z_0}{\lambda_0}\cos\theta + \delta(\theta)\Big|_{p,s}\right] \end{aligned} \tag{1.28}$$

where $r(\theta)\Big|_{p,s} = |r(\theta)\Big|_{p,s}| \cdot e^{i\delta(\theta)\Big|_{p,s}}$ are the reflection coefficient in the interface obtained with Eqs. (1.8) and (1.17). The factors $\hat{T}(\theta_t)\Big|_{p,s}$ are related with the transmittances $T(\theta_t)\Big|_{p,s}$, which calculated with Eqs. (1.5) and (1.14)

$$\hat{T}(\theta_t)\Big|_{p,s} = T(\theta_t)\Big|_{p,s} \cdot \frac{d\Omega}{d\Omega_t} \tag{1.29}$$

with

$$\frac{d\Omega}{d\Omega_t} = \frac{\cos\theta_t}{n_{SC}\cos\theta} \tag{1.30}$$

The factors $M(\theta)\Big|_{p}$ and $M(\theta)\Big|_{s}$ describe the influence of successive reflections between the slab interfaces (solid blue ray IIr in Fig. 1.10).

$$M(\theta)\Big|_{p,s} = |1 - r^2(\theta)\Big|_{p,s} \cdot e^{2\pi i \frac{n_{SC}}{\lambda_0} S_{THK}\cos(\theta)}|^{-2} \tag{1.31}$$

The radiation pattern for $z < 0$ is calculated by only changing the distance of the dipole from the two interfaces, θ and α definition as follows

$$z_0 \to S_{THK} - z_0 \tag{1.32a}$$

$$\theta \to 180 - \theta \tag{1.32b}$$

$$\alpha \to 180 - \alpha \tag{1.32c}$$

It is possible to estimate the amount of power radiate into the air P by integrating the radiation patterns for both $z < 0$ and $z > 0$.

$$\begin{aligned} P = & \int_{\phi=0}^{2\pi} \int_{\theta_t=0}^{\frac{\pi}{2}} \left[U_{z>0}(\theta_t,\phi)\Big|_p + U_{z>0}(\theta_t,\phi)\Big|_s \right] \cdot \sin(\theta_t)\, d\theta_t d\phi \\ & + \int_{\phi=0}^{2\pi} \int_{\theta_t=\frac{\pi}{2}}^{\pi} \left[U_{z<0}(\theta_t,\phi)\Big|_p + U_{z<0}(\theta_t,\phi)\Big|_s \right] \cdot \sin(\theta_t)\, d\theta_t d\phi \end{aligned} \tag{1.33}$$

In [18], the author obtains a closed-from analytic expressions for vertical and horizontal dipoles, P_v and P_h respectively. He studies different values of permittivities ε_{SC} and substrate thicknesses S_{THK}. Both dipoles are compared in terms of power radiated from the dielectric slab. Fig. 1.11 summarizes the results for SiO_2 (Fig. 1.11a), for silicon of permittivity $\varepsilon_{SC} = 18.25$ (Fig. 1.11b) and for a fictitious material of permittivity $\varepsilon_{SC} = 50$ (Fig. 1.11c). The slab thickness is normalized to the wavelength on the substrate material ($\frac{S_{THK}}{\lambda_0} n_{SC}$).

When comparing both Figs. 1.6 and 1.8 a lower efficiency of vertical dipoles is expected, as it is confirmed in Fig. 1.11 for all materials and all thickness. For clarification purposes, the radiated power of the vertical dipole is magnified in Figs 1.11b and 1.11c. For high permittivity material, the resonances become pronounces, so it is clear that the slab acts as a Fabry-Perot resonator. Even if the manufacturing capabilities allows us to tune the substrate thickness for a specific wavelength, low efficiencies must be expected, since most of the generated THz power remains in the substrate for high-permittivity infinite slabs.

1.4 Dielectric lenses

Dielectric lenses are one of the most used elements as a substrate for planar antenna for the terahertz frequencies. This allows improving both the radiation characteristics [14, 19], (directivity, main beam gaussicity, less back radiation) and the overall efficiency, since it drastically increases the amount of THz power radiated into the air. Fig. 1.12 shows same AE with (Fig. 1.12b) and without (Fig. 1.12a) dielectric lenses. A mayor advantage of the lens is the possibility of extracting radiation emitted under an angle exceeding the critical angle for total reflection $\theta_c = \arcsin\sqrt{\frac{1}{\varepsilon_{SC}}}$.

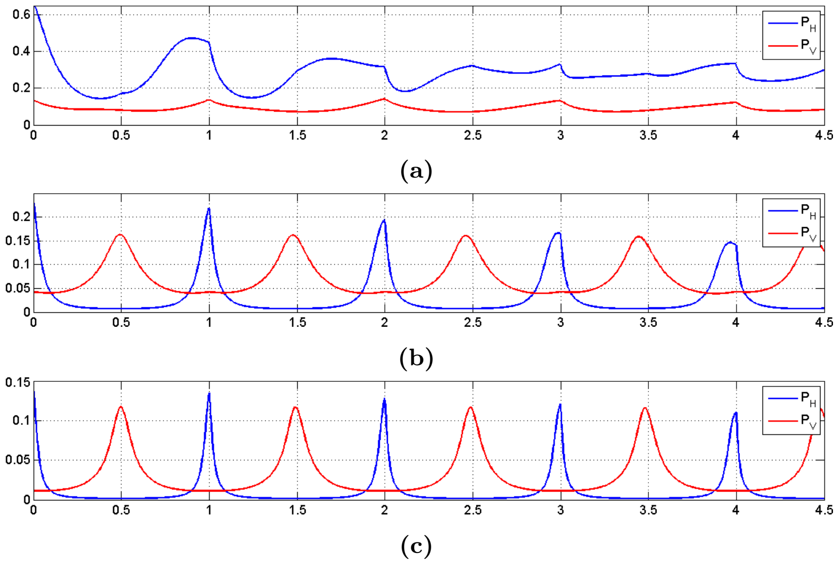

Figure 1.11: Power radiated to the air for the horizontal (P_H, blue) and vertical (P_V, red) dipole. It is normalized to the same antenna in a unbounded medium ($U_0 = 1$). Three different relative permittivities are used: 2.21 (a), 18.25 (b) and 50. Radiated power is strongly reduced for the vertical dipole in comparison with the horizontal one. For clarification purposes, P_V is magnified 60 times in (b) and 200 times in (c).

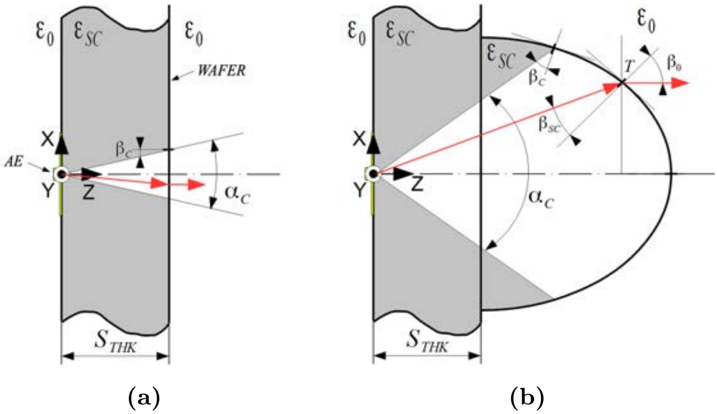

(a) (b)

Figure 1.12: Comparison between an AE lying on a dielectric slab (a) and on a dielectric lens (b). Region where total reflection occurs is shown shadowed. Wafer is assumed to be infinite in the XY plane. All the power lying out of the cone defined by α_c (shadowed) will be totally reflected in the interface between semiconductor and air.

The ideal shape of dielectric lens is the ellipsoidal one [20]. However, it is very difficult to manufacture, which makes it not practical. It can be approximated by an extended hemispherical one [19] or a hyper-hemispherical one, which are much easier to manufacture. In order to design this kind of lenses, full-wave simulations are combined with ray tracing techniques and conventional physical optics, since lens are electrically large ($> 5\lambda$) and they can easily exceed the computational resources, both memory and CPU time. For avoiding such limitations, the design procedure is divided in two main steps:

- Planar antenna design: The AE is simulated with a commercial full-wave electromagnetic simulator. A semi-infinite substrate of permittivity ε_{SC} is assumed. This allows obtaining the radiated field in spherical coordinates.

- Lens simulation: a ray-tracing technique is carried out to extend the fields to the lens surface. Physical optics is then used for obtaining the surface currents; then, the radiated fields; and finally the radiation pattern.

The AE is assumed to be punctual (Fig. 1.13). The dielectric substrate can be divided into four regions [21] (from a to d in Fig. 1.13) depending if there exists both transmitted and reflected rays in the external surface (a and d) or if there is total internal reflection (b and c). Obviously, only a and d regions contributes to the radiation pattern, since b and c only produce evanescent waves outside the dielectric. d region can be safely neglected for calculating fields far from XY plane [22]. Refected rays among the different regions can be reflected again and eventually escaping from the substrate, but its contribution is negligible [22].

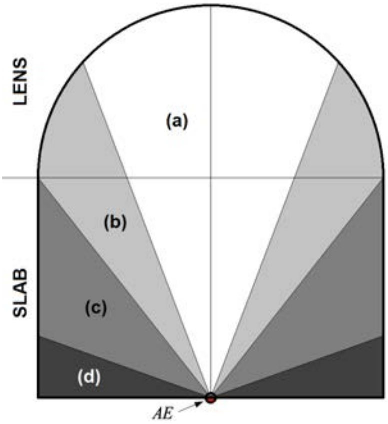

Figure 1.13: Regions into which a lens attached to a dielectric slab can be divided. The antenna emitter (red) is considered as a punctual source. lens (a and b) and slab (c and d) regions where both transmitted and reflected rays appear (a and d) and where total internal reflection occurs (b and c).

Physic optics is used for calculating the surface currents in the region a of the lens. Both electric and magnetic transverse electric (TE) and transverse magnetic (TM) components are obtained in the dielectric-air interface for TE and TM components. The reflectance Γ and the transmittance τ is calculated with the following expressions [23]:

$$\Gamma_{TE} = \frac{\sqrt{\varepsilon_{SC}}\cos\beta_{SC} - \sqrt{1-\varepsilon_{SC}\sin^2\beta_{SC}}}{\sqrt{\varepsilon_{SC}}\cos\beta_{SC} + \sqrt{1-\varepsilon_{SC}\sin^2\beta_{SC}}} \tag{1.34a}$$

$$\tau_{TE} = 1 + \Gamma_{TE} \tag{1.34b}$$

$$\Gamma_{TM} = \frac{\sqrt{\varepsilon_{SC}}\sqrt{1-\varepsilon_{SC}\sin^2\beta_{SC}} - \cos\beta_{SC}}{\sqrt{\varepsilon_{SC}}\sqrt{1-\varepsilon_{SC}\sin^2\beta_{SC}} + \cos\beta_{SC}} \tag{1.34c}$$

$$\tau_{TM} = \Big(1 + \Gamma_{TM}\Big)\frac{\cos\beta_{SC}}{\sqrt{1-\varepsilon_{SC}\sin^2\beta_{SC}}} \tag{1.34d}$$

where β_{SC} is the incidence angle with respect to the normal lens surface (Fig. 1.12). Then, both electric $\vec{J_s}$ and magnetic $\vec{M_s}$ current densities are obtained outside the lens surface [23]:

$$\vec{J_s} = \hat{n} \times \vec{H} \tag{1.35a}$$

$$\vec{M_s} = \hat{n} \times \vec{E} \tag{1.35b}$$

where $\hat{n}$ is the vector normal to the interface. Finally θ and ϕ components of the electric far field are obtained [23]:

$$E_\theta \approx -\frac{jke^{-jkr}}{4\pi r}\Big(L_\phi + \eta N_\theta\Big) \tag{1.36a}$$

$$E_\phi \approx \frac{jke^{-jkr}}{4\pi r}\Big(L_\theta + \eta N_\phi\Big) \tag{1.36b}$$

where η is the intrinsic impedance, $k = 2\pi/\lambda$ is the wavenumber, and $\vec{N}$ and $\vec{L}$ are the radiation vectors defined by [23]

$$\vec{N} = \iint_{S'} \vec{J_s} e^{jkr'\cos\psi}\, ds' \tag{1.37a}$$

$$\vec{L} = \iint_{S'} \vec{M_s} e^{jkr'\cos\psi}\, ds' \tag{1.37b}$$

where S' is the external surface of the lens region a, r' is the distance from origin to where the equivalent magnetic and electric density current are calculated, r is the distance from origin to the observation point and ψ is the angle between r' and r.

1.4.1 Performance estimation

On most applications, it is desired to have all the power radiated at only one direction. Because of the substrate effect, most of the generated power will be either confined in the dielectric or radiated along Z>0 (Fig. 1.12) if a lens is place below the AE, as discussed above. For quantifying how much of the generated power is radiated along Z>0, let us define the emission efficiency η as follows

$$\eta \triangleq \frac{P_{THz}^{rad}\Big|_{Z>0}}{P_{THz}^{gen}} = \frac{P_{THz}^{rad}\Big|_{Z>0}}{P_{THz}^{rad}\Big|_{Z>0} + P_{THz}^{rad}\Big|_{Z<0} + P_{THz}^{tir}} \tag{1.38}$$

where P_{THz}^{gen} is the total amount of generated THz power; $P_{THz}^{rad}\Big|_{Z>0}$ and $P_{THz}^{rad}\Big|_{Z<0}$ are the amount of power radiated in half-semispace towards $Z > 0$ and $Z < 0$, respectively; and P_{THz}^{tir} is the power that does not leave the substrate due to total internal reflection at eh substrate-air interface.

A simulation model of a log-periodic antenna of radius $R = 710\,\mu$m lying on a 300 μm thick infinite high-permittivity ($\varepsilon_r = 12$) slab has been done. No losses are taken into account. Using HFSS [24], it is possible to obtain $P_{THz}^{rad}\Big|_{Z>0}$, $P_{THz}^{rad}\Big|_{Z<0}$ and P_{THz}^{tir} by integrating the fields in the model boundaries. A frequency of 150 GHz is assumed for all the simulations. Table 1.1 shows emission efficiencies for hyper-hemispherical lenses of different radius. Efficiencies above 85% are feasible for electrically large antennas. On the other hand, using no lenses would lead to an emission efficiency of less than 30%.

R	Substrate $\left(P^{tir}_{THz}\right)$	Back radiaton $\left(P^{rad}_{THz}\big\vert_{Z<0}\right)$	η $\left(P^{rad}_{THz}\big\vert_{Z<0}\right)$
Plain AE	50%	20.4%	29.6%
$R = 0.50$ mm	14.7%	9.3%	76.0%
$R = 0.75$ mm	17.1%	9.8%	73.1%
$R = 1$ mm	20.0%	5.0%	75.0%
$R = 2$ mm	12.4%	4.0%	83.6%
$R = 3$ mm	5.0%	8.3%	86.7%
$R = 5$ mm	3.4%	9.5%	87.1%

Table 1.1: Comparative between efficiencies when using lenses of different radius R.

1.5 Conclusions

The families of planar antennas used for photomixing THz sources considered in this thesis were introduced. The effect of high-permittivity substrates in THz dipole antennas properties has been in-deep analyzed. Since both horizontal and vertical infinitesimal dipoles are the canonical cases analytical expressions for both have been obtained. Both semi-infinite substrate and infinite dielectric slabs have been considered. For semi-infinite substrates, the radiation intensities have been expressed as the product of two factors: the radiation pattern when embedded in a infinite medium and the effect of the interface. This allow us to model a new antenna-less photomixing source: the large area emitter (LAE).

The use of electrically large silicon lenses as substrate for photomixing sources is described. The physical optics (PO) calculation method is described. It allow us to obtain the radiation intensities of an AE lying on a dielectric lens from either the analytical or simulated radiation pattern when lying on a semi-infinite substrate. An alternative to dielectric lenses is introduced in Chapter 4.

1.6 References

[1] G. M. Rebeiz, “Millimeter-wave and terahertz integrated circuit antennas,” *Proceedings of the IEEE*, vol. 80, no. 11, pp. 1748–1770, 1992.

[2] Y. Mushiake, “Self-complementary antennas,” *IEEE Antennas and Propagation Magazine*, vol. 34, no. 6, pp. 23–29, 1992.

[3] D. S. Filipović and J. L. Volakis, “Novel slot spiral antenna designs for dual-band/multiband operation,” *IEEE Transactions on Antennas and Propagation*, vol. 51, no. 3, pp. 430–440, 2003.

[4] R. DuHamel and F. Ore, “Logarithmically periodic antenna designs,” *IRE International Convention Record*, vol. 1, p. 7, 1958.

[5] S. M. Duffy, S. Verghese, K. McIntosh, A. Jackson, A. Gossard, and S. Matsuura, “Accurate modeling of dual dipole and slot elements used with photomixers for coherent terahertz output power,” *IEEE Transactions on Microwave Theory and Techniques*, vol. 49, no. 6, pp. 1032–1038, 2001.

[6] D. F. Filipovic, W. Y. Ali-Ahmad, and G. M. Rebeiz, “Millimeter-wave double-dipole antennas for high-gain integrated reflector illumination,” *IEEE Transactions on Microwave Theory and Techniques*, vol. 40, no. 5, pp. 962–967, 1992.

[7] T. Endo, Y. Sunahara, S. Satoh, and T. Katagi, “Resonant frequency and radiation efficiency of meander line antennas,” *Electronics and Communications in Japan (Part II: Electronics)*, vol. 83, no. 1, pp. 52–58, 2000.

[8] I. Woo, T. K. Nguyen, H. Han, H. Lim, and I. Park, “Four-leaf-clover-shaped antenna for a THz photomixer,” *Optics Express*, vol. 18, no. 18, pp. 18 532–18 542, 2010.

[9] C. A. Balanis, *Antenna Theory: Analysis and Design.* John Wiley & Sons, 2005.

[10] W. Lukosz, “Light emission by magnetic and electric dipoles close to a plane dielectric interface. III. radiation patterns of dipoles with arbitrary orientation,” *JOSA*, vol. 69, no. 11, pp. 1495–1503, 1979.

[11] W. Lukosz and R. Kunz, “Light emission by magnetic and electric dipoles close to a plane interface. I. total radiated power,” *JOSA*, vol. 67, no. 12, pp. 1607–1615, 1977.

[12] W. Lukosz and R. Kunz, “Light emission by magnetic and electric dipoles close to a plane dielectric interface. II. radiation patterns of perpendicular oriented dipoles,” *JOSA*, vol. 67, no. 12, pp. 1615–1619, 1977.

[13] M. Kominami, D. Pozar, and D. Schaubert, “Dipole and slot elements and arrays on semi-infinite substrates,” *IEEE transactions on Antennas and Propagation*, vol. 33, no. 6, pp. 600–607, 1985.

[14] D. B. Rutledge, D. P. Neikirk, and D. P. Kasilingam, “Integrated circuit antennas,” *Infrared and Millimeter Waves*, vol. 10, no. part 2, pp. 1–90, 1983.

[15] S. Drabowitch, A. Papiernik, H. Griffiths, J. Encinas, and B. L. Smith, *Modern antennas.* Springer Science & Business Media, 2010.

[16] D. R. Jackson, P. Burghignoli, G. Lovat, F. Capolino, J. Chen, D. R. Wilton, and A. A. Oliner, “The fundamental physics of directive beaming at microwave and optical frequencies and the role of leaky waves,” *Proceedings of the IEEE*, vol. 99, no. 10, pp. 1780–1805, 2011.

[17] W. Lukosz, “Light emission by multipole sources in thin layers. I. radiation patterns of electric and magnetic dipoles,” *JOSA*, vol. 71, no. 6, pp. 744–754, 1981.

[18] S. Brueck, “Radiation from a dipole embedded in a dielectric slab,” *IEEE Journal of Selected Topics in Quantum Electronics*, vol. 6, no. 6, pp. 899–910, 2000.

[19] D. F. Filipovic, S. S. Gearhart, and G. M. Rebeiz, “Double-slot antennas on extended hemispherical and elliptical silicon dielectric lenses,” *IEEE Transactions on Microwave Theory and Techniques*, vol. 41, no. 10, pp. 1738–1749, 1993.

[20] T. A. Milligan, *Modern Antenna Design.* John Wiley & Sons, 2005.

[21] S.-Y. Chen and P. Hsu, "A simplified method to calculate far-field patterns of extended hemispherical dielectric lens," in *2007 Asia-Pacific Microwave Conference.* IEEE, 2007, pp. 1–4.

[22] A. Neto, S. Maci, and P. De Maagt, "Reflections inside an elliptical dielectric lens antenna," *IEE Proceedings-Microwaves, Antennas and Propagation*, vol. 145, no. 3, pp. 243–247, 1998.

[23] C. A. Balanis, *Advanced engineering electromagnetics.* John Wiley & Sons, 2012.

[24] Website of ANSYS HFSS,
http://www.ansys.com/Products/Electronics/ANSYS-HFSS.

CHAPTER 2

OPTOELECTRONIC TERAHERTZ SOURCES

In the Preface of this thesis, an expression of the radiated THz power $P_{THz}^{id}$by an ideal AE is deducted (Eq. (9)). This amount of power is an upper bound. There are several issues that limit the efficiency of an optoelectronic terahertz source:

- Laser reflection in the device surface. It is defined by a reflection coefficient R in the photomixer surface. It is possible to minimize R by an anti-reflection coating. This extra layer also passivate the device, which increase its operational life by protecting it against corrosion.
- Inefficient absorption of light: not all the optical power is absorbed in the active volume of the device. Photocarriers must be generated inside a DC electric field in order to have them accelerated towards the device contacts. This is typically achieved in a small volume. All optical power absorbed outside this region does not contribute to the photocurrent. As an example, a typical 1550 nm device has an absorption length d_i of 1 μm. Since $\mathrm{In}_{0.53}\mathrm{Ga}_{0.47}\mathrm{As}$ has an absorption coefficient $\alpha = 0.8 \cdot 10^{-4}$ cm^{-1}, the photomixer has an absorbance $A = 1 - e^{-\alpha d_i} = 55\%$.

- Impedance mismatch between the device and the antenna, which impedes the radiation of part of the generated photocurrent.The mismatch factor M is defined as follows

$$M = \frac{4R_aR_p}{(R_a + R_p)^2 + (X_a + X_p)^2} \tag{2.1}$$

where $Z_a = R_a + jX_a$ is the input impedance of the antenna and $Z_p = R_p + jX_p$ is the input impedance of the photomixer.

The reduction of both DC current I^{id}_{DC} and AC current I^{id}_{THz} regarding the ideal values calculated with Eqs. (8a) and (8b) is summarized in a external quantum efficiency η_{ext}

$$\eta_{ext} = (1 - R)^2 \cdot \left[1 - e^{-\alpha d_i}\right] \cdot M \tag{2.2}$$

At higher frequencies, there are two main factors that limit the performance:

- The RC roll-off. When connecting an antenna to the photomixer, the radiation resistance R_A is connected in parallel with the device capacitance. This conforms a low-pass filter that atenuates higher frequencies, according to its cut-off frequency. This attenuation can be calculated for every frequency ν_{THz} as follows:

$$\eta_{RC} = \frac{1}{1 + (2\pi R_A C \cdot \nu_{THz})^2} \tag{2.3}$$

- The life-time or transit-time of the photocarriers. If there is an accumulation of generated carriers in the deviceś active area, a screening of the THz signal will be produced, which reduces its amplitude. Losses due to this roll-off can be expresed as follows:

$$\eta_{tr} = \frac{1}{1 + (2\pi\tau \cdot \nu_{THz})^2} \tag{2.4}$$

where τ depends on the speed of the device an can be related to either the carrier lifetime τ_{rec} or transit time τ_{tr} depending on the specific device.

Therefore, the total radiated power is

$$P_{THz}^{id} = P_{THz}^{id} \cdot \eta_{ext} \cdot \eta_{RC} \cdot \eta_{tr} \tag{2.5}$$

This chapter introduces the photomixer-based terahertz sources related to this thesis. Photoconductives and *n-i-pn-i-p* photomixers for CW THz generation are described. For increasing the achieved power level, the combination of many coherently illuminated AE sources is evaluated.

Finally, a new device, the LAE is described and analyzed. Using the theoretical results that model dipoles embedded in semi-infinite substrates (see Chapter 1), an analytical model for this novel terahertz source is proposed.

2.1 Photoconductive photomixers

A photoconductive photomixer is made by simply adding two metal contact electrodes to a highly resistive semiconductor medium. This structure switches from high to low resistivity when the gap between contacts W_g is illuminated with a laser source of proper wavelength. An external DC field is required in order to separate the carriers and generate a photocurrent. Typical bias levels are from few volts to around 100 V, depending on the distance between electrodes and the device breakdown voltage.

In order to achieve an efficient CW power generation at high THz frequencies, the carrier recombination time τ_{rec} should be as short as possible [1]. A proper substrate with recombination mechanisms, such as LT-GaAs [2], can be chosen. A $\tau_{rec} = 100$ ps has been achieved for LT-GaAs [3], which leads to a 3 dB cut-off frequency of 1.6 THz [4].

In a realistic device, the photocurrent amplitude is reduced by a photoconductive gain $g = \tau_{rec}/\tau_{tr}$, where τ_{tr} is the transit time, defined as $\tau_{tr} = W_g/v_{drift}$ if we assume that electrons are instantaneously accelerated and they follow the shortest path (a straight line) between electrodes [5]. v_{drift} is the saturated drift velocity. Considering a gap of 1 μm and a drift velocity of 10^7 cm/s, the transit time is $\tau_{tr} \approx 10$ ps. There would be a reduction of power by a factor of 10^{-4}. Taking into account the photoconductive gain, Eq. (2.5) becomes

$$P^{id}_{THz} = P^{id}_{THz} \cdot g^2 \cdot \eta_{ext} \cdot \eta_{RC} \cdot \eta_{tr} \tag{2.6}$$

For increasing the radiated THz power, the E-field amplitude in the gap must be maximized [6]. Furthermore, it is desirable to get an uniform E-field distribution across the gap. Aditionally, the device capacitance should be minimize as much as possible for reducing the RC roll-off. Electrodes should be designed to accomplish these objectives without compromising τ_{tr}. Figure 2.1 shows four examples of electrodes configurations for a photoconductive area of AxB.

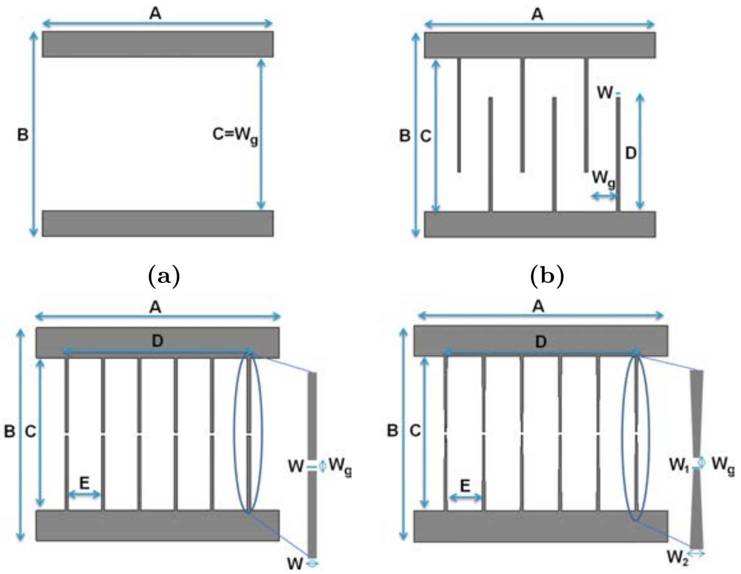

(a) **(b)**

(c) **(d)**

Figure 2.1: Top view of a bare electrode photoconductive photomixer (a). Interdigitated electrodes (b). Six fingers rectangular tip-to-tip electrodes (c). Nano-trapezoidal electrodes (d).

Two bare electrodes conform the simplest device design (Fig. 2.1a).

The inter-digitated electrodes topology (Fig. 2.1b) is the most common for photoconductors. It achieves an evenly distributed E-field in a wide active area [7]. However, it has a large capacitance, which drastically reduces the cut-off frequency of the device. In order to reduce it, the use of rectangular tip-to-tip electrode fingers (Fig. 2.1c) is proposed in [8].

In [6], the use of nano-trapezoid fingers (Fig. 2.1d) is proposed for increasing the generated THz power. This is achieved by both reducing the finger width W_1 in the gap. The device capacitance is reduced and the intensity of the E-field in the gap is increased when comparing with same distribution of fingers with $W_1 = W_2 = W$.

For evaluating the performance of each design, several devices with bare electrodes and rectangular and nano-trapezoid fingers are measured and fabricated in the gap of same bow-tie antenna design (Fig. 2.2). The interdigitated electrodes design is not evaluated due to its expected large capacitance and poor performance at higher frequencies. Table 2.1 shows device dimensions. Measured power levels for all three designs are plot in Fig. 2.3.

Parameter	Value [μm]
A	16
B	14
C	10
D	12.2
E	2.2
W	0.2
W_1	0.1
W_2	0.2
W_g	0.2

Table 2.1: Dimensions of photoconductive photomixer electrodes designs.

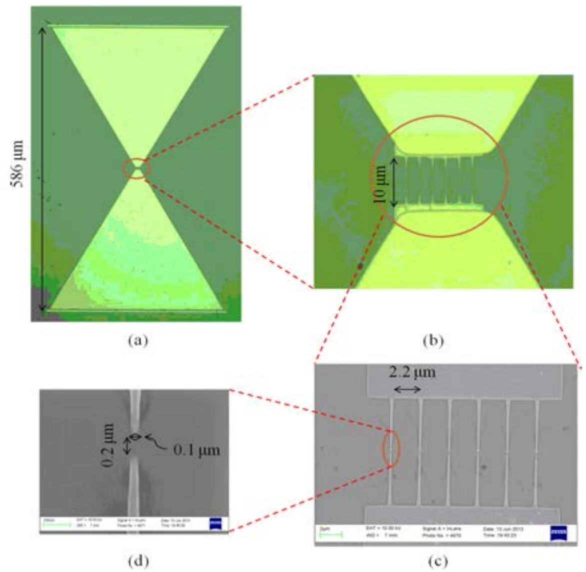

Figure 2.2: SEM photograpy of the THz bowtie antenna with nano-trapezoidal tip-to-tip fingers (a) overall antenna view (b) zoom-in of the photomixer section (c) zoom-in of the nano-trapezoidal tip-to-tip finger (d) zoom-in of a nanogap trapezoidal finger.

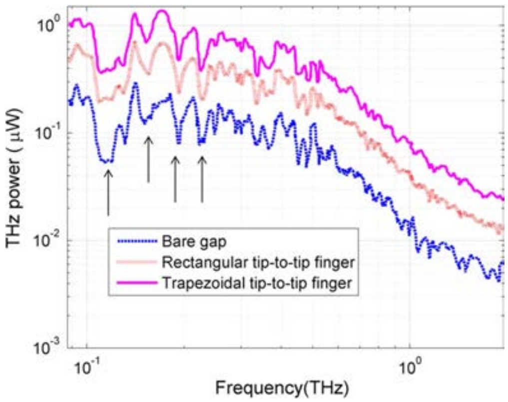

Figure 2.3: Measured THz power for the three photoconductive electrodes design: bare gap (blue, dashed), rectangular (red, dotted) and trapezoidal fingers (pink, solid).

2.2 N-i-pn-i-p photomixers

A *p-i-n* diode [9] consist of a p-doped semiconductor followed by an undoped (intrinsic) one and by a n-doped one (Fig. 2.4). This structure is typically implemented by adding successive layers of doped/undoped semiconductor, which is a more complex manufacturing process than the one required for photoconductive photomixers. An electric field of strength $E_i = E_G/(eW_g)$ is generated in the intrinsic region, where E_G is the band gap energy of the semiconductor, $e = 1.6602 \cdot 10^{-19}$ A·s is the electron charge and W_g is the intrinsic region length. No external bias (or less than the needed for photoconductive devices) is required, which increases the life span of the photomixer. The photocarriers generated in the intrinsic region are efficiently separated because of the buith-in electric field. This is not the case on p an n regions, where generated photocarriers are a slow contibution to the photocurrent. For preventing an increment on $\tau_{tr} = W_g/v_{drift}$, the generation in n and p regions is avoided by increasing the band gap to energies exceeding the photon energy $h\nu$. This can be achieved by adding aluminum to GaAs (for 800 nm devices) or to $\mathrm{In}_{0.53}\mathrm{Ga}_{0.47}\mathrm{As}$ (for 1550 nm devices) in the doped regions.

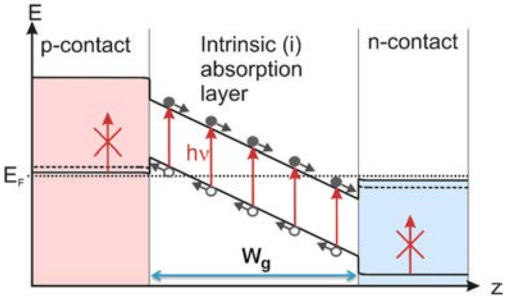

Figure 2.4: Band structure of a *p-i-n* diode. The vertical arrows indicate the photon energy $h\nu$.

The capacitance C_{PIN} of a *p-i-n* is easily estimated by considering it as a plate capacitor

$$C_{PIN} = \varepsilon_0 \varepsilon_{SC} \frac{A}{W_g} \tag{2.7}$$

where A is the device area and W_g is the intrinsic region length. It is not possible to improve the transit-time roll-off without increasing the capacitance, and therefore limiting the working band in the upper frequency range.

Other techniques can be used for reducing the transit time without increasing the capacitance. In [10] the *p-i-n* structure is modified for generating the photocarriers only in a region close to the p-doped contact. Since holes have a much larger effective mass than electrons (by a factor of 11 in InGaAs) they reach lower velocities ($v_h < v_e$). Fig. 2.5 shows the band structure of such diode. Only electrons travel along the full intrinsic region length W_g. Holes only travel along a much smaller distance W_A, which reduces the transit time τ_{tr}. Such kind of *p-i-n* diodes is known as UTC photomixer [9, 11]. An exhaustive analysis of this devices limitations is done in [12].

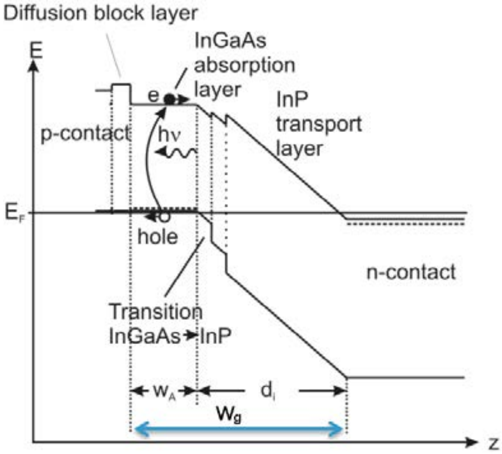

Figure 2.5: Band structure of a UTC *p-i-n* diode.

For reducing the RC roll-off, it is possible to reduce the photodiode area A, which will reduce the capacitance. However, this would reduce the maximum current and the maximum optical incident power. Typically, devices in the range of 3-15 μm^2 are usually considered for the THz range.

A further improvement of τ_{tr} is possible by increasing the velocity of electrons v_e in UTC diodes. Balistic speeds v_{bal} are only possible in vacuum. Inside a medium, electrons collide with atoms, which reduces the maximum velocity (saturation velocity $v_{sat} < v_{bal}$). For avoiding collisions, it is possible to reduce W_G but that would increase again the capacitance of the device. The *n-i-pn-i-p* supperlattice photomixer avoids this by stacking N *p-i-n* diodes with a W_g dimension optimized for achieving quasi-ballistic speeds [13, 14]. Fig. 2.6 sketches the band structure of a two-period *n-i-pn-i-p* photomixer. In order to avould a flat band situation in the pn junction between periods by charge accumulation, the junction is designed as a highly efficient recombination diode that recombines electrons and holes [5]. In order to provide the same optical power for each *p-i-n* diode, N times higher optical power power is required. There is a limit in the maximum number of stacked photomixer due to the non-uniform distribution of the optical power in the devices. A good compromise between power radiated and manufacturing complexity is achieved for $N = 3$, which corresponds with the value for the *n-i-pn-i-p* photomixer samples used in this thesis (see manufacturing details in Subsections A.1, and A.2).

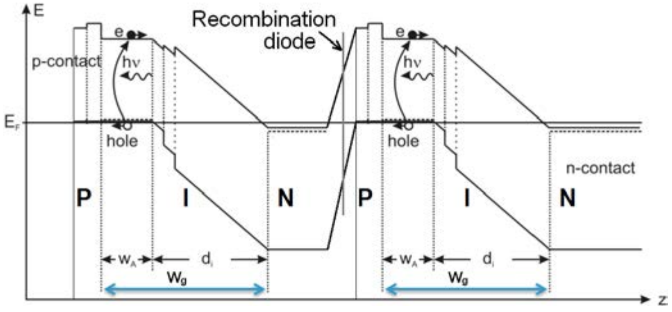

Figure 2.6: Band structure of a two-period *n-i-pn-i-p* diode.

This concept has been demonstrated for both 850 nm [13] and 1550 nm [14]. In Fig. 2.7 [5] the power spetrum emitted by a log-spiral antenna connected to a 3 period *n-i-pn-i-p* photomixer is shown. The advantage of this devices in comparison with photoconductive diodes in terms of power level becomes obvious when comparing Figs. 2.3 and 2.7: 30 times more power is achieved at 200 GHz. A power level of 0.8 mW was obtained at a photocurrent of 17 mA in a operation conditions close to thermal breakdown. The device was a large one with a cross section of 82 μm^2, which results in a RC 3 dB cut-off frequency of 140 GHz [5]. The transit-time 3 dB cut-off frequency is at 1 THz.

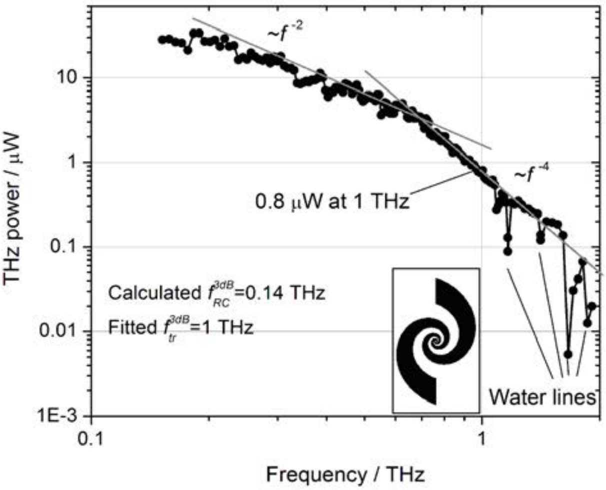

Figure 2.7: Measured THz power for the three-period *n-i-pn-i-p* photomixer connected to a self complementary log-spiral antenna (inset).

2.3 Array of antenna emitters

It is possible to overcome the power limitations in photomixed-based THz sources by combining many antenna emitters [15–17]. For considering array configurations, the sources must have similar coherence properties. This is possible by using same optical source for all photomixers. This was demostrated by Preu et al [16, 18]. In [18], authors use two photomixing sources in a Young's experiment setup for measuring the coherence length. The two combined terahertz sources are split by a beam splitter and fed to the terahertz sources. In [16], it is show how N sources can be combined for increasing the generated THz power. An improvement by N^2 is achieved in the maximum of the radiation pattern [16, 19, 20].

From the manufacturing point of view, the most appealing configuration of sources is the linear or planar array. The radiation pattern $U_{tot}(\theta, \phi)$ is calculated as follows

$$U_{tot}(\theta, \phi) = U_{AE}(\theta, \phi) \cdot |AF(\theta, \phi)|^2 \qquad (2.8)$$

where $U_{_{AE}}(\theta,\phi)$ is the radiation patern for one single element. The array factor $AF(\theta,\phi)$ depends on the element distribution. For photomixing sources, 2D rectangular configurations are of particular interest (Fig. 2.8). For this specific type, the array factor becomes [21]

$$AF(\theta,\phi) = \sum_{m=1}^{M}\sum_{n=1}^{N} I_{mn}\cdot e^{j(m-1)(k\cdot d_x\cdot\sin(\theta)\cos(\phi)+\beta_x}\cdot e^{j(n-1)(k\cdot d_y\cdot\sin(\theta)\cos(\phi)+\beta_y} \tag{2.9}$$

where k is the wave number, I_{mn} is the amplitude of the current of the mn element, d_x and d_y are the distance between elements in the x- and y-direction, respectively; and β_x and β_y are the progressive phase in the x- and y-direction respectively.

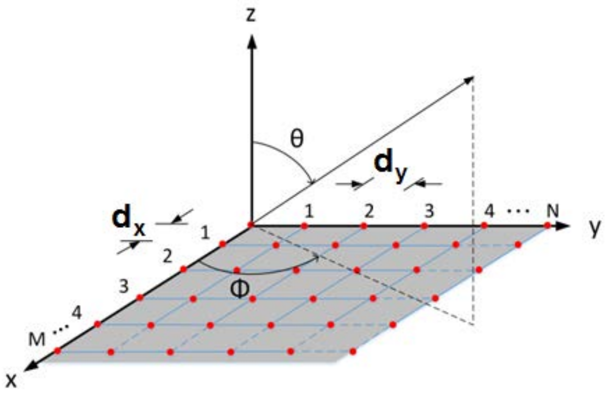

Figure 2.8: Geometry of a 2D rectangular array of MxN elements (red).

The possibility of using arrays of antenna emitters for beam steering was discussed in [22, 23]. The progressive phase for achieving a specific main lobe direction (θ_0,ϕ_0) can be calculated as follows

$$\begin{aligned}\beta_x &= -k\,d_x\sin(\theta_0)\cos(\phi_0)\\ \beta_y &= -k\,d_y\sin(\theta_0)\sin(\phi_0)\end{aligned} \tag{2.10}$$

The size of elements is a obvious lower bound to the array pitch d_x and d_y. Ultra-wideband elements, such as log-spiral and log-periodic AEs are electrically large for the higher frequencies. If the radiation pattern shape is critical for the application, this limits the working band. If a parabolic mirror collect all the radiated power they can be still used for high power generation.

Below, two extra limiting factors are taken into account:

- Optical fiber diameter: if each element is fed by one optical fiber. A single electrically-large lens is placed down the array for increasing the power extracted from the substrate.
- Lenses size: if one lens per element is used, the lens radius is the limiting factor, since electrically-small lenses have smaller emission efficiency (see Section 1.4.1).

Next, both strategies are considered.

2.3.1 Arrays with a single electrically-large lens

Fig. 2.9 shows the calculated radiation pattern of a 3x3 array of horizontal dipole AE (see Section 1.2.2) at 1 THz. It has a spacing between elements of $d_x = d_y = 168\,\mu$m.

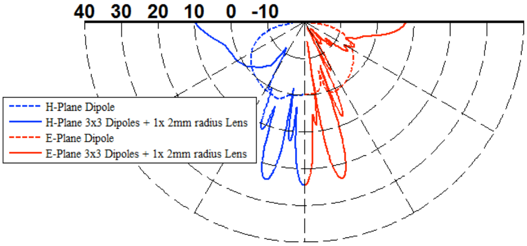

Figure 2.9: Directivity (in dB) of a 3x3 horizontal dipole AE array with $d_x = d_y = 168\,\mu$m and lens of radius $R = 2$mm. Both H-plane (blue) and E-plane (red) are shown for both the single element (dashed) and the array (solid).

As it can be seen, even for coherently driven THz sources, there is no constructive interference, since all elements but the central one are out-of-focus (Fig. 5.1). This effect is confirmed by the experimental results.

Several 5x5 and 3x3 arrays of log-spirals AE (see Section A.1) have been manufactured and measured. A common pitch between elements is $d_x = d_y = 160\,\mu$m, since this allows us to use a commercial 3x3 optical fiber array for illuminating up to 9 devices at the same time. Examples of radiation pattern measurements at 300 GHz are shown in Fig. 2.10. They were measured by illuminating groups of 3x3 elements of the 5x5 array. Despite of the lack of angular resolution, the presence of several lobes can be appreciated in most of them.

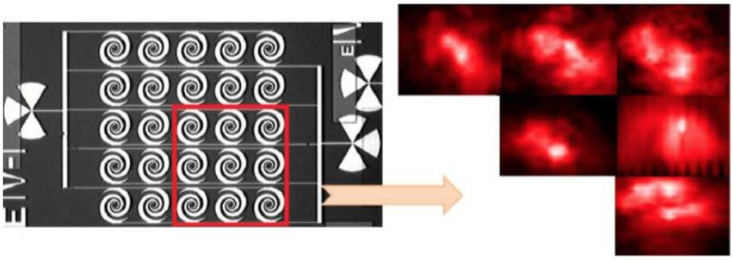

Figure 2.10: Radiation pattern for the spiral arrays [24].

Fig. 2.11 shows the measured terahertz power normalized to the square of the devices photocurrent P_{THz}/A^2 [24,25] for all the elements of the 3x3 array highlighted in red (Fig. 2.10). Terahertz power is collected by using two parabolic mirrors.

There is a 10-100 factor between the normalized power radiated by different elements of the same array. This is consistent with the simulation results, since only the power inside the cone define by the mirror size and its distance to the source is collected by the power receiver (a Golay cell): if an out-of-focus element radiates its main beam out of this cone, the measured power is smaller.

The limiting factor in the pitch of the AE array is the optical fiber diameter ($D = 150\,\mu$m), but a inter-spacings of less than $150\,\mu$m are difficult to achieve. Furthermore, when using the optical fiber array, we

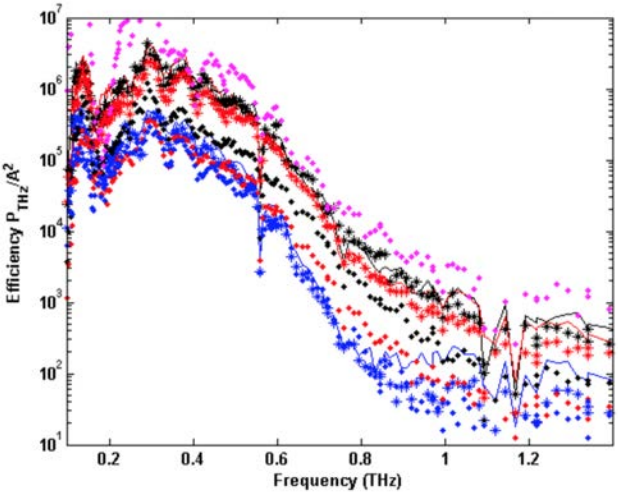

Figure 2.11: Power (normalized to the square of the photocurrent) emitted by each element of the 3x3 array marked in red in Fig. 2.10. Left column elements (red). Central column elements (black). Right column elements (blue). Radiated power by the single element is also shown (pink).

were unable to achieve an uniform optical pump of elements [26], even for only a 2x2 array. By using semiconductor micro- and nano-fabrication techniques, it could be possible to manufacture an optical fiber array holder with the required precision ($\leq 1\,\mu$m [26]).

It is possible to reduce the illumination complexity by using an array of 1550 nm lenses with the same pitch as the array of AEs. Then, a single optical pump creates a large spot in the optical lenses, which would be focused in the photomixers. Depending on the achieved alignment precision, larger or smaller spots could be generated in the AE plane by modifying the distance between lenses and the photomixers. Two bow-tie AE arrays have been manufactured (see Section A.3) with pitches of $150\,\mu$m (Thorlabs MLA150-7AR) and $300\,\mu$m (Thorlabs MLA300-14AR), which corresponds to commercially-available values for arrays of optical microlenses [27]. Fig. 2.12 sketches the design of the $d_x = d_y = 300\,\mu$m 5x5 array. 1550 nm photoconductive terahertz sources are placed in the gaps marked in green. Dummy bow ties around the functional ones prevent the edge effects and serve as biasing pads.

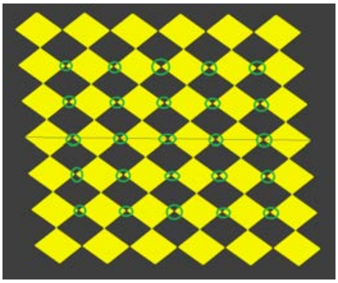

Figure 2.12: Array of bow tie (gold) AEs. Pitch is $d_x = d_y = 300\,\mu$m. AE are marked in green.

2.3.2 Arrays with multiple lenses

When considering one lens per AE, the array becomes sparse if they are electrically large. Then, a radiation pattern with many sidelobes is expected. Fig. 2.13 shows the radiation pattern of the same AE array as in Fig. 2.9 at 1 THz, but considering one lens per device and a pitch $d_x = d_y = 2$mm.

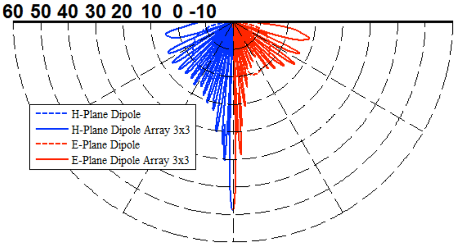

Figure 2.13: Directivity (in dB) of a 3x3 horizontal dipole AE array with $d_x = d_y = 2$mm and one lens per element. Both H-plane (blue) and E-plane (red) are shown for both the single element (dashed) and the array (solid).

The above discussion about the optical fiber alignment precision is applicable here. On the other hand, arrays with pitches $d_x = d_y > 750\,\mu$m can be manually assembled gluing one by one all the optical fibers (see Section 3.2). This is feasible for a prototyping context. In Section 5.2 an array of 1x4 elements is proposed by using DRW antennas (see Chapter 4) instead of lenses, since they have less cross-section area.

2.4 Large area emitter

A LAE is a Terahertz photomixer source. It overcomes the limitation found in other optoelectronic sources such as *n-i-pn-i-p* and photoconductive photomixers by avoiding the limitations in optical power due to the small size of the device. As it was explained before, the RC roll-off and transit time roll-off in *n-i-pn-i-p* sources force a maximum active area [28]. Photoconductives also need optical power focalized in a small region. Small devices suffer of strong heating [28], which increases the risk of thermal failure. Moreover, higher power densities lead to high photo-carrier densities, which could screen the applied DC electric fields required for their transport [28]. Both heating and screening are solved by increasing the device size and, therefore, keeping a feasible density of optical power while increasing its value. This leads to an increase of the terahertz radiated power [19].

Large Area Emitters do not need an external antenna for radiating the generated photocurrent, since each generated photocarrier is assumed to be an independent source. One of each can be assimilated as an elementary Hertzian dipole when subjected to an accelerating DC electric field. This dipole is also known as a Large Area Quasi Dipole (LAQD) [19]. The radiation characteristic can be modeled by considering the contribution of all photocarriers as an array of large area quasi dipoles (LAQDs).

According to the orientation of the DC electric fields, two different topologies are defined: horizontal (Fig. 2.14a) and vertical (Fig. 2.14b) LAE. An incident Gaussian laser beam of radius ρ_0 with two colors of photon frequencies differing by the THz frequency ν_{THz} produces a variable distribution of electrons and holes. This variation is spatially directed parallel to the E_{DC} DC electric fields. Its period corresponds to the THz frequency [19].

Vertical orientation of the photocarrier oscillations can be obtained in an *n-i-pn-i-p* structure (Fig. 2.15a). LAQD length is determined then by the thickness of the layers and is typically of the order of 200 μm. An example of manufactured device design was presented on [29]. It is a 5028x2283 μm^2 (a x b) device with 28 (n) MESAs. W_{MESA} is 165 μm and GAP 12 μm. An InP wafer of 350 μm of thickness (S_{THK})

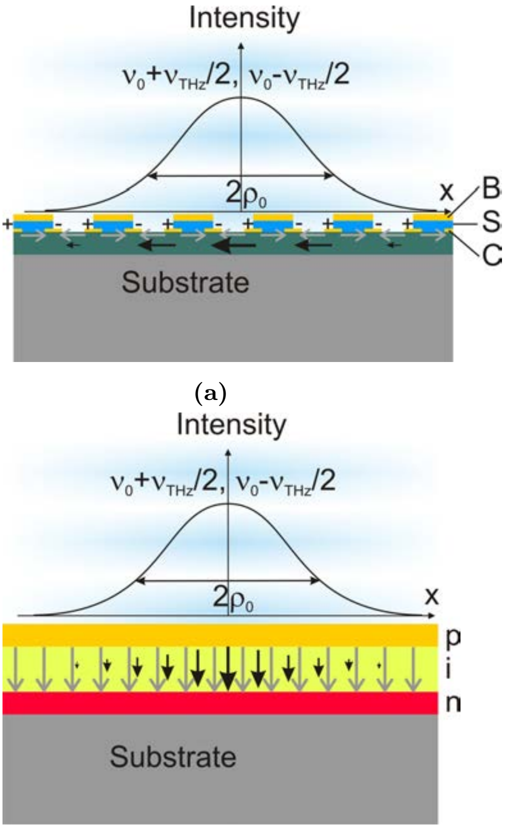

(a)

(b)

Figure 2.14: Schematic diagram illustrating the photomixing process in both vertical (a) and horizontal (b) Large Area Emitters.

was used as a substrate. As stated above, radiation characteristics can be estimated by modeling the contribution of generated photocarriers as an array of LAQD dipoles. Fig. 2.15b sketches an example of model. Each MESA is modeled as an array of N_X x N_Y x N_Z vertical LAQD. Distance between array elements (d) must be chosen small enough for modeling properly both in phase and amplitude the optical Gaussian beam impinging the LAE

$$d \ll min(\rho_0^2, \frac{\lambda_0}{4\sqrt{\varepsilon_{SC}}}) \tag{2.11}$$

The radiation intensity for the vertical ($U_{LAE,v}$) and the horizontal ($U_{LAE,v}$) LAE can be calculated by the product of each LAQD radiation pattern when embedded in the substrate and the array factor AF_{LAE}

$$U_{LAE,v}(\theta,\phi) = U_{LAQD,v}(\theta,\phi) \cdot AF_{LAE}(\theta,\phi) \tag{2.12a}$$

$$U_{LAE,h}(\theta,\phi) = U_{LAQD,h}(\theta,\phi) \cdot AF_{LAE}(\theta,\phi) \tag{2.12b}$$

where $U_{LAQD,v}$ and $U_{LAQD,h}$ are the radiation intensities of the vertical and horizontal LAQD, respectively. When assuming a semi-infinite substrate (see Section 1.2), they can be determined by Eqs. (1.7), (1.10), and (1.11) (vertical LAE), and by Eqs. (1.12) (horizontal LAE), when particularizing the radiation intensity amplitude U_0 to the LAQD case:

$$U_0 = \frac{3}{8\pi} P_{THz}^{id} \tag{2.13}$$

where P_{THz}^{id} is [19]

$$P_{THz}^{id} = \frac{1}{2} R_{LAQD} \left| I_{THz}(\omega_{THz}) \right| \tag{2.14}$$

where the LAQD radiation impedance R_{LAQD} can be estimated from the substrate refractive index $n_{_{SC}} = 1/\sqrt{\varepsilon_{_{SC}}}$ and the photocarriers velocity v_{val}

$$R_{LAQD} = \Big(\frac{2Z_0 n_{_{SC}}}{3\pi}\Big)\Big(\frac{v_{val}}{c}\Big)^2 = 12.8 \cdot 10^{-3}\Omega \tag{2.15}$$

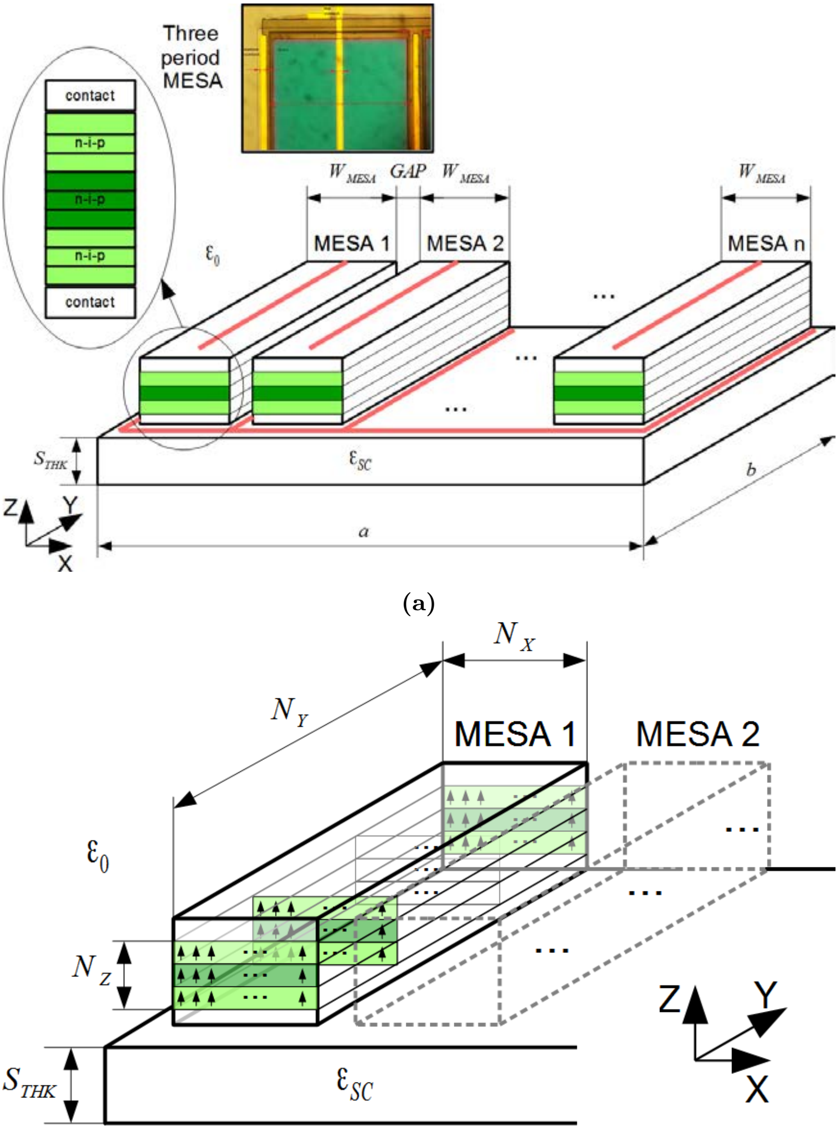

Figure 2.15: Sketch of a Vertical LAE (a). Both top and bottom contacts (red) for DC biasing are shown. Detailed view of the corresponding model using LAQD (b).

where $v_{val} = 2 \cdot 10^8$ cm/s for InGaAs at sufficiently high electric fields (> 3 kV/cm) [19] for a well-designed LAE, $Z_o = 1/\varepsilon_0 c = 377\Omega$ is the impedance of free space and $c = 3 \cdot 10^8$ m/s is the vacuum velocity of light, and I_{THz} is the THz AC current, whose amplitude depends on both the laser power P_{opt} and the frequency ω_{THz}.

When the Eq. (2.11) is fulfilled, the differences between the array factor of a discrete LAE model (such as the one shown in Fig. 2.15b, which can be analytically obtained similarly as in Section 2.3) and a more realistic continuous array factor become negligible [5]. The continuous array factor assumes a continuous distribution of photocarriers. When assuming same coordinates system as in Fig. 2.14, it can be expressed as

$$AF_{LAE}(\theta,\phi) = \Big| \int_a \int_b n(\vec{\rho}) \cdot \exp\big(-i\vec{k}(\theta,\phi) \cdot \vec{\rho}(\rho_x,\rho_y)\big) \cdot d\rho_x d\rho_y \Big|^2 \tag{2.16}$$

where $\vec{\rho} = (\rho_x, \rho_y, 0)$ is the vector from the origin to the THz field source when integrating the LAE area (a x b), and $n(\vec{\rho})$ is the photocarrier density distribution. $n(\vec{\rho})$ depends on the optical beam shape. For an Gaussian beam of radius ρ_0, it calculated as

$$n(\vec{\rho}) = n_0 \cdot \exp\left(- \frac{\rho_x^2 + \rho_y^2}{\rho_0} \right) \tag{2.17}$$

where n_0 is the maximum density of photocarriers in the XY plane, and it is proportional to $P_L/(\pi\rho_0^2)$, being P_L the incident optical power. For an isotropic Gaussian optical beam in the Z-axis direction the continuous array factor is only dependent on θ. The 2D integral can be analytically solved, with the result

$$AF_{LAE}(\theta) = \Big(n_0 \pi \rho_0^2 \Big)^2 \cdot \exp\left(- \frac{1}{2} \Big[k\rho_0 \sin\theta \Big] \right) \tag{2.18}$$

By using equations (2.12) and (2.18) it is possible to calculate the radiation pattern of a LAE. Fig. 2.16 shows radiation intensities of an horizontal (x-axis oriented E_{DC} field) LAE for $\rho_0 =$

$0.1, 0.2, 0.5, 1, 2, 5\lambda_0/n_{SC}$. Since for $\rho_0 < 0.2\lambda_0/n_{SC}$ the array factor is almost isotropic, the radiation patterns become similar to the one calculated for a single dipole lying in a semi-infinite substrate (Fig. 1.8). As expected. Most of the power is radiated into the high-permittivity substrate.

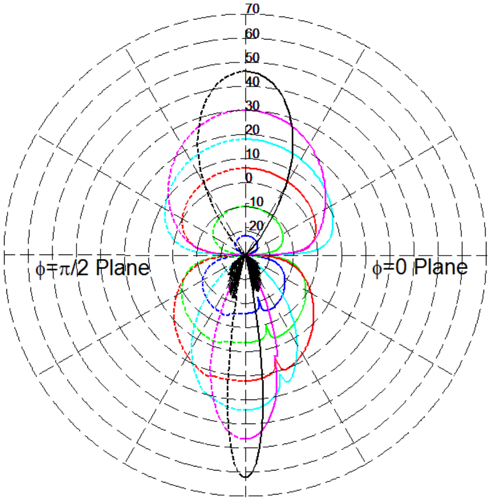

Figure 2.16: Radiation intensities of horizontal LAE with different radius $\rho_0 = 0.1, 0.2, 0.5, 1, 2, 5\lambda_0/n_{SC}$ of the Gaussian optical pump. Photocarriers are accelerated by an electric field parallel to the surface in x-direction. Both E-plane ($phi = 0°$ plane, solid) and H-plane ($phi = 90°$ plane, dashed) are shown for $\rho_0 = 0.1\lambda_0/n_{SC}$ (blue), $\rho_0 = 0.2\lambda_0/n_{SC}$ (green), $\rho_0 = 0.5\lambda_0/n_{SC}$ (red), $\rho_0 = 1\lambda_0/n_{SC}$ (cyan), $\rho_0 = 2\lambda_0/n_{SC}$ (magenta) and $\rho_0 = 5\lambda_0/n_{SC}$ (black).

Same calculations can be done for the vertical LAE by using the radiation pattern of a vertical dipole. When illuminating with an optical beam perpendicular to the device, a much smaller THz power level is expected, since the vertical dipole lying in a semi-infinite substrate has a null in the z-axis (Fig. 1.8). For this family of LAEs an oblique instead of a perpendicular incident beam is chosen. By doing so, it is possible to steer the main lobe of the array factor, which allows to maximize the amount of power radiated into the substrate. Fig. 2.17 sketches the oblique excitation of a vertical LAE. ZX is the plane of incidence.

From the theoretical study, it was found that an angle of incidence

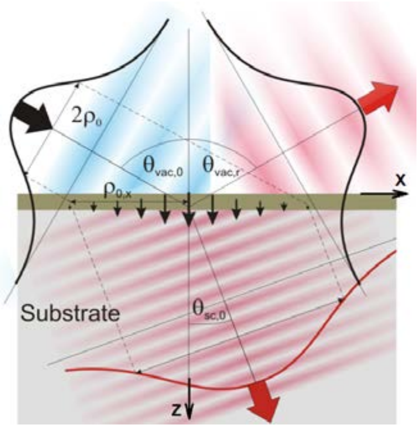

Figure 2.17: Oblique excitation of a vertical LAE. An incident Gaussian optical beam (blue) conforms an angle $\theta_{vac,0}$ with the z-axis. The generated photocarriers are not in phase, which produces a deviation of the terahertz (red) main beam of $\theta_{sc,0}$ with respect to the z-axis.

close to the Brewster angle $\theta_{BR,0} = \arctan(n_{SC}) = 74.48°$ (InGaAs) represents a suitable choice, since the array factor and vertical dipole maximums differ only by 0.6 degree. Calculated radiation pattern for the vertical LAE is shown in Fig. 2.18, for both $\phi = 0°$ (Fig. 2.18a) and Brewster (Fig. 2.18b) planes. The Brewster plane is perpendicular to $\phi = 0°$ and contains the maximum of the radiation pattern.

Despite horizontal LAE are more appealing from the theoretical point of view, they are more difficult to manufacture, especially for CW operation [19]. It is difficult to achieve ballistic transport times while getting rid of field screening due to saturation effects [19].

2.5 Conclusions

The three optoelectronic terahertz sources used in this thesis were described. The main limitations of photoconductive and *n-i-pn-i-p* photomixers were analyzed. For overcoming them, a new device, the LAE, has been proposed. Both photoconductive devices and *n-i-pn-i-p* photomixers manufacturing processes are described in Appendix A.

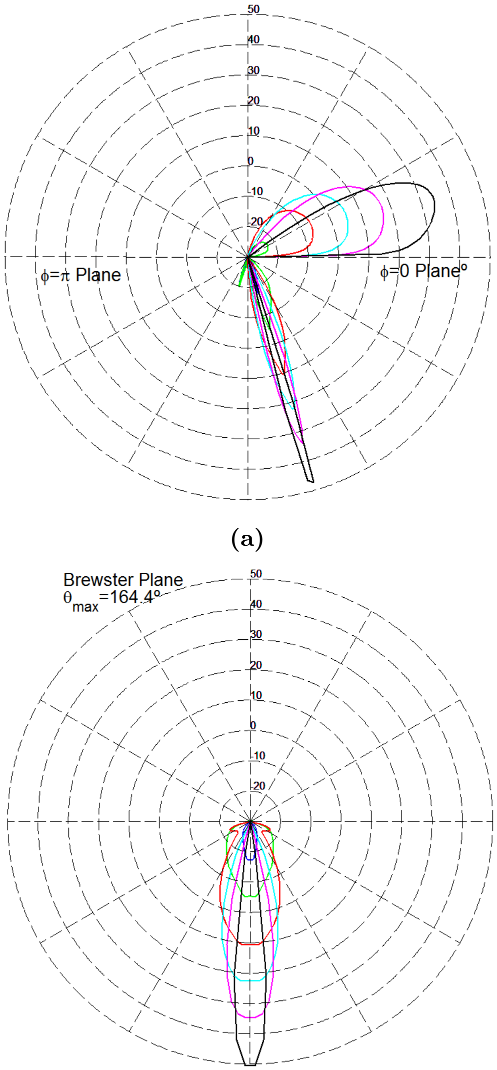

(a)

(b)

Figure 2.18: Radiation intensities of horizontal LAE with different radius $\rho_0 = 0.1, 0.2, 0.5, 1, 2, 5\lambda_0/n_{SC}$ of the Gaussian optical pump. Photocarriers are accelerated by an electric field parallel to the surface in x-direction. Both $phi = 0°$ plane (a) and Brewster plane (b) are shown for $\rho_0 = 0.1\lambda_0/n_{SC}$ (blue), $\rho_0 = 0.2\lambda_0/n_{SC}$ (green), $\rho_0 = 0.5\lambda_0/n_{SC}$ (red), $\rho_0 = 1\lambda_0/n_{SC}$ (cyan), $\rho_0 = 2\lambda_0/n_{SC}$ (magenta) and $\rho_0 = 5\lambda_0/n_{SC}$ (black).

The combination of many discrete terahertz sources has been discussed. Despite on the fact that there is work to do, some preliminary measurement of manufactured arrays have been provided.

As said in Section 2.4, LAEs allows to increase the optical pump power, which leads to an increment on the generated terahertz power with respect to other photomixing sources technologies. A model this device has been proposed. It is based on the work described in Chapter 1.

2.6 References

[1] I. S. Gregory, C. Baker, W. R. Tribe, I. V. Bradley, M. J. Evans, E. H. Linfield, A. G. Davies, and M. Missous, "Optimization of photomixers and antennas for continuous-wave terahertz emission," *IEEE Journal of Quantum Electronics*, vol. 41, no. 5, pp. 717–728, 2005.

[2] E. Peytavit, S. Arscott, D. Lippens, G. Mouret, S. Matton, P. Masselin, R. Bocquet, J. Lampin, L. Desplanque, and F. Mollot, "Terahertz frequency difference from vertically integrated low-temperature-grown GaAs photodetector," *Applied Physics Letters*, vol. 81, no. 7, pp. 1174–1176, 2002.

[3] I. S. Gregory, C. Baker, W. Tribe, M. Evans, H. E. Beere, E. H. Linfield, A. Davies, and M. Missous, "High resistivity annealed low-temperature GaAs with 100 fs lifetimes," *Applied physics letters*, vol. 83, no. 20, pp. 4199–4201, 2003.

[4] I. S. Gregory, W. Tribe, C. Baker, B. Cole, M. Evans, L. Spencer, M. Pepper, and M. Missous, "Continuous-wave terahertz system with a 60 db dynamic range," *Applied Physics Letters*, vol. 86, no. 20, p. 204104, 2005.

[5] G. Carpintero, L. E. García-Muñoz, H. L. Hartnagel, S. Preu, and A. V. Räisänen (Editors), *Semiconductor Terahertz Technology Devices and Systems at Room Temperature Operation.* Wiley, 2015.

[6] N. Khiabani, Y. Huang, L. E. García-Muñoz, Y.-C. Shen, and A. Rivera-Lavado, "A novel sub-THz photomixer with nano-trapezoidal electrodes," *IEEE Transactions on Terahertz Science and Technology*, vol. 4, no. 4, pp. 501–508, 2014.

[7] E. Brown, F. Smith, and K. McIntosh, "Coherent millimeter-wave generation by heterodyne conversion in low-temperature-grown GaAs photoconductors," *Journal of Applied Physics*, vol. 73, no. 3, pp. 1480–1484, 1993.

[8] H. Tanoto, J. Teng, Q. Wu, M. Sun, Z. Chen, S. Maier, B. Wang, C. Chum, G. Si, A. Danner *et al.*, "Nano-antenna in a photoconductive photomixer for highly efficient continuous wave terahertz emission," *Scientific reports*, vol. 3, 2013.

[9] H. Ito, F. Nakajima, T. Furuta, and T. Ishibashi, "Continuous THz-wave generation using antenna-integrated uni-travelling-carrier photodiodes," *Semiconductor Science and Technology*, vol. 20, no. 7, p. S191, 2005.

[10] T. Ishibashi, N. Shimizu, S. Kodama, H. Ito, T. Nagatsuma, and T. Furuta, "Uni-traveling-carrier photodiodes," *RECON no. 20010018262. Journal of The Communications Research Laboratory*, vol. 46, pp. 467–470, 1999.

[11] H. Ito, S. Kodama, Y. Muramoto, T. Furuta, T. Nagatsuma, and T. Ishibashi, "High-speed and high-output InP-InGaAs unitraveling-carrier photodiodes," *IEEE Journal of Selected Topics in Quantum Electronics*, vol. 10, no. 4, pp. 709–727, 2004.

[12] M. N. Feiginov, "Analysis of limitations of terahertz pin uni-traveling-carrier photodiodes," *Journal of Applied Physics*, vol. 102, no. 8, p. 084510, 2007.

[13] G. Döhler, F. Renner, O. Klar, M. Eckardt, A. Schwanhäußer, S. Malzer, D. Driscoll, M. Hanson, A. Gossard, G. Loata *et al.*, "THz-photomixer based on quasi-ballistic transport," *Semiconductor Science and Technology*, vol. 20, no. 7, p. S178, 2005.

[14] S. Preu, F. Renner, S. Malzer, G. Döhler, L. Wang, M. Hanson, A. Gossard, T. Wilkinson, and E. Brown, "Efficient terahertz emission from ballistic transport enhanced n-i-pn-i-p superlattice photomixers," *Applied Physics Letters*, vol. 90, no. 21, pp. 212 115–212 500, 2007.

[15] R. C. Hansen, *Phased Array Antennas.* John Wiley & Sons, 2009, vol. 213.

[16] S. Preu, S. Malzer, G. Döhler, J. Zhang, Z. Lu, and L. Wang, "Highly collimated and directional continous-wave terahertz emission by photomixing in semiconductor device arrays," in *Photonics Europe.* International Society for Optics and Photonics, 2006, pp. 61 940F–61 940F.

[17] N. Shimizu and T. Nagatsuma, "Photodiode-integrated microstrip antenna array for subterahertz radiation," *IEEE Photonics Technology Letters*, vol. 18, no. 6, pp. 743–745, 2006.

[18] S. Preu, S. Malzer, G. Döhler, Q. Zhao, M. Hanson, J. Zimmerman, A. Gossard, and L. Wang, “Interference between two coherently driven monochromatic terahertz sources,” *Applied Physics Letters*, vol. 92, no. 22, p. 1107, 2008.

[19] G. H. Dohler, L. E. García-Muñoz, S. Preu, S. Malzer, S. Bauerschmidt, J. Montero-de Paz, E. Ugarte-Munoz, A. Rivera-Lavado, V. Gonzalez-Posadas, and D. Segovia-Vargas, “From arrays of THz antennas to large-area emitters,” *IEEE Transactions on Terahertz Science and Technology*, vol. 3, no. 5, pp. 532–544, 2013.

[20] A. Rivera-Lavado, L. E. García-Muñoz, G. Dohler, S. Malzer, S. Preu, S. Bauerschmidt, J. Montero-de Paz, E. Ugarte-Muñoz, B. Andrés-García, V. Izquierdo-Bermúdez *et al.*, “Arrays and new antenna topologies for increasing THz power generation using photomixers,” *Journal of Infrared, Millimeter, and Terahertz Waves*, vol. 34, no. 2, pp. 97–108, 2013.

[21] C. A. Balanis, *Antenna Theory: Analysis and Design.* John Wiley & Sons, 2005.

[22] S. Bauerschmidt, S. Preu, S. Malzer, G. Döhler, L. Wang, H. Lu, and A. Gossard, “Continuous wave terahertz emitter arrays for spectroscopy and imaging applications,” in *SPIE Defense, Security, and Sensing.* International Society for Optics and Photonics, 2010, pp. 76 710D–76 710D.

[23] S. Preu, S. Malzer, G. H. Döhler, and L. J. Wang, “Coherent superposition of terahertz beams,” in *SPIE Europe Security and Defence.* International Society for Optics and Photonics, 2008, pp. 71 170S–71 170S.

[24] B. Andres-Garcia, “Enhancing the radiated power in the terahertz band,” Ph.D. dissertation, Universidad Carlos III de Madrid, 2014.

[25] B. Andres-Garcia, L. E. Garcia-Muñoz, D. Segovia-Vargas, S. Preu, S. Malzer, S. Bauerschmidt, G. Döhler, H. Lu, and A. C. Gossard, “High power terahertz photomixer arrays,” in *Proc. 6th European Conf. Antennas and Propagation (EUCAP)*, Mar. 2012, pp. 1007–1010.

[26] S. Preu, private communications.

[27] Website of Thorlabs, https://www.thorlabs.de.

[28] S. Preu, G. Döhler, S. Malzer, L. Wang, and A. Gossard, "Tunable, continuous-wave terahertz photomixer sources and applications," *Journal of Applied Physics*, vol. 109, no. 6, p. 061301, 2011.

[29] A. Rivera-Lavado, J. Montero-de Paz, G. Dohler, L. E. García-Muñoz, S. Preu, S. Malzer, S. Bauerschmidt, and D. Segovia-Vargas, "An antenna-free device for continuous-wave THz emission: Vertical large area emitter," in *9th European Conference on Antennas and Propagation (EuCAP)*, 2015, pp. 1–2.

CHAPTER 3

GENERATION AND DETECTION OF THZ POWER

This chapter describes the measurement and sample preparation setups developed during the experimental work related to this thesis. For a description of the samples manufacturing, please refer to Appendices A and B. The following sections explain the main set-ups that were designed and manufactured for conducting the experiments whose results are shown in the following chapters:

- THz transmission setup: A optoelectronic THz source and a detector (either a optoelectronic receiver or a bolometer) are used for measuring the amplitude of a transmission coefficient.
- Photomixer assembly setup: The assembly of THz sources is described.
- Antenna measurement setup: The previous setup is integrated in a radiation pattern measurement setup. Then, the THz source is replaced with a THz transmitter prototype for characterizing it.
- DRW transmission setup: A vector network analyzer (VNA) is used for measuring the S parameter matrix of DRW (see Chapters 4 and 5).

3.1 Photomixing setup

As said above, two different configurations are possible for detecting the signal of a photomixing THz source: a second photomixer (photo-receiver) or a bolometer.

When pumping the photo-receiver with same optical signal as in the photomixing source, it is possible to modulate the THz signal by adding an AC component to the DC biasing of the source. By detecting the AC component in the receiver photocurrent, a coherent receiver scheme is achieved.

A more simple approach uses a bolometer as a detector. It detects a broad range of wavelengths, so an external lock-in amplifier (and a chopping of the optical pump of the THz source) is needed for recognizing the desired terahertz signal.

Setups for both approaches are described in the following subsections.

3.1.1 Coherent system

GREMA group owns a 1550 nm optoelectronic spectroscopy kit, which is a coherent THz system. Power source is electrically modulated so the achieved dynamic range is maximized by using a lock-in detector. Sketch of the system is provided on Fig. 3.1.

The *Toptica Photonics CW Terahertz Spectroscopy Kit*, also known as *TeraScan 1550*, is an optical heterodine system. An AE is irradiated with two 1550 nm high-power laser diodes (40 mW). Lasers wavelength is tuned by controlling temperature with two thermo-electric coolers (TECs) [2]. Both lasers are combined in a 2x2 PM fiber splitter.

THz source is a InP-based *p-i-n* photomixer originally developed for 1550 nm telecom applications [3, 4]. It is integrated with a 100 μm bow tie antenna and a silicon lens. Radiation patterns were measured in the setup described in Subsection 3.3.1. They are shown in Fig. 3.2. As it can be seen, they have many secondary lobes. Moreover, the main lobe

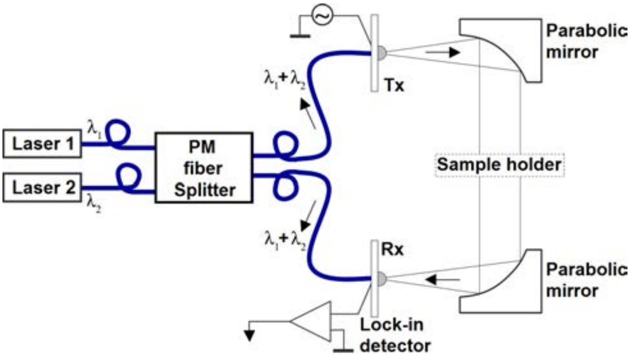

Figure 3.1: *Toptica TeraScan 1550* system sketch [1]. polarization maintaining (PM) fiber (blue) is used to ensure a proper polarization matching in the photomixers ($cos(\beta) = 0$ in Eq. (6)).

has a tilt of ≈ 10° at some frequencies. Since all the radiated power in collected by a parabolic mirror (Fig. 3.1) the radiation pattern is not a critical issue for this kit, which is intended for spectroscopy applications. They can be compared with the radiation pattern (at 150 GHz) achieved by the antenna proposed in Subsection 4.2.2 (Fig. 4.12).

Photomixer is excited with an electrical sinusoid of 1 volt amplitude V_{pp}, -1 volt offset V_{off} and a frequency of 12.20703 kHz. Dymanic range highly depends on the system integration time. According to the manufacturer, it is possible to achieve 90 dB when using 300 ms/step. An intermediate value of 59.97 ms/step is used for the radiation pattern measurments displayed in Fig. 3.2.

Depite using broadband photoconductive sources, the radiation pattern is frequency dependent. At 150 GHz sidelobe level (SLL) is less than 5 dB. As said above, the poor quality of the radiation patterns is not critical as long as most of the THz power is collected by the large enough parabolic mirror. If not, part of the power would be lost due to spill-over. In such case, the dynamic range of the system would be reduced for some frequencies, which would make impossible to recognize spectral signatures with resonances close to these frequencies.

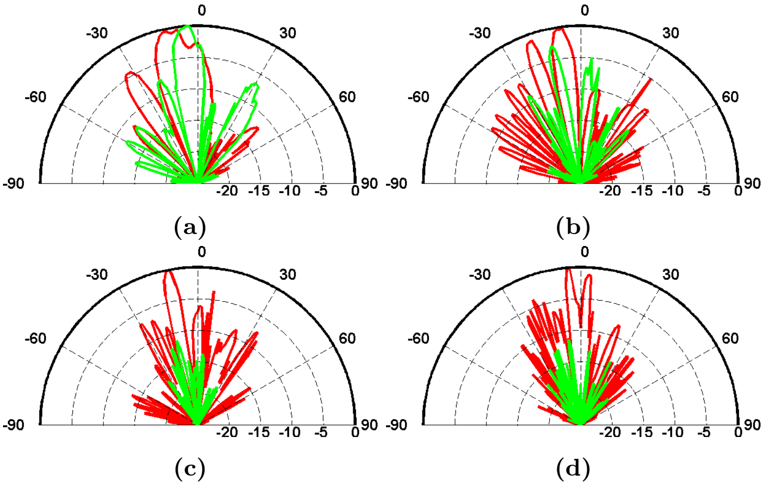

Figure 3.2: Measured radiation patterns (H-plane, copolar) of the *TeraScan 1550* THz photomixing source for 100 GHz (a, red), 150 GHz (a, green), 200 GHz (b, red), 250 GHz (b, green), 300 GHz (c, red), 400 GHz (c, green), 500 GHz (d, red), and 600 GHz (d, green). Each subplot is normalized to the maximum value of its radiation patterns.

3.1.2 Non coherent system

Fig. 3.3 shows a simplified sketch of this system. The receiver has been replaced by a Golay cell, which is a bolometer on which a gas filled cavity with an internal IR absorber. The incident radiation heats up the absorber, which makes the gas to expand. One of the cavity walls is a membrane, whose deformation is measured by a photodiode, which receives a laser beam reflected on the membrane (Fig. 3.4). The detector speed depends on the time required to reach a thermal equilibrium inside the gas cavity. This is defined by the response rate parameter T_R.

The THz power is modulated by chopping the optical pump of the source. Chopping frequency is chosen for increasing the sensitivity of the Golay cell, according to its specifications (see Table 3.1).

Both laser sorces are the same as in the previous setup, so the controller of the *Toptica TeraScan 1550* is used for tuning the lasers and, therefore, setting the THz frequency.

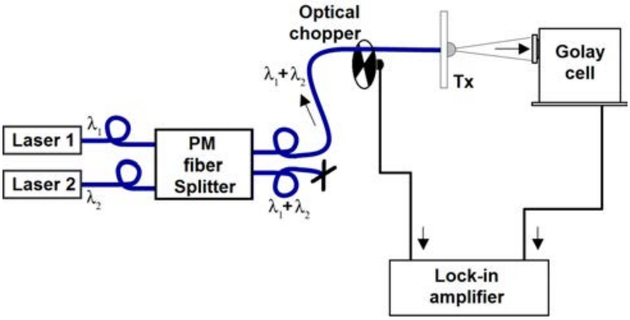

Figure 3.3: Non-coherent setup for characterizing experimental THz sources.

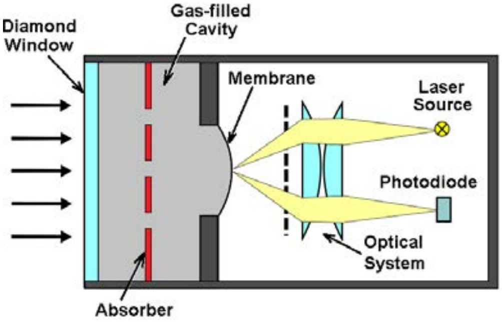

Figure 3.4: Sketch of a Golay cell.

The Golay cell manufacturer [5] also provides an A/D converter. With their software it is possible to determine the received power level by simply configuring a hardware and software gain, reading a voltage level and, finally, multiplying it by the cell responsivity R. Both time domain and spectrum analysis are perform over the analog output of the Golay cell.

Fig. 3.5 shows the spectrum of the output of the bolometer. The laser pump of the photomixer-based source was chopped at 7 Hz. According to the Golay cell responsivity at 150 GHz, a total power of 22.56 nW is being measured.

It is possible to capture the signal by using a locking-amplifier. It allows us to increase the measurement dynamic range. This was the

Param	Value	
Detector	Golay Cell GC-1D (No. GC00148)	
Power supply	GC-PS/1 (No. PS10028)	
Horn aperture	11 mm	
Window aperture	5 mm	
Frequency	5 Hz	10 Hz
NEP	$9.66 \cdot 10^{-11}$ V/$\sqrt{\text{Hz}}$	$9.09 \cdot 10^{-11}$ V/$\sqrt{\text{Hz}}$
R	$1.64 \cdot 10^{5}$ V/W	$1.02 \cdot 10^{5}$ V/W
T_R	39 ms	39 ms

Table 3.1: Technical data and specifications of the TYDEX Golay cell owned by GREMA.

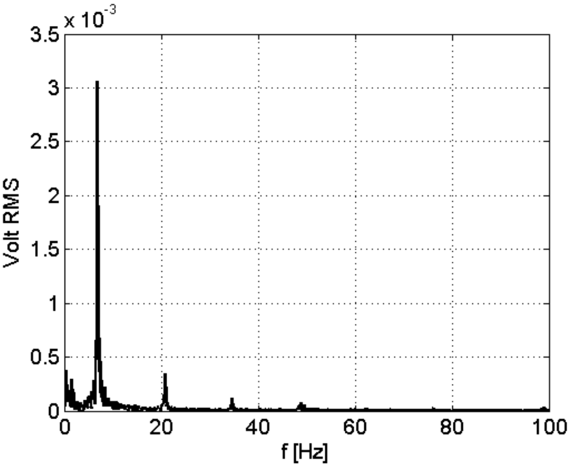

Figure 3.5: Spectrum example of the Golay cell analog output.

chosen option for integrating the non-coherent system in a radiation pattern measurement setup, as is described in the following section.

3.2 Device packaging

The packaging procedure for THz photomixing sources is described in this section. It was developed according to the manufacturing capabilities of the GREMA.

Firstly, a proper glue was found. Three samples of high-resistivity low-permittivity epoxy glues are selected at first: Hysol 9492 [6], Macrocast CR6127 [7] and Hysol 3421 [8]. They are initially found appropriated for gluing most of the AE substrates and optical fibers [9]. A few glue samples are prepared (Fig. 3.6a) and characterized with the setup described in Subsection 3.1.1 (Fig. 3.6b), since the manufacturer does not provides any high frequency characterization. Glue samples of 30 mm x 10 mm x 3 mm are cured in a silicone mold [9] and fixed in a iris between the two parabolic mirrors. The iris diameter is tuned for increasing the receiver photocurrent without any sample $I_{pd,0}$ and kept constant for the rest of measurements.

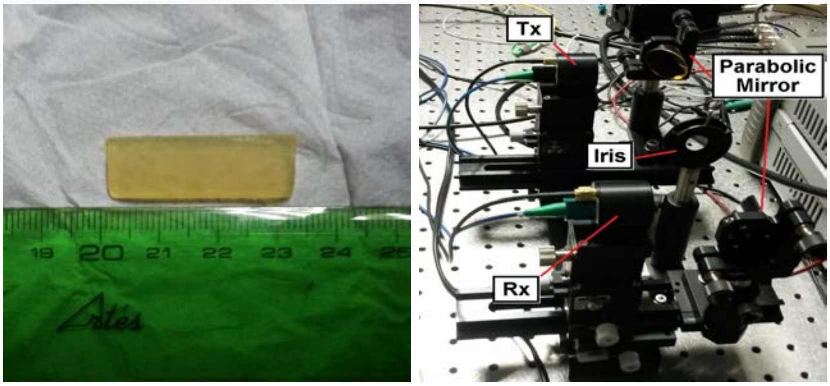

(a) **(b)**

Figure 3.6: Glue samples (a) are placed in a iris (b) of a coherent spectroscopy system (see subsection 3.1.1).

Only attenuation L in the received power is measured from 50 GHz to 1 THz, so it is not possible to obtain both losses and permittivity. The attenuation for a specific sample is calculated from the measured photocurrent $I_{pd,glue}$ as follows

$$L[dB/mm] = 10 \cdot \log_{10}\left(\frac{I_{pd,0}}{T \cdot I_{pd,glue}}\right) \tag{3.1}$$

where $T = 3$ is the sample thickness in millimeters. On the other hand, both must be as small as possible for reducing the impact on the AE performance. Therefore, the candidate with the smallest attenuation is chosen. Results are shown in Fig. 3.7. Hysol 3421 is found to be the most suitable for frequencies beyond 300 GHz. Three different Hysol 3421 samples are displayed for checking the repetition of the characterization procedure. It is used for attaching the DRW antenna to the AE (see Subsection 4.2.2 and Fig. 3.8a), and then, to a 1 inch diameter foam disc (Fig. 3.8b).

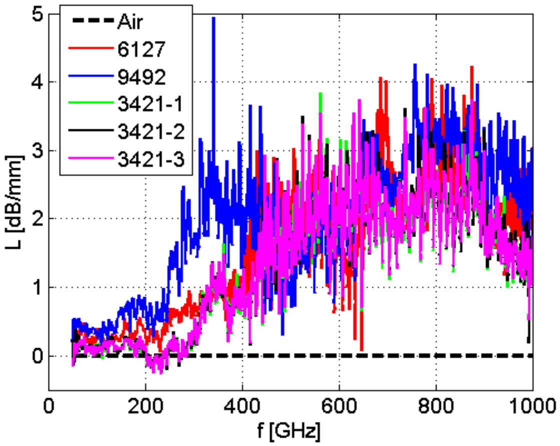

Figure 3.7: Glue characterization in the sub-terahertz and terahertz frequencies. Atenuation is obtained when normalizing the receiver photocurrent to the case without any sample in the iris (black, dashed). Different glues has been tested (solid).

Secondly, the biasing contacts of the device are done. A small pcb (Fig. 3.9) is manufactured an glued close to the AE. A 0.5 mm thick FR-4 subrate is chosen because it has a similar thickness and smaller permittivity than the AE substrate (InP). Contact between FR-4 and the biasing pads is done by glue bonding [10]. When distance between FR-4 pcb and semiconductor is too high, copper wires with silver ink or conductive epoxy are used to ensure electrical contact. Copper wires are soldered in the FR-4 pads. Moreover, the board layout offers enough

(a) **(b)**

Figure 3.8: Device assembly: The AE is glued to the DRW antenna: photo (a) shows a Log-periodic AE glued to a H-plane tapered DRW antenna. Secondly, it is centered and aligned to the axis of a 1 inch diameter 3 mm thick foam disc. Two micropositioners with customs holders are used in this step.

room for an electrical protection circuit made of surface-mount device (SMD) discrete components.

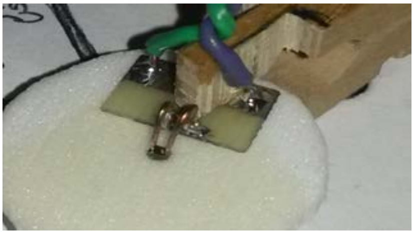

Figure 3.9: Biasing contacts for an AE.

First devices do not have a protection circuit, since they were used for a DC characterization. Fig. 3.10 shows the I-V curve of a 3-period *n-i-pn-i-p* photomixer (see Sections 2.2 and A.2). It was done in three different illumination conditions. For this, a Keysight B2985A picoammeter is controlled through general purpose instrumentation bus (GPIB) with an in-house MATLAB [11] software developed during the realization of this thesis (Fig. 3.11).

At this point, all devices are tested before any further step. For this, a biasing current is applied for determinate its polarity. Then, they are

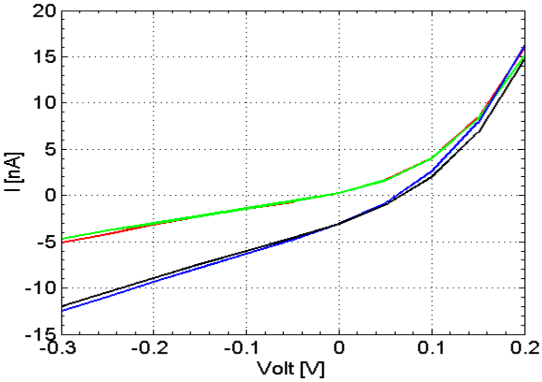

Figure 3.10: I-V curve of a *n-i-pn-i-p* photomixer. It is tested both in dark conditions (green and red) and illuminated with a tungsten lamp (black and blue). The density of power is unknown. Two sweeps were taken for showing the repetition of the measurement.

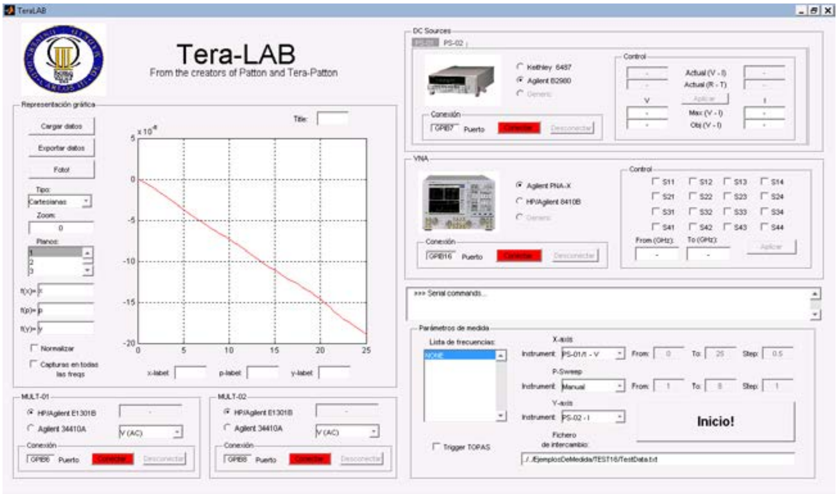

X-axis
Instrument: PS-01/I - V From: 0 To: 25 Step: 0.5

P-Sweep
Instrument: Manual From: 1 To: 8 Step: 1

Y-axis
Instrument: PS-02 - I

Fichero de intercambio: ./../EjemplosDeMedida/TEST16/TestData.txt

Figure 3.11: TeraLAB software was made for characterizing devices both in DC and RF. It talks via GPIB with a combination of power sources, multimeters, picoammmeters and a VNA for 1D a 2D parameter sweeps.

reverse biased. A chopped (4-7 Hz) optical pump is provided to the devices for checking the photocurrent. Finally, an optical fiber is aligned to the photomixer and glued. The alignment is checked and adjusted if needed during the whole curing process, since the volume of epoxy glue decreases. A picture of the alignment setup is shown on Fig. 3.12.

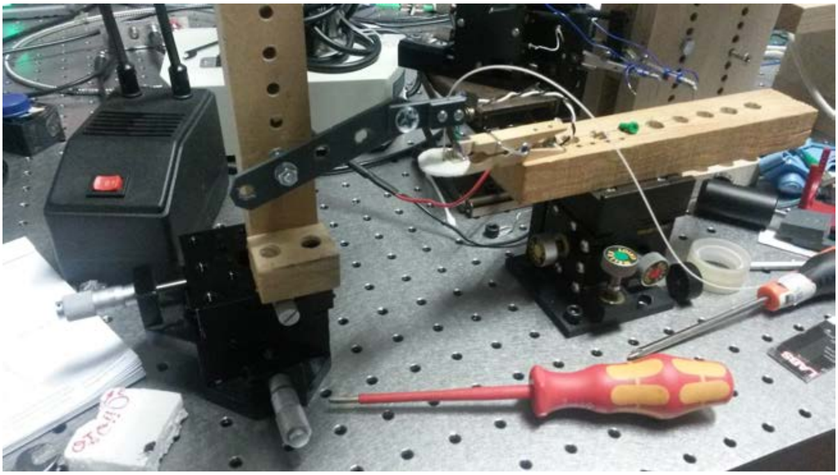

Figure 3.12: Alignment setup: Two micropositioners and a microscope are used for aligning the photomixer and he optical fiber.

Finally, the device is definitely encapsulated with epoxy glue. Because of the standard diameter of the foam disc, assembled sources can be easily integrated in more complex systems using lens holder Fig. 3.13a. The radiation pattern measurement setup described in Subsection 3.3.1 was specifically designed for this prototype. For a well-pigtailed device, an phase center alignment better than 200 μm is easily achieved (Fig. 3.13b).

3.3 Antenna pattern measurement

For the radiation pattern acquisition, two different setups were used: a spherical far field setup and a 2D planar scanner. The first one was developed during this thesis in the THz lab of the Carlos III University of Madrid, in Leganés, Spain. The second one is owned and operated by the Department of Radio Science and Engineering (MilliLab), at Aalto University in Espoo, Finland.

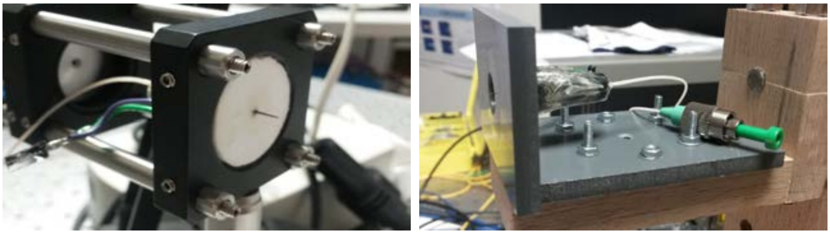

(a) (b)

Figure 3.13: Device assembly: The AE is glued to the DRW antenna (a). Secondly, it is centered and aligned to the axis of a 1 mm diameter foam disc. Two micropositioners with customs holders are used in this step.

3.3.1 Spherical far-field setup

In this subsection, the setup developed for measuring radiation patterns in GREMA's THz lab is described. It is sketched in Fig. 3.14. Either coherent and non-coherent THz measurement setups are supported by the software controller.

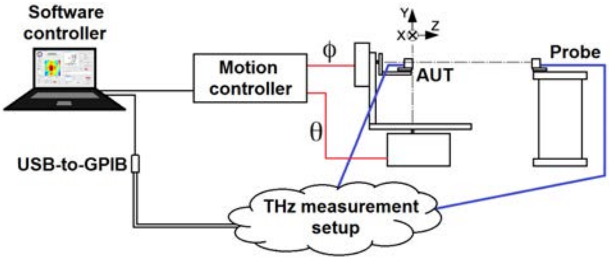

Figure 3.14: Sketch of the spherical radiation pattern measurement setup. A laptop with the software controller installed talks via serial-to-USB with the motion controller. It powers both axis θ and ϕ motors (red wires). Laptop also reads and controls the chosen THz measurement setup via either universal serial bus (USB) or GPIB. Both optical fiber and cables connects the antenna under test (AUT) and the probe with instrumentation equipments (blue), according to the specific setup details.

The coherent setup integrates the *Toptica TeraScan 1550* system for radiation pattern measurements. Both system transmiter or receiver can be exchange with prototypes as long as the following are taken into account:

- Devices must work at a wavelength of 1550 nm. Accepted power must be equal or greather than 80 mW.
- Electric compatibility: despite it is sill possible to adapt both amplitude V_{pp} and offset V_{off} device must work at the frequency of the heterodyne setup.

Partial communication betwen the THz setup and software controller is supported. *Toptica TeraScan 1550* has its own control software, *Topas*. It communicates with the *Toptica* USB hardware drivers via a transmission control protocol (TCP) local connection. Manufacturer provides labview drivers but no other communication mechanism, not even hardware triggers. Despite it could be possible to sniff and inject commandos in the TCP data channel, it is not supported by the company. Chosen strategy lays on the *Topas* possibility to run successive frequency sweeps saving data in text files. The software controller of the setup waits to the generation of the corresponding datafile before moving the positioner to the next point. By setting a wait time between *Topas* sweeps, synchrony is achieved.

Non-coherent setups for terahertz sources can be used by using the Golay cell as probe. For that, the software talks with a Standford Research Systems SR830 DSP Lock-in Amplifier. A Thorlabs MC2000 Optical Chopper is used as a reference generator and as a laser modulator.

The antenna positioner (Fig. 3.15a) was designed with a limitation of €100 in the hardware expenses. Because of this, wood is chosen instead of any metal for the positioner parts. Ambient moisture must be keep low for ensuring durability, which is not difficult to achieve due to the dry climate of Madrid. On the other hand, wood is machined easily. It is possible to keep the positioner in working condition by checking the tight of the screws twice per year.

The motion controller is implemented with an Arduino Mega 2560 [12]. Two 12 volt DC motors control both phi and theta axis of the

(a)

(b)

Figure 3.15: Radiation pattern measurement setup (a). Software controller graphical user interface (GUI) (b). This in-house software was developed using MatLAB platform.

antenna positioner. An 4-channel L298 dual full-bridge driver is used for both motors axis. For each axis, an Agilent HEDS-9711 optical encoder with a Ruhlatec circular strip (part no. C4557-80019) with 7200 marks per revolution ensures a precision of 0.05° in the angle measurement. For avoiding vibrations, controller software set positioning tolerance to 0.2 degrees. It is possible to improve it (up to 0.05°) by tuning both mechanics (adding axis friction in bearings by tightening screws) and motor speed. Since wood is sensible to moisture readjusting of speed parameters is eventually required.

Despite of using interruptions inputs for the optical encoders, the Atmel 2560 microcontroller performance limits the steps per second that can be detected for both axis. Axis speed is then consequently reduced. If not, a failure of following encoder ticks would led to inconsistent angular information. This can be solved by using a more powerful platform, such as *Raspberry Pi* [13] or similar, but prices would increase far from established goal. It is scheduled to increase the hardware capabilities by upgrading the motion controller.

The control and processor software (Fig. 3.15b) is implemented under MATLAB [11]. Instead of doing a constant-speed sweep, it moves the positioner to a specific point. When convergence is ensured, measurement is taken, which increases the precision at the expense of increasing the scanning time.

Additionally, it is also possible to control the Agilent N5247A PNA-X via GPIB for adquiring S parameters (phase and amplitude) while scanning in both phi and theta. With OML V10VNA2-T/R and OML V08VNA2-T/R Millimetre-wave VNA extenders the setup can carry out radiation pattern measurements in the 75 GHz - 110 GHz and the 90 GHz - 140 GHz range with limitations in the antenna weight.

3.3.2 Planar far-field setup

Planar scanners are quite convenient for near-field range measurements. Radiation patterns can be obtained after the proper post-process. When ensuring enough distance between AUT and probe it is also possible to obtain directly the far field (FF) radiation characteristic without any transformation. Typically this is sub-optimum both in terms of scanning points and time. Moreover, only a narrow region of the sphere can be scanned (ideally, half of the sphere with an infinite planar scanner).

Despite of this, a planar scan for FF range measurements is still useful when measuring high-directivity antennas, where only a small solid angle close to the unique main bean is of interest. In this setup (Fig. 3.16a), an NSI 2D scanner is placed facing an optical table. An AB Millimetre millimeter vector network analyzer (MVNA) running from 8 to 350 GHz with two head extensions, a ESA-1-A-FC-2 source system and a ESA-2-FC detection system, is used for measuring both phase and amplitude of the S_{21} parameter. A windows PC running labview [14] is used for running the motors controller and storing the data.

A rectangular waveguide probe is used as a range antenna, in the receiver side. AUT is placed in the transmitter side. Eccosorb VFX-2 absorbers were used to control the reflections in the critical zones. Fig. 3.16b shows an example of DRW antenna (see subsection 4.2.1) measurement setup.

3.4 DRW measurement setup

A VNA with two rectangular waveguide head extensions can be use for characterizing the propagation inside a DRW. Two different configurations were used for obtaining the S parameters of dielectric waveguides:

- 4-ports Agilent N5247 PNA-X with two WR-10 OML V10VNA2-T/R head extensions. This setup is in the THz lab of the GREMA (Carlos III University of Madrid, Spain).
- 2-ports HP8530 VNA with two WR-10 HP W85104A head extensions. This setup is in the sub-mm lab of the MilliLab (Aalto University, Finland).

Fig. 3.17 shows a photo of both setups. The DRW holder is made of low density foam and glued with epoxy. Teflon strip should be used for avoiding contact between the rod and the rectangular waveguides in

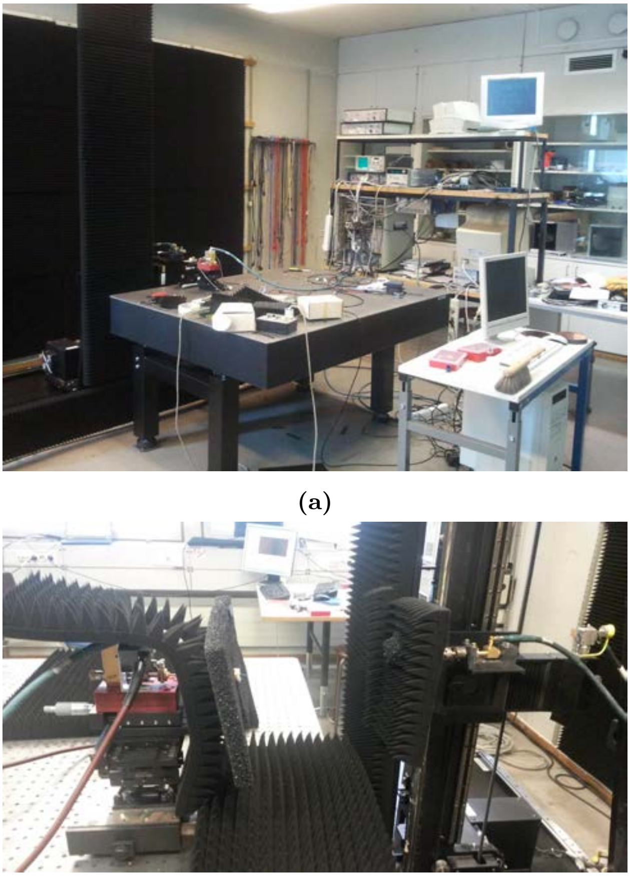

(a)

(b)

Figure 3.16: Radiation pattern measurement setup. Planar scanner (a). Detailed view when measuring a DRW antenna (b).

both ports. Heads should be mounted on 3 axis micropositioner while keeping the DRW holder in a fixed position. When using a optical table, a good alignment between heads can be easily achieved by fixing them to the surface. In this case, only a 3-axis micropositioner for tuning the DRW position is needed. The OML V10VNA2-T/R are shipped with Nylon 6/6 screw legs, but an extra fixation to the table is needed, since they do not conform a stable and precise enough holder.

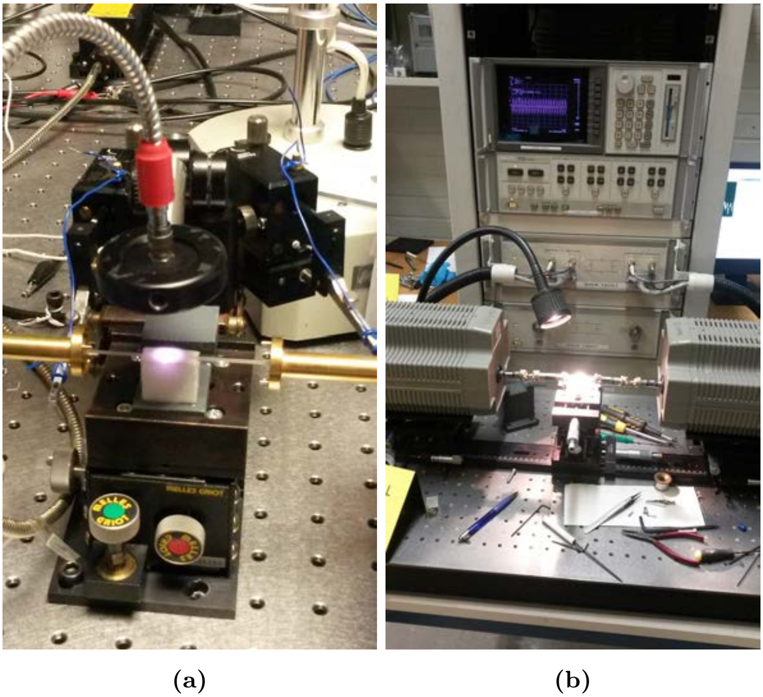
(a) (b)

Figure 3.17: DRW measurement setups at GREMA (a) and MilliLab (b) laboratories. Both experiments are related to the phase shifter that is described in Section 5.3

3.5 Conclusions

The packaging of photomixing THz sources and the measurement setups developed for this thesis have been described. Experimental work was done in the labs of MilliLab (at Aalto University, Espoo, Finland) and GREMA (at Carlos III University of Madrid, Leganés, Spain) research groups.

3.6 References

[1] A. J. Deninger, T. Göbel, D. Schönherr, T. Kinder, A. Roggenbuck, M. Köberle, F. Lison, T. Müller-Wirts, and P. Meissner, “Precisely tunable continuous-wave terahertz source with interferometric frequency control,” *Review of Scientific Instruments*, vol. 79, no. 4, p. 044702, 2008.

[2] D. Stanze, A. Deninger, A. Roggenbuck, S. Schindler, M. Schlak, and B. Sartorius, “Compact cw terahertz spectrometer pumped at 1.5 μm wavelength,” *Journal of Infrared, Millimeter, and Terahertz Waves*, vol. 32, no. 2, pp. 225–232, 2011.

[3] H.-G. Bach, A. Beling, G. G. Mekonnen, R. Kunkel, D. Schmidt, W. Ebert, A. Seeger, M. Stollberg, and W. Schlaak, “InP-based waveguide-integrated photodetector with 100-GHz bandwidth,” *IEEE Journal of Selected Topics in Quantum Electronics*, vol. 10, no. 4, pp. 668–672, 2004.

[4] A. Beling, H.-G. Bach, G. G. Mekonnen, R. Kunkel, and D. Schmidt, “Miniaturized waveguide-integrated pin photodetector with 120-GHz bandwidth and high responsivity,” *IEEE Photonics Technology Letters*, vol. 17, no. 10, pp. 2152–2154, 2005.

[5] Website of TYDEX,
http://www.tydexoptics.com/.

[6] Website of Loctite,
http://www.loctite.co.uk/loctite-4087.htm?nodeid=8802629320705.

[7] Website of Henkel Ltd.,
http://www.henkel-adhesives.co.uk/2838_UKE_HTML.htm?
nodeid=8802700132353.

[8] Website of Loctite,
http://www.loctite.co.uk/loctite-4087.htm?nodeid=8802624405505.

[9] M. Pantoja-Ruiz, private communications.

[10] S. Preu, private communications.

[11] Website of MatLAB,
http://www.mathworks.com/products/matlab/.

[12] Website of Arduino,
https://www.arduino.cc/.

[13] Website of the Raspberry Pi Foundation,
https://www.raspberrypi.org/.

[14] Website of National Instruments about Labview,
http://www.ni.com/labview/esa/.

CHAPTER 4

DIELECTRIC ROD WAVEGUIDE ANTENNAS

In this chapter, an alternative to dielectric lenses is presented for reducing the amount of terahertz power scattered in the high permittivity substrate. Silicon lenses, which are mostly suitable choice for combining with AEs, are able to extract most of the power (see Section 1.4) from the semiconductor, but their cost is in the order of hundreds of euros. This is a mayor barrier for opening the terahertz technology to the mass market. A cost-affordable alternative is critical for developing future consumer electronics.

Rectangular dielectric rod waveguide is a well-known waveguide technology. DRWs can be easily tapered for either coupling field into it or out from it. They can be efficient radiators with a long-enough taper. Their manufacture only requires few simple steps leading to cost-affordable components. It is possible to include other active or passive structures, such as amplifiers [1], directional couplers [2] and phase shifters [3] offering a huge versatility.

First, a brief overview of the theory concerning DRWs is presented. A method for estimating fundamental and higher-order modes in DRW is described. Then, the main parameters concerning the radiation properties are highlighted. Next, the excitation of DRW is studied: both rectangular waveguide and photomixing sources lying on high-permittivity substrates are considered. Finally, a novel proposal for increasing the bandwidth of these antennas when fed by AEs is presented.

4.1 Dielectric rod waveguides

DRW with circular cross-sections are well-studied, since an analytical solution can be found in terms of the Bessel functions for the fundamental mode HE_{11} [4]. Nonetheless, this kind of dielectric waveguides are difficult to manufacture.

This thesis is focused on DRW with a rectangular cross-section, since its ease of manufacture makes them cost-affordable, even when using high-permittivity materials such as silicon and GaAs. Despite of the lack of analytical solutions for calculating the structure modes some approximations, such as Marcatilli's [5] and Goell's [6] methods has been proposed. An sketch of the cross-section of a infinite rectangular DRW along the Z-axis is given in Fig. 4.1.

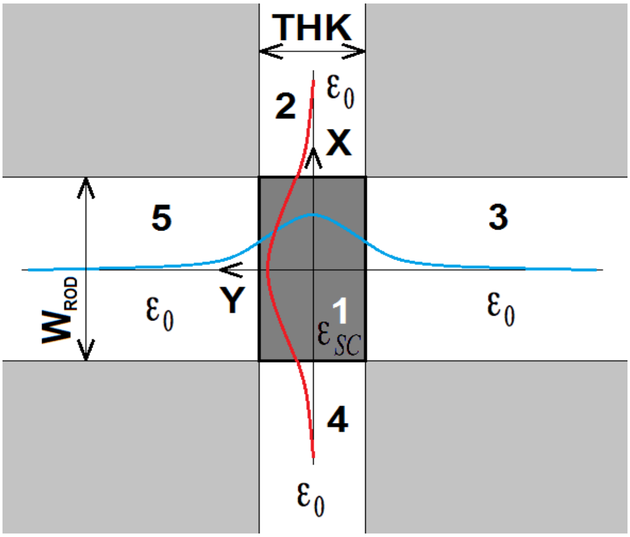

Figure 4.1: Cross section of a rectangular DRW.

When assuming a field perpendicular to the Z-axis, two families of transverse electromagnetic mode (TEM) modes are defined: the E^x_{pq} and E^y_{pq} [4,5,7]. Superscripts x and y indicate the main polarization direction of the electric field, being the others components negligible, according to Marcatilli's approximation. p and q subscripts indicate the number of nulls in the field derivative along the X and Y axis, respectively. Fig. 4.1 sketches the field distribution of the fundamental mode E^x_{11}. Field has a single maximum along both X and Y axis, which is in the center of the waveguide cross-section. Both the E_x (red) and H_y (blue) field components follows a cosinusoidal distribution inside the DRW. Outside, they decrease exponentially. The shadowed zones are not taken into account in this analysis. Expressions of the E and H field components are given in [5] for the five regions denoted $i =$ from 1 to 5:

$$H_{x,i} = 0 \tag{4.1a}$$

$$H_{y,i} = \exp(-jk_z z + j\omega t)\begin{cases} M_1\cos(k_x x + \beta_1)\cos(k_y y + \beta_2) & \text{for } i = 1 \\ M_2\cos(k_y y + \beta_2)\exp(-k_{x,0}x) & \text{for } i = 2 \\ M_3\cos(k_x x + \beta_1)\exp(k_{y,0}y) & \text{for } i = 3 \\ M_4\cos(k_y y + \beta_2)\exp(k_{x,0}x) & \text{for } i = 4 \\ M_3\cos(k_x x + \beta_1)\exp(-k_{y,0}y) & \text{for } i = 5 \end{cases} \tag{4.1b}$$

$$H_{z,i} = -\frac{j}{k_z}\frac{\partial^2 H_{y,i}}{\partial x \partial y} \tag{4.1c}$$

$$E_{x,i} = -\frac{k_0^2 n_{r,i}^2 - k_{x,i}^2}{\omega\varepsilon_0 n_{r,i}^2 k_z} H_{y,i} \tag{4.1d}$$

$$E_{y,i} = -\frac{1}{\omega\varepsilon_0 n_{r,i}^2 k_z}\frac{\partial^2 H_{y,i}}{\partial x \partial y} \tag{4.1e}$$

$$E_{z,i} = \frac{j}{\omega\varepsilon_0 n_{r,i}^2}\frac{\partial H_{y,i}}{\partial y} \tag{4.1f}$$

where M_i are amplitude coefficients, n_i the refraction index of medium i, β_1 and β_2 are phase constants, $k_{x,2-5} = k_{x,0}$ and $k_{y,2-5} = k_{y,0}$ are the decaying factors outside the DRW, and $k_{x,1} = k_x$, $k_{y,1} = k_y$ and k_z are the axial propagation constants inside the rod, approximated as follows when rod is fully surrounded by air ($\varepsilon_0 = 1$) for the E^x_{pq} modes family

$$k_x \approx \frac{p\pi}{W_{ROD}}\Big(1 + \frac{2A_0}{\pi\varepsilon_{SC}W_{ROD}}\Big)^{-1} \tag{4.2a}$$

$$k_y \approx \frac{q\pi}{THK}\Big(1 + \frac{2A_0}{\pi THK}\Big)^{-1} \tag{4.2b}$$

$$k_z = \sqrt{k^2_{SC} - k^2_x - k^2_y} \tag{4.2c}$$

and for the E^y_{pq} modes family

$$k_x \approx \frac{p\pi}{W_{ROD}}\Big(1 + \frac{2A_0}{\pi W_{ROD}}\Big)^{-1} \tag{4.3a}$$

$$k_y \approx \frac{q\pi}{THK}\Big(1 + \frac{2A_0}{\pi\varepsilon_{SC}THK}\Big)^{-1} \tag{4.3b}$$

$$k_z = \sqrt{k^2_{SC} - k^2_x - k^2_y} \tag{4.3c}$$

being

$$A_0 = \frac{\pi}{\sqrt{k^2_{SC} - k^2_0}} = \frac{\lambda_0}{2\sqrt{\varepsilon_{SC} - 1}} \tag{4.4}$$

Having the propagation constant approximated, it is possible to optimize the waveguide dimensions W_{ROD} and THK for a specific frequency range for a single-mode E^x_{11} propagation regime. For the 75 - 110 GHz frequency range the optimum dimensions are $W_{ROD} = 1$ mm and $THK = 0.5$ mm when considering silicon or GaAs ($\varepsilon_{SC} \approx 12$). [7–10]. Fig. 4.2 shows the estimated modal chart for both E^y_{pq} (black) and E^y_{pq} (red) modes families. Its axes are normalized. The ordinate corresponds to

$$\frac{k^2_z - k^2_0}{k^2_{SC} - k^2_0} \tag{4.5}$$

which takes values from 0 to 1. The abscissa is a function of k_0 that takes into acount the waveguide thickness THK and permittivities.

$$\frac{2 \cdot THK}{\lambda_0}\sqrt{\varepsilon_{SC} - 1} \tag{4.6}$$

The 75 - 110 GHz frequency range corresponds to the 0.84 - 1.24 abscissa range. In this frequency range only the E^x_{11} fundamental mode is propagating. It is also possible to excite the E^y_{11} mode if the feeding is not properly designed. Both E^x_{11} and E^y_{11} modes do not have a cut-off frequency. Marcatilli's approximation is not accurate for lower frequencies, since it wrongly predicts such a lower frequential limits for both fundamental modes.

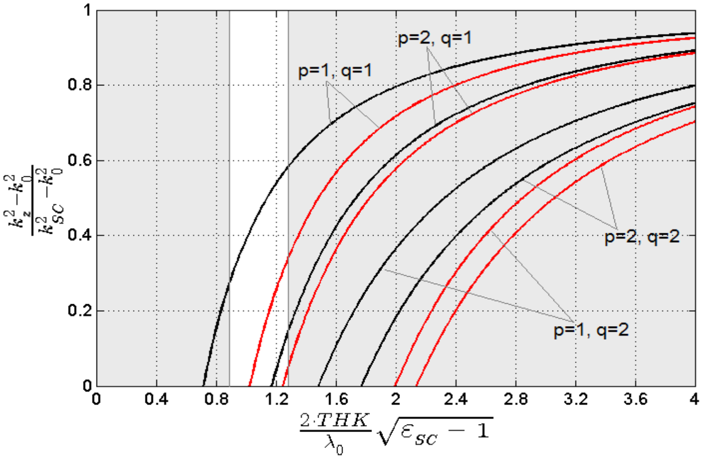

Figure 4.2: Axial propagation constant k_z. Both axis are normalized according to the criteria used in [5].

This waveguide design is used in Subsections 4.2.1 and 5.1 for designing antennas working at such frequencies.

Subsection 4.2.2 shows how an electrically large DRW antenna fed by a spherical source exhibits Brillouin waves in the rod due to total internal refections. In such case, the Marcatilli's assumption is not valid. E-field distribution cannot be defined as a contribution of different TEM modes. A solution for avoiding such non-TEM modes inside the rod is proposed in Subsection 4.3.

4.2 DRW antennas

As mentioned in the introduction of this chapter, a dielectric rod waveguide can properly radiate the power to the air by simply tapering it. This can be done in E, H, both planes or in more complex configurations (Fig. 4.3). Tapering in one single plane is the simplest choice and, according to simulations, can be efficient from the point of view of the radiation properties. It is show that tapering in the E-plane is slightly better than in the H-plane [11–13].

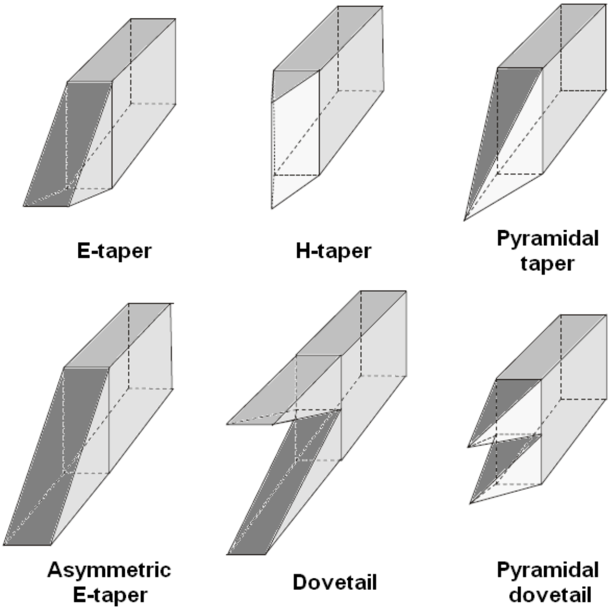

E-taper **H-taper** **Pyramidal taper**

Asymmetric E-taper **Dovetail** **Pyramidal dovetail**

Figure 4.3: Tapers geometries.

Because of the ease of the manufacturing process (see Section B.1), DRW antennas are cost-affordable. When using high permittivity materials, such as silicon or GaAs, they can be small size and lightweight. Waste parts of processed wafers can be used for manufacturing them, as long as they are low losses and have suitable thickness. Then, it is possible to get from the same wafer both the AEs and the DRW. Dielectric rods are a compact and mechanically strong alternative to conventional silicon lenses.

Different illumination strategies are possible to coupling field to a DRW. Two different alternatives are of interest for the research presented in this document: rectangular waveguides and AEs. First, is interesting because of its ease of implementation, which is convenient for concept validation. The second is when coupling the AE generated field to the DRW antenna for increasing the amount of terahertz power extracted from the high permittivity substrate. Coming up next, a study of both strategies is done in the following subsections (4.2.1 and 4.2.2, respectively).

4.2.1 DRW antenna fed by rectangular waveguide

Planar dielectric rod antennas were proposed for the mm- and submm wave range in [10,14,15]. Authors use standard rectangular waveguides for coupling the field into the DRW. This family of antennas has one matching taper for efficient coupling between metallic waveguide and dielectric slab. A second taper is made for radiating the power into the free space properly. Such antenna is sketched on Fig. 4.4a. Both ends of a HR silicon taper rod are tapered on the horizontal plane (XZ, E-plane). The taper length L_{TAPER} must be large enough for providing a good matching in the working band [11–13,16].

DRW radiation taper has no upper cut-off frequency, which gives the possibility to use in ultra-wideband applications. The prototype shown in Fig. 4.4b is only limited by the bandwidth of the WR-10 metal waveguide (75-110 GHz). A GaAs prototype working from 75 GHz to 1.1 THz is reported on [17]. Such bandwidth is achieved by using different waveguide standard for each sub band, from WR-10 to WR-1.

Fig. 4.4b sketches a DRW antenna. A 100 GHz prototype is designed, manufactured and characterized for evaluating both its performance and the quality of our simulation models. It has a maximum cross section (THK x W in Fig. 4.4a) of 0.5 x 1.0 mm^2. The taper length L_{TAPER} is chosen to be 8 mm, which according to the laboratory measurements provides a good-enough matching over the full WR-10 operation band.

A 2 mm long L_{DRW} section of DRW is added for gluing a low-density foam ring, which keeps the dielectric rod properly aligned into the metal

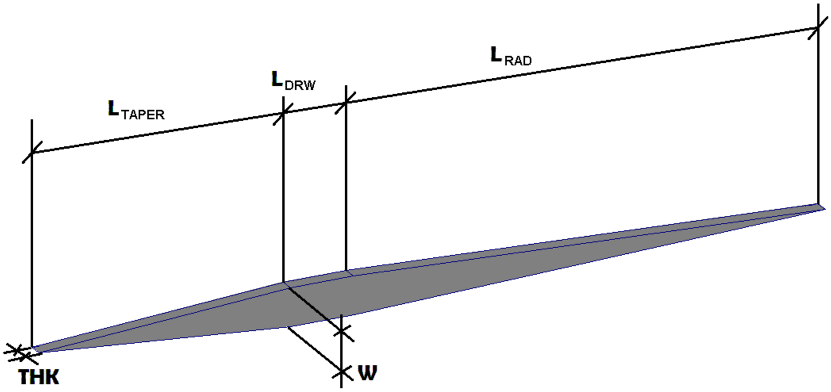

(a)

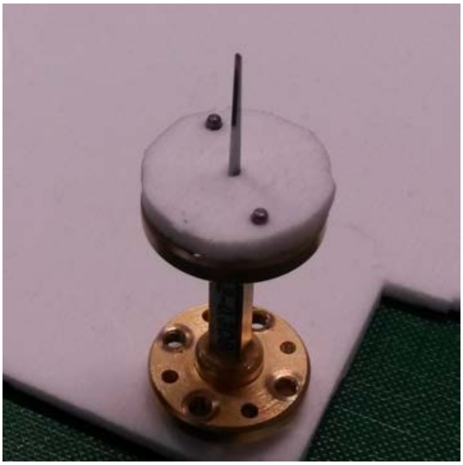

(b)

Figure 4.4: Assembled dielectric rod waveguide antenna. Sketch (a) and manufactured sample designed to work at 75-110 GHz (b). It is fed by a WR-10 rectangular waveguide

waveguide. A strip of teflon is used for avoiding a contact between metal and semiconductor (unseen in Fig. 4.4b due to the foam).

The antenna is properly fed when only the fundamental mode is excited. Suitability of metallic waveguide feeder is verified through full-wave simulations using HFSS [18] software. Fig. 4.5 shows E-field distribution both in the transition from the rectangular waveguide to the

DRW (Fig. 4.5a) and in the radiation taper (Fig. 4.5b). It is shown that the wave that comes from the metal waveguide is mostly guided through the DRW. Then the wave propagates in a single-mode regime along the DRW axis.

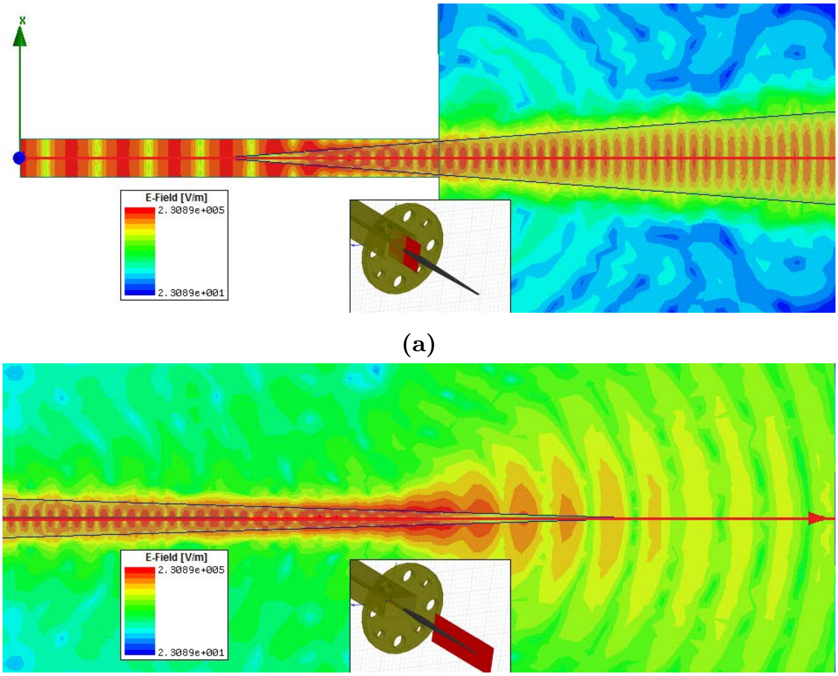

(a)

(b)

Figure 4.5: Example of simulated E-Field distribution [log(V/m)] on XZ plane (red area in 3D inset) in the waveguide DRW transition (a) and in the radiation tapering (b)

Fig. 4.5a shows how the waveguide field is efficiently coupled to the dielectric structure. A matching taper of length 8 mm can achieve a $|S_{11}| < -15$dB on the whole band (75-110 GHz), as confirmed by experimental evidence (Fig. 4.6).

The radiation taper length L_{RAD} is directly related to the antenna directivity [8,11,16]. A length of $L_{RAD} = 15$ mm is chosen, which leads to a measured gain of 16 dB after calibrating the set-up with a 20 dB Aerowave-7020 pyramidal horn. Fig. 4.7 shows the measured radia-

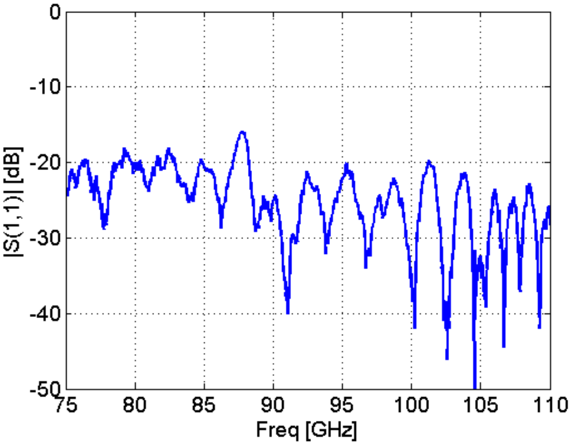

Figure 4.6: Measured S_{11} parameter for the DRW antenna of Fig. 4.4b.

tion pattern compared with a full-wave simulation results. A measured cross-polar discrimination (XPD) of 28 dB is achieved in the main lobe direction.

Figure 4.7: Simulated (dashed) and measured (solid) radiation patterns of the DRW antenna. Both E-plane ($\phi = 0°$, red) and H-plane ($\phi = 90°$, blue) are shown. Cross-polar cannot be seen since they are below -25 dB.

4.2.2 DRW antenna fed by AE

Fig. 4.8 shows the geometry of a DRW antenna fed by an AE terahertz source. The first is placed at the backside of the AE wafer. For convenience, the substrate is assumed to be infinite on XY plane in all of full-wave simulations. This is commonly a proper assumption, since in order to take advantage of the manufacturing resources, many experiments are built in the same substrate. It is also a realistic scenario in commercial designs where various electronics are embedded in the same package and, therefore, share a large semiconductor slab as a common substrate.

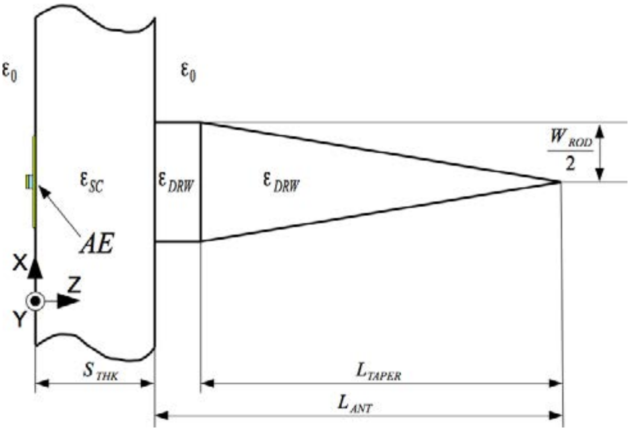

Figure 4.8: Sketch of the system: Dielectric antenna of length $L_{ANT} = L_{DRW} + L_{TAPER}$ attached to an infinite substrate layer S_{THK} thick.

An E-field X-axis direction is chosen for the fundamental mode inside the DRW. This will achieve an efficient illumination. An X-axis oriented linear-polarized log-periodic antenna is placed in order to avoid a 3 dB penalization. Both relative permittivities ε_{SC} and ε_{DRW} are the same if the same material substrate both for the wafer and for the manufactured DRW is used. This also avoids an extra penalization for reflections between two different mediums.

Several prototypes were assembled an characterized. Below, measurements are presented for two designs: first, is a proof-of-concept with an already available DRW antenna; second, with an optimized dielectric antenna for 200 GHz.

a) First DRW Antenna Prototype

For the first proof-of-concept manufactured, L_{TAPER} is chosen to be 8 mm and W_{ROD} 1.2 mm. In order to simplify the assembly, a dielectric rectangular waveguide is placed between the radiation taper and the wafer, being L_{DRW} 15 mm, so the total length of the DRW antenna is $L_{ANT} = 23$ mm. A low-loss semi-insulating GaAs wafer of 0.6 mm thickness is chosen for manufacturing the dielectric antenna structure.

A three-period *n-i-pn-i-p* photomixer [19] is attached to a log-periodic antenna (Fig. 1.4). It is manufactured using a InP wafer of 0.5 mm of thickness. The whole prototype is pigtailed for measurement convenience, as can be seen in Fig. 4.9. An RC filter protects the AE from electrostatic shocks.

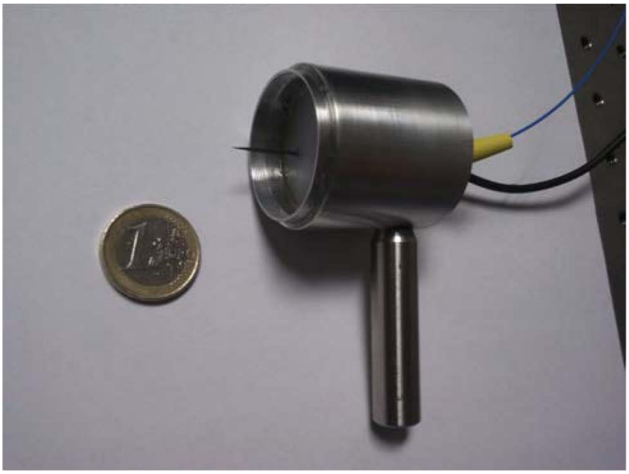

Figure 4.9: Proof-of-concept prototype. This is the first asembly of an AE with a DRW antenna.

A radiation pattern was measured at 137 GHz and compared with similar prototype with same type of AE but a 10 mm diameter silicon lens instead of a DRW antenna. As it can be deducted from Fig. 4.10, the power (normalized by the square of the photocurrent, $P_{THz}(\phi, \theta)/I_{DC}^2$

where P_{THz} is the THz measured power over the Golay cell aperture for a certain (ϕ, θ) direction and I_{DC} is the photomixer current) of DRW antenna is much lower than that of a lens. A slight tilt can be appreciated in the E-plane for the lens setup. This is due to a misalignment in the XY plane (along the X-axis) of the lens, which leads to place the focal point out of the AE center.

Figure 4.10: Comparison between measured power (in arbitrary units, logarithmic scale) achieved by the use of silicon lens, E-plane (red) and H-plane (black), and DRW antenna, E-plane (green) and H-plane (blue).

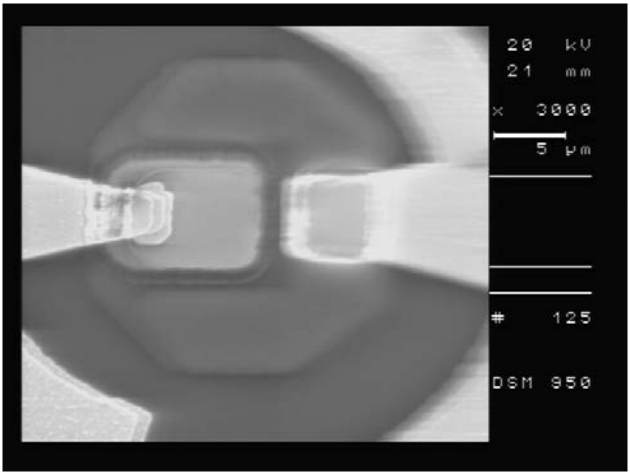

Figure 4.11: SEM image of the *n-i-pn-i-p* photomixer of the second.

b) Second DRW Antenna Prototype

A second prototype (Fig. 3.13a) is manufactured with an optimized design of DRW antenna (*DRW-AE-02*). After several rounds of simulations, L_{TAPER} is chosen to be 8 mm and W_{ROD} 0.5 mm. A low-loss high-resistivity silicon wafer of 0.5 mm thickness is used this time for manufacturing the dielectric antenna.

A three-period InGaAs *n-i-pn-i-p* photomixer (Fig. 4.11) with a log-periodic antenna is used. This is a device with a cross section of 8.5 x 5 μm^2. Its small size (42 μm^2. Typical devices are 10 x 10 μm^2) is for improving its performance at 1 THz [20] by reducing the effect of the RC roll-off. Because of its low band gap energy (0.75 eV) it is suitable for telecommunication lasers. Because of the assembly procedure (see Section 3.2) it is not possible to estimate the laser spot size over the diode. Nevertheless, a maximum optical power of 20 dBm in the FC/APC connector is tolerated for avoiding excessive heating.

Radiation pattern is measured in the spherical FF setup (see Section 3.3.1) and shown on Fig. 4.12. A Golay cell is used in a non-coherent scheme as a detector. An optical chopper and a locking amplifier are used for measuring at a chopping frequency of 8 Hz. Achieved dynamic range is only 12 dB. Measured photocurrent is around 150 nA, which is much

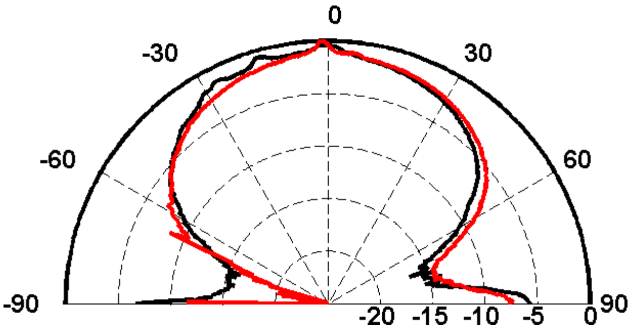

Figure 4.12: Measured radiation pattern at 150 GHz. Both E-plane (XZ plane, black) and H-plane (YZ plane, red) are shown.

lower than expected (it should be in the order of milliamps, according to other devices measurements). This explains the measurement poor dynamic range, since a low power level is achieved.

4.2.3 Alignment tolerances

According to our simulations, a tolerance of $\pm 100\,\mu$m must be achieved in the DRW antenna alignment step for the XY plane. Bigger errors would decrease the amount of THz power coupled to the fundamental mode of the rod.

4.2.4 Limitations

Fig. 4.13 shows the simulated E-field distribution in the *DRW-AE-02* design for 200 GHz (Fig. 4.13a) , 250 GHz (Fig. 4.13b), and 300 GHz (Fig. 4.13c).

Various modes propagate inside the DRW antenna when the width W_{ROD} is electrically large. Each mode is radiated at different active zones along the radiation taper, when they are no longer supported in the dielectric slab. This leads to a widely dispersed radiation zones (1 and 2 in Figs. 4.13b and Fig. 4.13c) through the rod axis. Due to the small wavelength this leads to a multilobe radiation pattern. When only single-lobe endfire radiation patterns are required for the specific application,

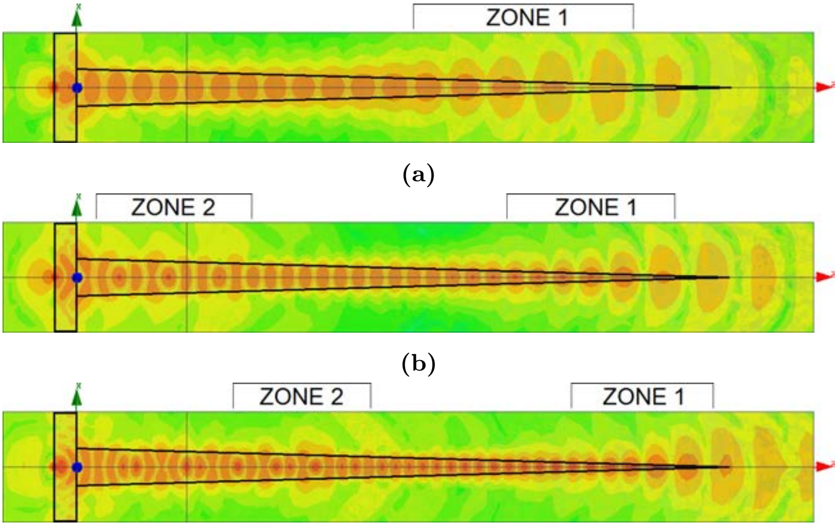

(a)

(b)

(c)

Figure 4.13: Simulated E-field [log(V/m)] distribution on XZ plane at 200 GHz (a), 250 GHz (b), and 300 GHz (c).

the bandwidth of the DRW antenna is limited by the existence of higher-order modes.

These higher-order modes cannot be described using the methodology introduced in Section 4.1. On such modes, a non-negligible E-field longitudinal component is present, so they cannot be defined as a quasi-TEM mode.

Moreover, for a frequency high enough, the union between the wafer and the DRW radiates part of the power, which leads to ripples in the radiation pattern. According to gained design experience, AE and DRW antenna must be coupled in the near field region, having substrates of thickness preferably smaller than the minimum $\lambda_{SC}/2$. This reduces the power radiated in the union and, therefore, increases the amount of power radiated by the DRW antenna.

4.3 Ultra-wideband DRW antenna

An AE creates spherical waves inside the DRW for an electrically large width W_{ROD}. Total internal refection along the radiation taper lead to higher-order modes, as shown in Figs. 4.13b and 4.13c. The integration of a planar lens inside the rod is proposed for rectifying the the generated wavefront of the spherical waves (Fig. 4.14).

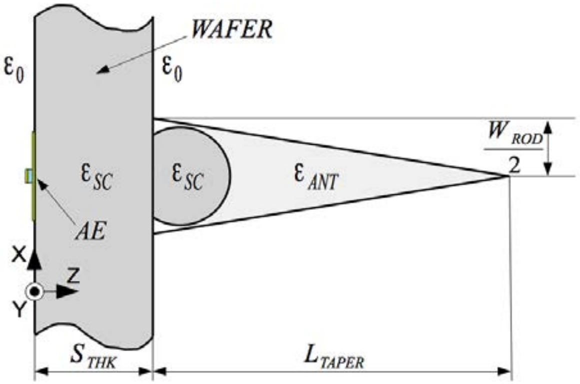

Figure 4.14: Sketch of dielectric rod waveguide antenna with an embedded planar lens.

The refracting interface of a lens introduces losses due to the media change. The generated power travels inside a medium of relative permittivity ε_{SC}. In order to minimize the reflection losses, the radiation taper permittivity ε_{ANT} must be an intermediate value between ε_{SC} and ε_0. The criteria for determining the optimum value of ε_{ANT} takes into account manufacturing capabilities, and losses due to reflections in medium changes.

Reflection losses at the lens-DRW interface are calculated according to the angle of incidence to the interface between media. Planar lenses must be E-plane oriented instead of H-plane, since it minimizes the reflections in the refractive interface. This is because the module of the power reflection coefficient of a p-oriented E-field $|\Gamma_p(\beta_{SC})|$ is less than or equal to an s-oriented E-field reflection coefficient $|\Gamma_s(\beta_{SC})|$ for $\beta_{SC} \in [0, \beta_c]$, being β_{SC} the angle of incidence of the medium change (see Figs. 4.15 and 4.18) and β_c the critical angle. Both $|\Gamma_p(\beta_{SC})|$ and

$|\Gamma_s(\beta_{SC})|$ can be calculated with the Fresnel coefficients

$$|\Gamma_s(\beta)| = \left| \frac{n_{SC} \cos \beta_{SC} - n_{ANT} \cos \beta_{ANT}}{n_{SC} \cos \beta_{SC} + n_{ANT} \cos \beta_{ANT}} \right|^2 \tag{4.7a}$$

$$|\Gamma_p(\beta)| = \left| \frac{n_{SC} \cos \beta_{ANT} - n_{ANT} \cos \beta_{SC}}{n_{SC} \cos \beta_{ANT} + n_{ANT} \cos \beta_{SC}} \right|^2 \tag{4.7b}$$

were $n_{SC} = \sqrt{\varepsilon_{SC}}$ and $n_{ANT} = \sqrt{\varepsilon_{ANT}}$ are the refractive indices of the two media for non-magnetic materials with $\mu_{SC} = \mu_{ANT} = 1$. The radiation taper avoids reflections between the intermediate medium and the air when L_{TAPER} is large enough by converging the effective permittivity $\varepsilon_{eff}(z)$ progressively to ε_0.

The lens dimensions must be chosen by taking into account the beamwidth of the AE. In order to prevent total internal reflection at the lens-DRW interface, the beam waist of the antenna must be smaller than the critical angle, β_c ($\beta_{SC} = [-\beta_c, \beta_c]$). Further, the lens must be large-enough to collect most of the THz power.

It can be shown [21] that an elliptic pattern is the exact solution to the problem, according to geometric optics (GO). Hyper-hemispheric lenses, however, are easier to produce and represent a good approximation to an elliptic interface.

The rest of this section is organized as follows. Firstly, the analytical expressions for the exact GO solution are shown. Secondly, the approximate design procedure is given. Both embedded lenses, the elliptic and the hyper-hemispherical one, are compared by full-wave simulations. Silicon ($\varepsilon_{SC} = 12$) is assumed for both AE wafer and lens. Both lens designs are integrated in a DRW antenna of dielectric constant $\varepsilon_{ANT} = \sqrt{\varepsilon_{SC}\varepsilon_0} \approx 3.5$. Rod length L_{TAPER} is 17 mm and width W_{ROD} is 2.2 mm. Thickness THK is assumed to be 300 μm for both wafer and DRW antenna.

Finally, a low frequency proof-of concept is characterized. The manufacturing of THz antennas is discussed in Section B.2.

4.3.1 Elliptical lenses

The embedded lens is a single refracting surface elliptical lens [21]. Its shape can be analytically determined as follows

$$X(\alpha) = \frac{(q-1)f\sin(\alpha)}{q\cos(\alpha)-1} \tag{4.8a}$$

$$Z(\alpha) = \frac{(q-1)f\cos(\alpha)}{q\cos(\alpha)-1} \tag{4.8b}$$

where $q = \sqrt{\frac{\varepsilon_{ANT}}{\varepsilon_{SC}}}$ takes into account the ration between relatives permittivities, $X(\alpha)$ and $Z(\alpha)$ describes the shape of the elliptic lens when giving values to the angle α; and $f = S_{THK} + Z(0)$ is determined for fitting the lens inside the DRW antenna and maximizing the collected THz power. The geometry is given in Fig. 4.15. The AE is placed in one of the ellipse focus. The distance between the AE and the refracting surface along the Z-axis is $f = 1.5$ mm.

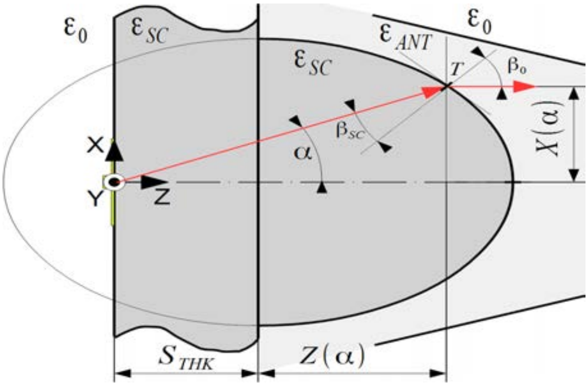

Figure 4.15: Geometry of an embedded elliptical planar lens.

Simulated E-field distributions in the XZ-plane are shown in the Fig. 4.16 at 150 GHz (Fig. 4.16a), 300 GHz (Fig. 4.16b), and 800 GHz (Fig. 4.16c). Elliptic lens transforms the generated spheric wave reducing excitation of higher order modes in the DRW, even for frequencies on which the rod is electrically large. The number and the importance of secondary radiation zones along the antenna is reduced, however, side lobes are still visible at higher frequencies. Secondary radiation zones are marked in the Fig. 4.16c.

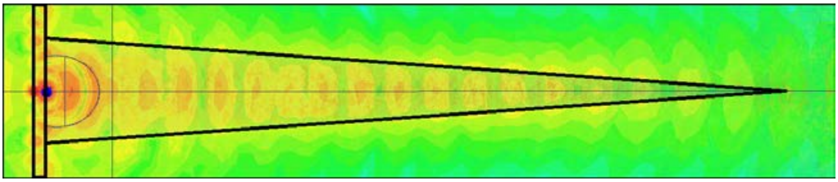

(a)

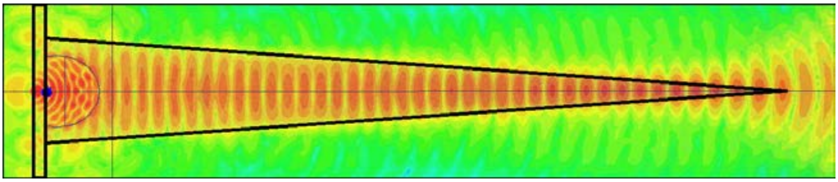

(b)

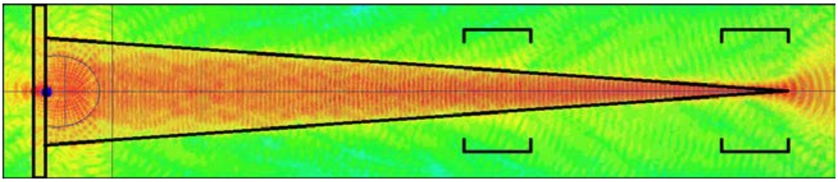

(c)

Figure 4.16: Simulated E-field distribution on XZ plane at 150 GHz (a), 300 GHz (b), and 800 GHz (c) for an elliptic lens as described in the text.

Calculated radiation patterns are given in Fig. 4.17.

4.3.2 Hyper-hemispherical approximation

Fig. 4.18 sketches the geometry of a hyper-hemispherical lens embedded in a DRW antenna. The planar lens is defined by a circumference of center C and radius R.

The lens hyperhemisphericity is $H = S_{THK} + \Delta Z$. Several series of simulations were defined in order to approximate the wavefront phase error inside the DRW radiation taper to the one obtained with an elliptic

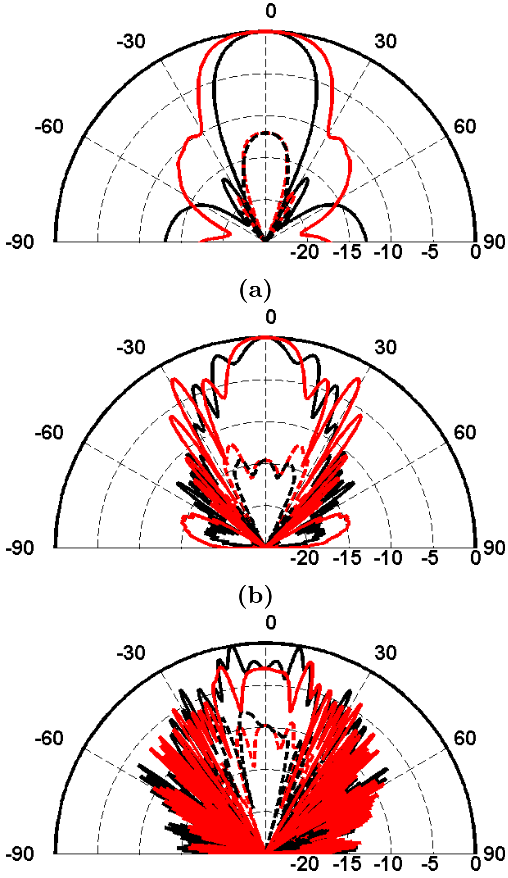

(c)

Figure 4.17: Simulated radiation pattern for the DRW antenna with an elliptic lens at 150 GHz (a), 300 GHz (b), and 800 GHz (c). Both E-plane (black) and H-plane (red) co-polar (solid) and cross-polar (dashed) components are shown.

lens. We appreciated that this phase error was reduced in at least a $1 : 10$ frequency range when forcing T_A ray (red) to be parallel to the Z-axis for $\beta_{SC} = 45°$. Assuming the same refractive index for the lens and the photomixer substrate, hyperhemisphericity is determined by the following expression:

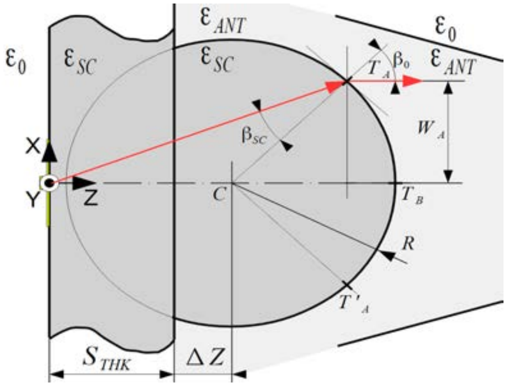

Figure 4.18: Geometry of an embedded hyper-hemispherical planar lens.

$$H = \left[\tan\left(\sin^{-1}\left(\frac{q}{\sqrt{2}}\right) + \frac{\pi}{4}\right) - 1\right]\frac{R}{\sqrt{2}} \tag{4.9}$$

where $q = \sqrt{\frac{\varepsilon_{ANT}}{\varepsilon_{SC}}}$ is the same as in eq. 4.8.

Fig. 4.19 shows the design chart according to eq. (4.9). Designs above the blue line are not feasible, since $\Delta Z > R$. Points below the red line are lenses with hyperhemispherities smaller than the AE substrate thickness S_{THK}, which are unachievable too. Insets sketch aspects of lens-based DRW antenna designs for different chart regions.

The relative permittivity ε_{ANT} is usually restricted to a few sets of values due to manufacturing issues. When ε_{ANT} is close to ε_{SC} (that is, $q \to 1$) the design of the lens becomes difficult, specially when wafer thickness S_{THK} is non negligible.

A lens of radius $R = 2$ mm is designed according to the explained procedure for $q = 0.54$. It is marked with a D in the design chart (Fig. 4.19), with $\Delta Z = 0.7$ mm, which leads to a hyperhemispherity $H = 1$ mm.

Fig. 4.20 shows the simulated E-field distribution inside the DRW antenna in the XZ plane. The lens generates a phase front similar to

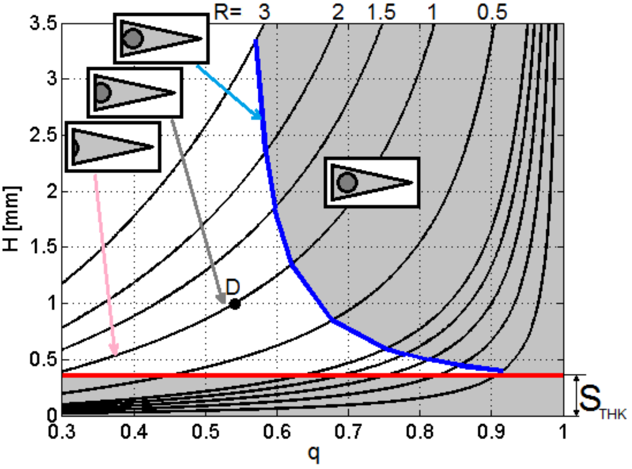

Figure 4.19: Design chart of embedded planar lenses. Limits of achievable hyperhemispherity values due to the wafer thickness (red) and the $\Delta Z > R$ constraint (blue) are shown. Insets show aspects of lens-based DRW antennas for different regions of the chart. When $\Delta Z = R$ (blue) the lens is tangent to the junction between wafer and DRW. Curves for $R = 3, 2, 1.5, 1, 0.5, 0.25, 0.20, 0.15, 0.10,$ and 0.05 mm are given (black). The design simulated in Section IV is highlighted (D).

the ones achieved with the elliptic lens at frequencies where $W_{ROD} >> \lambda_{DRW}$. Results are shown for 150 GHz (Fig. 4.20a), 300 GHz (Fig. 4.20b), and 800 GHz (Fig. 4.20c). The majority of the power is indeed radiated along the main lobe at theta=0°. However, there are still side lobes caused by higher order modes at 300 and 800 GHz (Fig. 4.20c).

The radiation pattern of the antenna is deteriorated. This can be solved by modifying the lens shape by scaling it and, if its possible, by reducing q in order to have a lens of bigger diameter and lesser hyperhemispherity H.

Radiation patterns are given in Fig. 4.21. Since not all the power is radiated at the DRW antenna tip, there are many secondary lobes of comparable levels to the main beam. Furthermore, there is a degradation in the XPD for the higher frequencies. The presence of nulls along the Z-axis is avoided, although there can be destructive interference in the radiation pattern for the endfire direction.

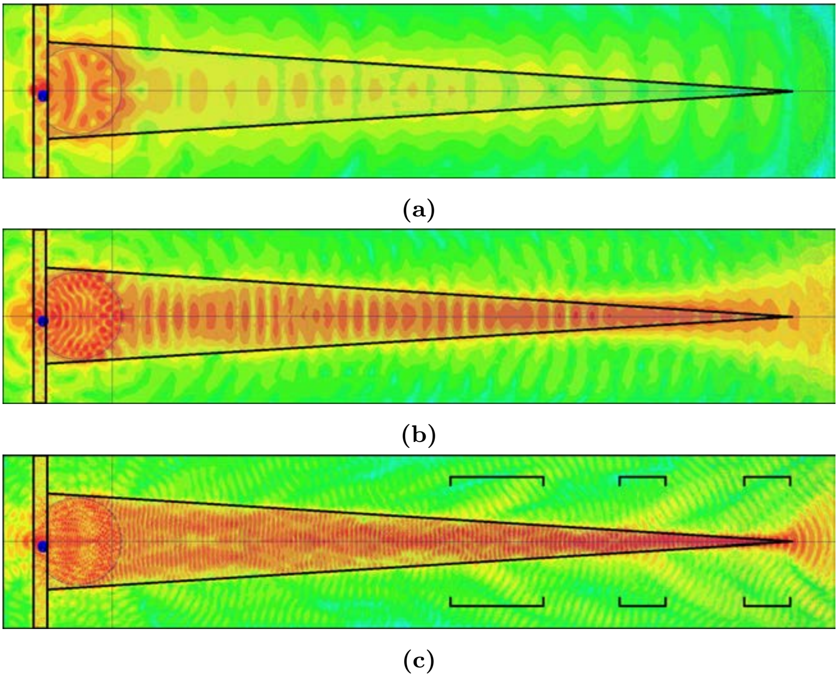

Figure 4.20: Simulated E-field distribution on XZ plane at 150 GHz (a), 300 GHz (b), and 800 GHz (c).

it can be appreciated that elliptic lens achieves a better radiation pattern when comparing Figs. 4.17 and 4.21. The exact GO solution leads to a lower SLL and less destructive interference at $\theta = 0°$.

When manufacturing capabilities allow embedding planar lenses of arbitrary shape patterns, an elliptic one should be chosen. If not, an hyperhemispheric design is preferable, in particular for inexpensive designs where the lens is accommodated in a drilled hole in a low-permittivity DRW antenna.

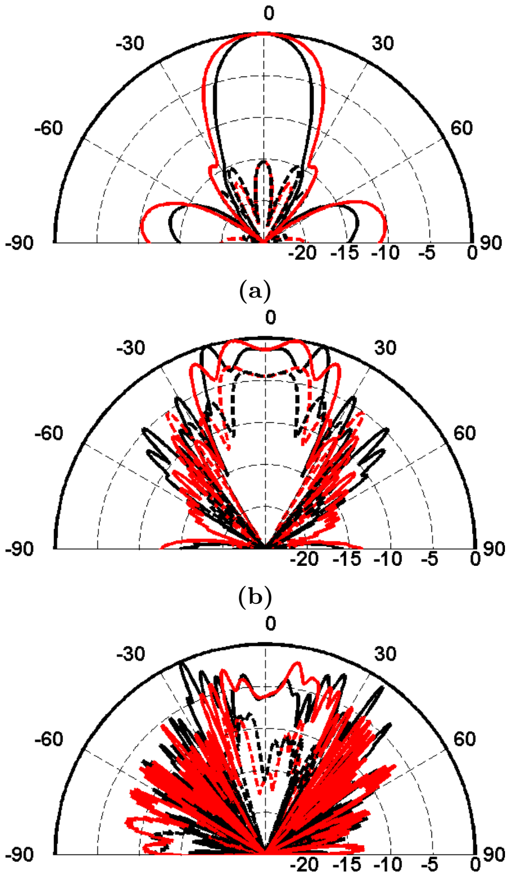

(a)

(b)

(c)

Figure 4.21: Simulated radiation pattern for the DRW antenna with a hyperhemispheric lens at 150 GHz (a), 300 GHz (b), and 800 GHz (c). Both E-plane (black) and H-plane (red) co-polar (solid) and cross-polar (dashed) components are shown.

4.3.3 Low frequency proof-of-concept

As seen in Fig. 4.13, for a high enough frequency a DRW antenna has many active zones. At some frequencies, there is destructive interference, which leads to a null in the Z-axis, as illustrated in Fig. 4.22 for an E-tapered polypropylene ($\varepsilon_r = 2.2$) DRW antenna designed to operate in the single-mode regimen in the 6-12 GHz band. Measurement was performed at 25 GHz. For exciting higher-order modes, a WR-28 rectangular waveguide is directly attached to the rod without matching taper (see Section 4.2.1). Rod dimensions are $L_{TAPER} = 190$mm and $W_{ROD} = 22$ mm (see Fig. 4.14). Polypropylene thickness is 5 mm.

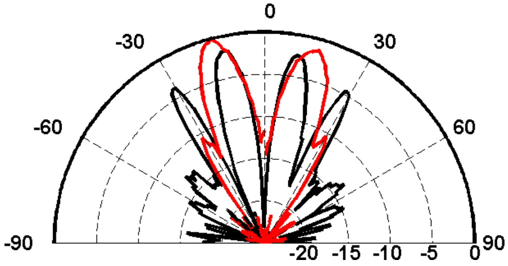

Figure 4.22: Measured radiation pattern. Higher-order modes are present in the rod. Interference of the modes results in a null in the Z-axis, besides an SLL of 4 dB. Both E-plane (red) and H-plane (black) co-polar (solid) and cross-polar (dashed) components are shown. θ is swept between ±90°. Radiation pattern is normalized, in dB.

The concept is validated by manufacturing and measuring the same DRW antenna with an embedded planar lens. A high-permittivity (AD-1000, $\varepsilon_r = 10$) substrate is used for manufacturing the elliptic lens of $q = 0.47$ and $f = 15$ mm. Same WR-28 rectangular waveguide is used for feeding the dielectric antenna.

According to our measurements, the working band, defined by the presence of a radiation maximum in the $\theta = 0°$ direction, is extended to beyond 30 GHz. Fig. 4.23 shows the measured radiation pattern at 25 GHz. A pronounced main lobe along $\theta = 0°$ is recorded, in contrast to the design without lens shown in Fig. 4.22.

For proving the suppression of radiation nulls in the Z-axis direction, the $|S_{12}|$ parameter is measured when antenna under test (AUT) is pointing towards a reference horn (TEST). The dielectric planar lens avoids the radiation null shown at 25 GHz both in Fig. 4.22 and Fig. 4.24. There is also a null at 32 GHz that is not present in the lens-based DRW antenna.

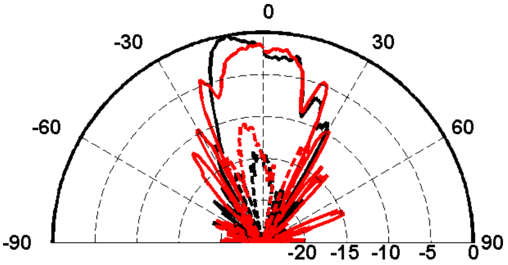

Figure 4.23: Measured radiation pattern. Both E-plane (red) and H-plane (black) co-polar (solid) and cross-polar (dashed) components are shown. θ is swept between ±90°. Radiation pattern is normalized, in dB.

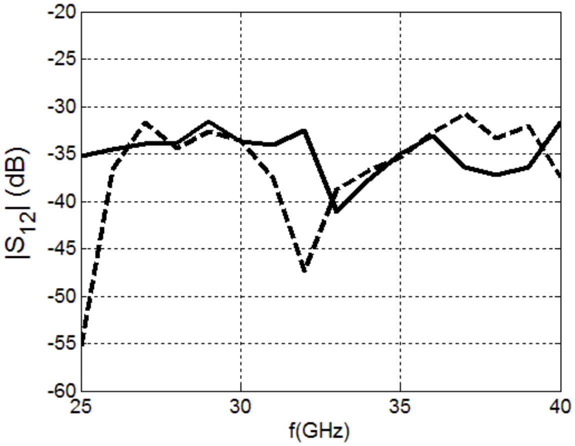

Figure 4.24: Measured $|S_{12}|$ parameter. A homogeneous DRW antenna presents radiation nulls along the Z-axis for some frequencies when operated outside of the single-mode frequency range (dashed). Same design with an embedded elliptic planar lens avoids such nulls up to 32 GHz (solid).

4.4 Conclusions

Table 4.1 summarizes the simulated efficiencies in the same conditions as the ones detailed in Section 1.4. As it can be seen, the use of DRW antennas can increase the efficiency of a plain AE, despite it does not match the silicon lens performance. When considering costs, they become appealing since rods can be between one and two orders of magnitude cheaper than silicon lenses due to its ease of manufacture.

	Substrate $\left(P^{tir}_{THz}\right)$	Back radiaton $\left(P^{rad}_{THz}\big\|_{Z<0}\right)$	η $\left(P^{rad}_{THz}\big\|_{Z>0}\right)$
Plain AE	50%	20.4%	29.6%
AE + lens ($R = 0.75$ mm)	17.1%	9.8%	73.1%
AE + lens ($R = 3$ mm)	5%	8.3%	86.7%
AE + DRW antenna	13.6%	9.1%	77.3%

Table 4.1: Comparative between efficiencies when using lenses, DRW antennas or nothing for avoiding scattering power into the semiconductor substrate.

A DRW antenna prototype has been assembled to a photomixing-based *n-i-pn-i-p* terahertz source. Radiation pattern measurements at 137 GHz and 150 GHz have been provided for two different samples.

A solution for increasing the band of DRW antennas has been proposed. Due to the extremely wideband achieved, the lens-based rods designs are electrically large in the E-plane (XZ-plane) for the higher frequencies, which it is undesirable in array configurations. They are compacts in the H-plane (YZ-plane), so they can be used for single-plane electronic steerable arrays. Two different lens design strategies have been proposed and compared via full-wave simulations. The concept has been validated through measurements in a low-frequency proof-of-concept.

4.5 References

[1] P. Pousi, D. Lioubtchenko, S. Dudorov, and A. V. Räisänen, "Dielectric rod waveguide travelling wave amplifier based on AlGaAs/GaAs heterostructure," in *38th European Microwave Conference (EuMC)*, 2008, pp. 1082–1085.

[2] J. Pousi, S. Dudorov, D. Lioubtchenko, and A. V. Räisänen, "Frequency selective coupler for W band based on power transfer in dielectric rod waveguides," in *Proceedings of the Fourth European Conference on Antennas and Propagation*, 2010.

[3] D. V. Lioubtchenko, P. Pousi, S. N. Dudorov, A. V. Räisänen, A. Deleniv, V. Drakinskiy, and S. Gevorgian, "Millimetre-wave phase shifter based on dielectric rod waveguide," in *38th European Microwave Conference (EuMC)*, 2008, pp. 1204–1206.

[4] C. Yeh and F. I. Shimabukuro, *The Essence of Dielectric Waveguides.* Springer, 2008.

[5] E. A. Marcatili, "Dielectric rectangular waveguide and directional coupler for integrated optics," *Bell System Technical Journal*, vol. 48, no. 7, pp. 2071–2102, 1969.

[6] J. Goell, "A circular-harmonic computer analysis of rectangular dielectric waveguides," *Bell System Technical Journal*, vol. 48, no. 7, pp. 2133–2160, 1969.

[7] D. Lioubtchenko, S. Tretyakov, and S. Dudorov, *Millimeter-Wave Waveguides.* Springer Science & Business Media, 2003, vol. 114.

[8] P. Pousi, "Active and passive dielectric rod waveguide components for millimetre wavelenghts," *Ph.D. dissertation, Department of Radio Science and Engineering, School of Science and Technology, Aalto University, Espoo, Finland*, 2010.

[9] A. Generalov, "Dielectric rod waveguide components at sub-THz frequencies," *Ph.D. dissertation, Department of Radio Science and Engineering, School of Electrical Engineering, Aalto University, Espoo, Finland*, 2015.

[10] J. Pousi, D. Lioubtchenko, S. Dudorov, J. Mallat, and A. Räisänen, “High permittivity dielectric rod waveguide antenna for 110-150 GHz,” in *First European Conference on Antennas and Propagation, 2006. EuCAP 2006.*, 2006, pp. 1–4.

[11] S. Kobayashi, R. Mittra, and R. Lampe, “Dielectric tapered rod antennas for millimeter-wave applications,” *IEEE Transactions on Antennas and Propagation*, vol. 30, pp. 54–58, 1982.

[12] S. Kobayashi, R. Mittra, and R. Lampe, “Dielectric rod antennas of rectangular cross section,” in *Antennas and Propagation Society International Symposium, 1980*, vol. 18, 1980, pp. 27–30.

[13] J. Weinzierl, C. Fluhrer, and H. Brand, “Dielectric waveguides at submillimeter wavelengths,” in *IEEE Sixth International Conference on Terahertz Electronics Proceedings, 1998. THz Ninety Eight. 1998*, 1998, pp. 166–169.

[14] D. V. Lioubtchenko, S. N. Dudorov, J. A. Mallat, and A. V. Räisänen, “Dielectric rod waveguide antenna for W band with good input match,” *IEEE Microwave and Wireless Components Letters*, vol. 15, no. 1, pp. 4–6, 2005.

[15] A. A. Generalov, J. A. Haimakainen, D. V. Lioubtchenko, and A. V. Räisänen, “Wide band mm- and sub-mm-wave dielectric rod waveguide antenna,” *IEEE Transactions on Terahertz Science and Technology*, vol. 4, no. 5, pp. 568–574, Sep. 2014.

[16] A. Rivera-Lavado, S. Preu, L. E. García-Muñoz, A. Generalov, J. Montero-de Paz, G. Dohler, D. Lioubtchenko, M. Mendez-Aller, F. Sedlmeir, M. Schneidereit *et al.*, “Dielectric rod waveguide antenna as THz emitter for photomixing devices,” *IEEE Transactions on Antennas and Propagation*, vol. 63, no. 3, pp. 882–890, 2015.

[17] A. Generalov, D. Lioubtchenko, and A. V. Raisanen, Räisänen, “Dielectric rod waveguide antenna at 75–1100 GHz,” in *2013 7th European Conference on Antennas and Propagation (EuCAP)*, 2013.

[18] Website of ANSYS HFSS, http://www.ansys.com/Products/Electronics/ANSYS-HFSS.

[19] G. Döhler, F. Renner, O. Klar, M. Eckardt, A. Schwanhäußer, S. Malzer, D. Driscoll, M. Hanson, A. Gossard, G. Loata *et al.*,

"THz-photomixer based on quasi-ballistic transport," *Semiconductor Science and Technology*, vol. 20, no. 7, p. S178, 2005.

[20] S. Preu, *Continuous-wave, Tunable THz n-i-pn-i-p Superlattice Photomixers and Applications.* MPL, 2009.

[21] T. A. Milligan, *Modern Antenna Design.* John Wiley & Sons, 2005.

CHAPTER 5

DIELECTRIC ROD WAVEGUIDE ANTENNA ARRAY

The potential advantages of dielectric rod waveguide antennas over dielectric lenses for photomixer-based terahertz sources have been highlighted in Chapter 4. Besides that, DRW antennas can achieve a major performance improvement when combining multiple sources.

The coherent combination of multiples AEs in a array configuration is a straightforward way to increase the generated power (see Section 2.3). When using a single large dielectric lens, the constructive interference between elements of the array no longer happens, specially when the off-axis distance of exterior elements is not electrically negligible. This effect is sketched in Fig. 5.1. In such scenario, multiple lobes appear in the radiation pattern [1] reducing the total power radiated along z-axis.

An array of DRW antennas can effectively combine the power of an arbitrary large number of mm- and sub-mm wave sources while keeping cost-affordable and lightweight. For proving this, a first prototype is done with rectangular waveguide feeder for reducing the complexity inherent to the use of an antenna emitter array (AEA). Therefore, the dimension of the used waveguide standard limits the density of elements.

An early 2x1 DRW antenna array prototype was presented and characterized on [2]. In the following subsection, a 4x4 elements array is fully

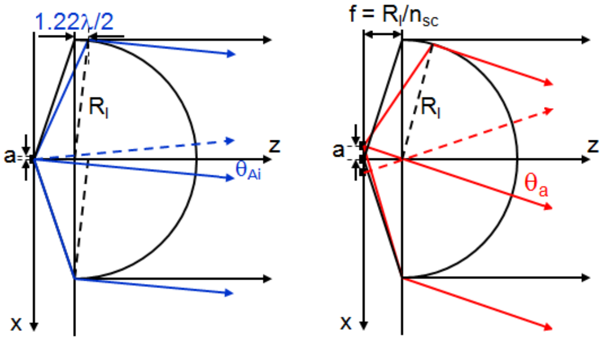

Figure 5.1: Illustration of the geometrical imaging and the diffraction aspects of an array with lens of radius R_l, and refractive index of n_{SC}. (a) A high density array (short distance , a, between elements) leads to a low-enough θ_{Ai}, so constructive interference is still possible. (b) Constructive interference hardly exists so instead of combining generated power along z-axis, many lobes are present in the radiation pattern.

studied for testing the scalability of this concept.

After the successful validation of the concept, an 1x4 antenna array is designed and simulated using an AEA in Section 5.2.

Besides the increase of radiated power, DRW antenna arrays can achieve a fully electronic beam steering when combined with proper phase shifters [3]. For proving this, scanning properties are studied. Furthermore, a novel carbon nanotube (CNT) based phase shifter is introduced. Provided measurements show how it is possible to modify the propagation constant by illuminating a thin layer deposited in one of the DRW walls with a tungsten lamp.

5.1 4x4 antenna array fed by rectangular waveguides

Fig. 5.2 sketches the layer-based power divider for feeding the DRW antennas. Upper layers are removed from the view for clarification purposes. First, a 1x4 E-plane power splitter divides equally the power into four layers. Then, four 1x4 H-plane horizontal power splitters feed the dielectric antennas. The rectangular waveguides are of standard WR-10 size. An uniform in-phase illumination distribution is achieved with this power divider. The array is designed to work at a central frequency of 100 GHz, since measurement facilities in Carlos III University of Madrid (see Section 3.3.1) and Aalto University (Subsection 3.3.2) can both operate at such frequency.

Alignment of the structure is extremely critical, especially when it is desirable to avoid the reflections between E-plane and H-plane power splitters. Because of that, a top and bottom layer with eight alignment pins and then screws are used.

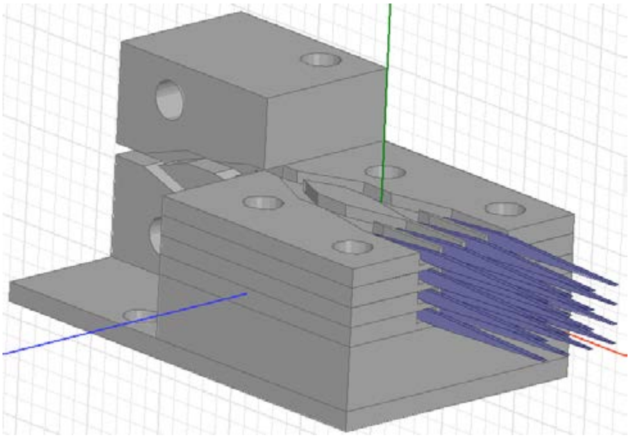

Figure 5.2: Sketch of the 4x4 DRW antennas array.

The feeder prototype is manufactured of brass and gold-plated. A vertical pitch between elements of 2 mm ($2\lambda_0/3$ at 100 GHz) is chosen for convenience. Horizontal pitch is 3 mm (λ_0). Other relevant dimensions are shown in Fig. 5.3a and Fig. 5.3b for the E-plane and H-plane 1x4 power dividers, respectively. Fig. 5.4 shows the assembled feeder prototype. The DRW antennas used are those described in Section 4.2.1.

Fig. 5.5 shows the manufactured prototype. DRW antennas are glued first on a slab made of the same low-density foam used for the single element prototype prensented in Section 4.2.1. For achieving the required alignment precision, foam can be previously milled via a computerized numerical control (CNC) device. Rods are properly placed in the gluing step by using a holder. Finally, the foam slab is aligned in the feeder.

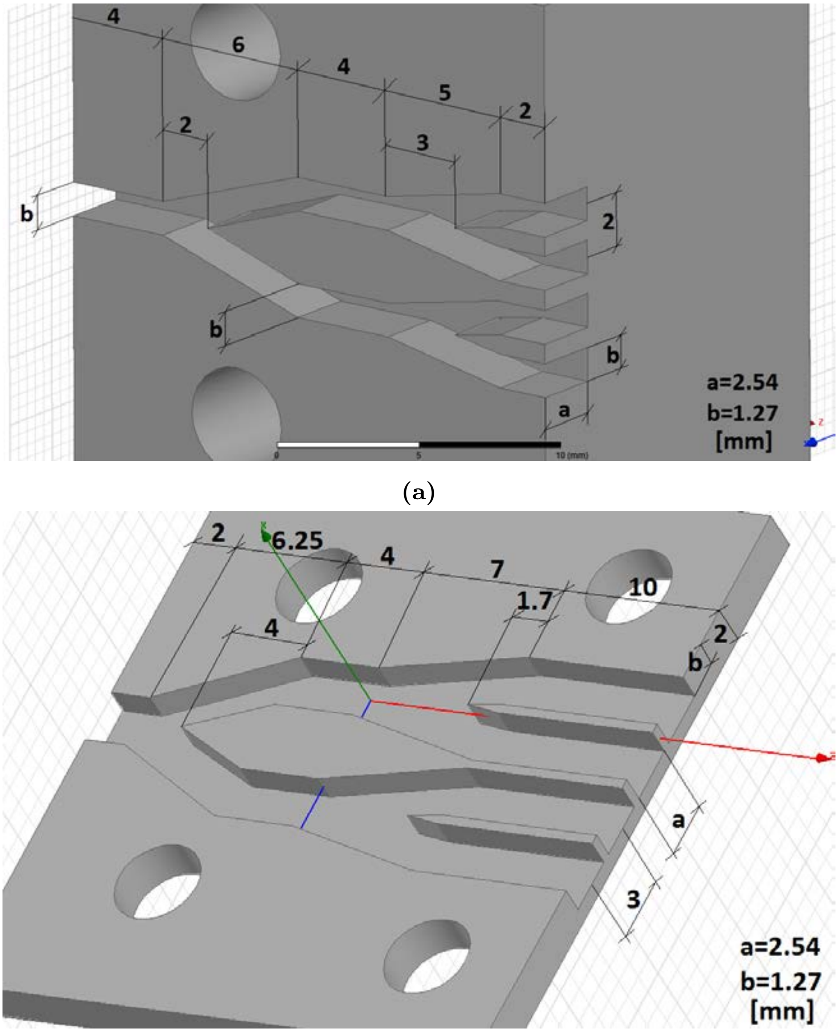

(a)

(b)

Figure 5.3: Geometric dimensions (in mm) for the vertical (a) and horizontal (b) 1x4 power dividers.

According to the simulations (see Subsection 4.2.1) a tolerance below 0.1 mm in he H-plane will lead to a successful coupling between rectangular waveguides and DRW antennas without any non-desired beam deviation. Tolerances in the E-plane are due to the DRW antennas width

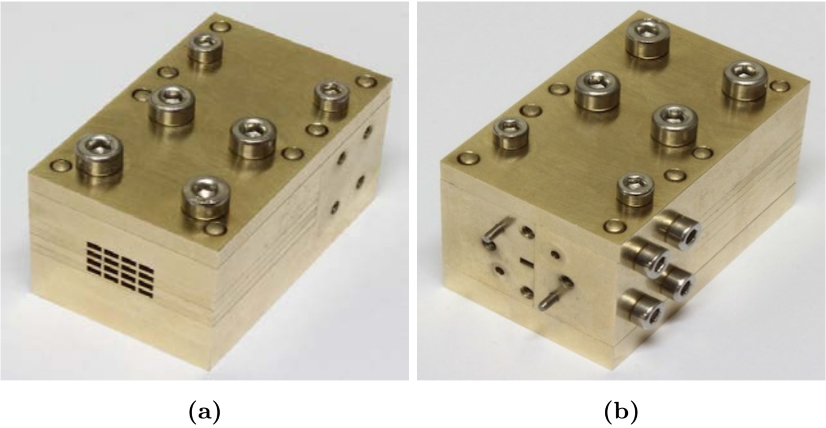

(a) (b)

Figure 5.4: Manufactured power divider before placing the DRW antennas.

(parameter W in Fig. 4.4a) and the milling error in the foam slab (it typically belittles the error in brass milling) which is around 0.02 mm.

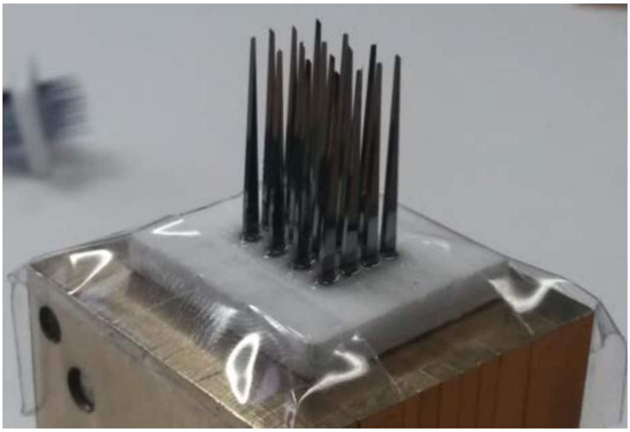

Figure 5.5: DRW antennas array fully assembled.

Coupling between elements is studied by simulating the structure. It is expected to be low, since most of the field is concentrated inside the rod [3, 4]. Following the results, the worst case is between two adjacent central elements. For a frequency of 100 GHz, coupling is below -30 dB. Fig. 5.6 shows the coupling over the frequency for adjacent elements, for both E-plane and H-plane. It is obtained by simulating the array using a waveguide port per rod instead of the power divider, and then, calculating the S parameter matrix.

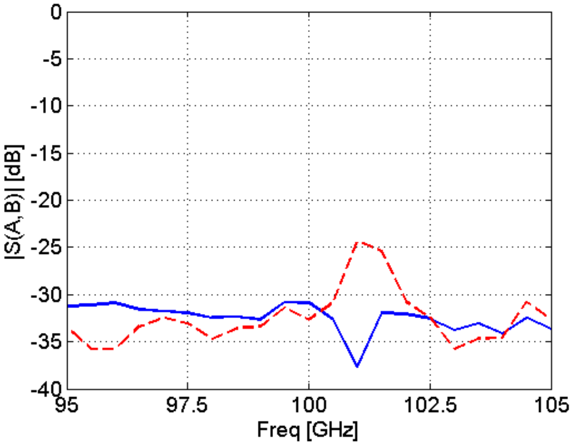

Figure 5.6: Coupling between E-plane (red, dashed) and H-plane (blue, solid) adjacent DRW antennas (worst case, central elements).

Performance of the WR-10 feeder is evaluated via a full-wave simulation of the field distribution inside the waveguides. Obtained E-field amplitude is shown in Fig. 5.7. Since this cannot be experimentally validated, return loss is both calculated from simulations and measured. Comparisons between obtained S_{11} parameters is displayed in Fig. 5.8. It is undeniable that the measurement results agrees very well with the simulation result at the frequency of 100 GHz. As concluded in Section 4.2.1, the bandwidth is restricted by the feeding network; and it is, clearly, narrower than the WR-10 standard operational band.

The radiation pattern is obtained in the setup described in Section 3.3.2. A view of the dispositions of the probe and the AUT is shown in Fig. 5.9. Distance between both antennas is 219.5 mm for ensuring a FF measurement conditions. Both measured and simulated radiation patterns are in a good agreement (Fig. 5.10). By calibrating with the same reference horn as in Section 4.2.1, a total gain of 23.5 dB is calculated. Fig. 5.11 shows the 2D radiation pattern (normalized, in dB).

For this particular configuration, according to the array factor, ad-

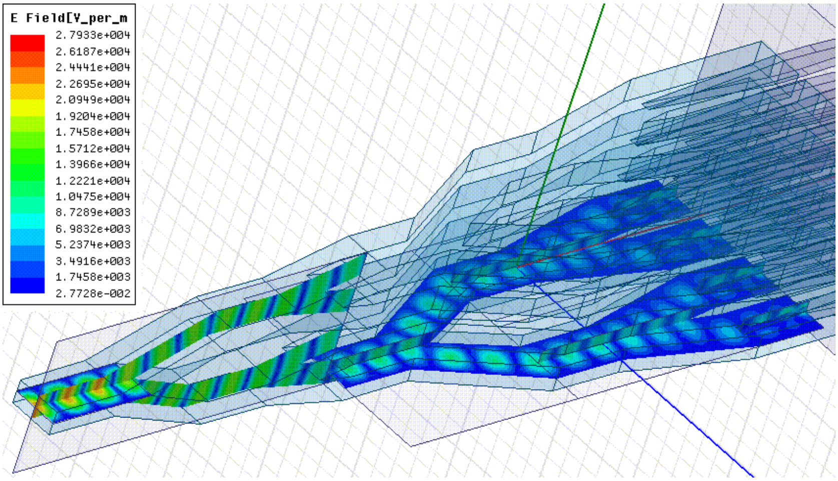

Figure 5.7: Simulated field distribution inside the power divider at 100 GHz.

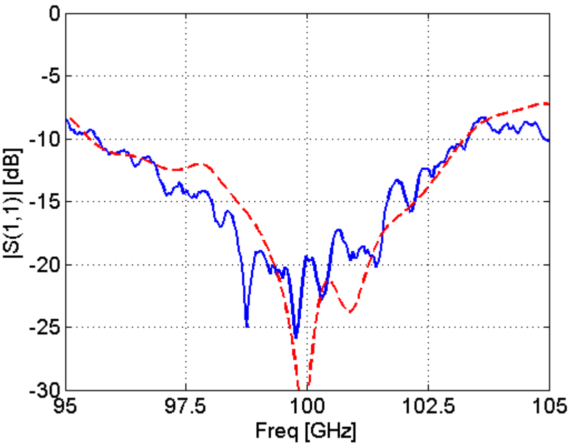

Figure 5.8: Simulated (red, dashed) and measured (blue, solid) S_{11} parameter of the fully assembled prototype.

ditional major lobes should appear at $\theta = \pm 90°$ in the H-plane. They are not present due to the single element radiation pattern, which has a zero at $\theta = \pm 90°$ (Fig. 4.7).

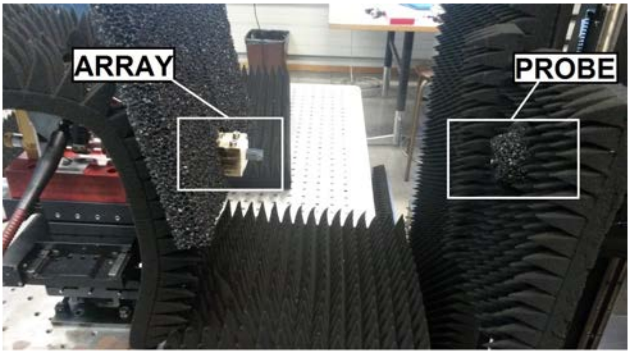

Figure 5.9: Measurement setup. A 2D planar scanner is used to measure the radiation pattern around the main beam.

Figure 5.10: Simulated (dashed) and measured (solid) radiation patterns of the DRW antenna array at 100 GHz. Both E-plane ($\phi = 0°$, red) and H-plane ($\phi = 90°$, blue) are shown. Cross-polar component (H-plane black, and E-plane green) is also displayed.

A XPD of 26 dB is obtained at 100 GHz. Although the simulated cross-polar component is still visible on Fig. 5.10 measured one is not because of the chosen amplitude range for clarification purposes. An explanation of why simulation gives smaller XPD levels than measurement results has not yet been found. This is not common, since there is always tolerances and misalignments that worsen the performance parameters, such as the XPD.

Simulated radiation pattern are obtained for different progressive phase values β between 0° and 90°. Scanning in both E-plane (Fig.

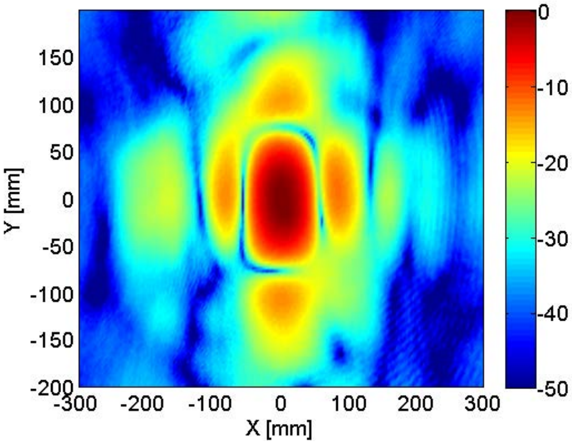

Figure 5.11: Normalized 2D E-field scan.

5.12a) and H-plane (Fig. 5.12b) is shown. As it can be expected, a great scanning angle leads to side lobes, which is non-desirable for scanning purposes. A SLL of 10 dB is obtained for a progressive phase of 90°. This limits the scanning angle to 39° for the E-plane and 56° for the H-plane, which is consistent with the expectations taking into account the spacing between elements in both perpendicular planes.

5.2 1x4 antenna array fed by an AEA

An 1x4 E-plane array of log-periodic photoconductive AEs prototype is designed and manufactured (Appendix A, Section A.3). AEs have a minimum working frequency of 100 GHz. Four DRW antennas are designed optimized for a frequency of 150 GHz. They work from 100 GHz to 200 GHz. Its dimensions are (see Fig. 4.8) $L_{TAPER} = 8$ mm, $L_{DRW=0}$ mm, $W_{ROD} = 0.5$ mm, and $S_{THK} = 0.5$ mm, E-plane tapered. A pitch of 1 mm between elements was chosen both for manufacturing considerations (experiments in the wafer must be fit in cells of 2x4 mm^2) and array factor properties: distance between elements is $\lambda/2$, which is suitable for broadside scanning arrays [5] at the optimum frequency. Since it is possible to get more dense arrays when using AEs instead of rectangular waveguides, better scanning properties can be expected from this configuration.

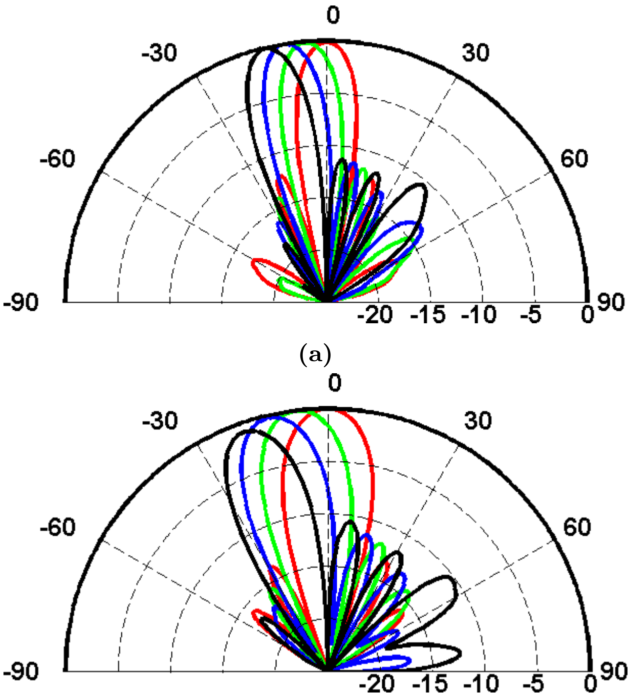

(a)

(b)

Figure 5.12: Radiation patterns when scanning in the E-plane (a) and the H-plane (b). Only E-plane (a) or H-plane (b) co-polar component is shown for progressive phase shift β of 0° (red), 30° (green), 60° (blue), and 90° (black).

A 3D view of the array design is shown in Fig. 5.13. Field distribution in the H-plane (XY plane, Fig. 5.14a) and E-plane (YZ plane, Fig. 5.14b) are displayed for a frequency of 150 GHz. The fundamental mode is clearly predominant inside each DRW antenna, which leads to a maximum radiation along the Z-axis.

As it can be deducted from the array configuration, the radiation pattern is more directive in the E-plane than in the H-plane (Fig. 5.15). The broadside directivity is 12.62 dB. A simulated XPD of 10.78 dB is obtained.

Fig. 5.16 shows the E-plane radiation patterns when scanning. When

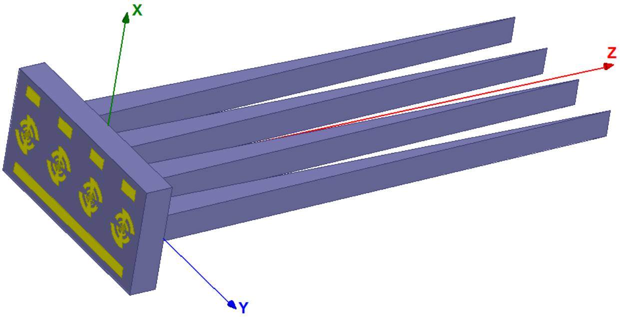

Figure 5.13: 1x4 DRW antenna array fed by four log-periodic AEs.

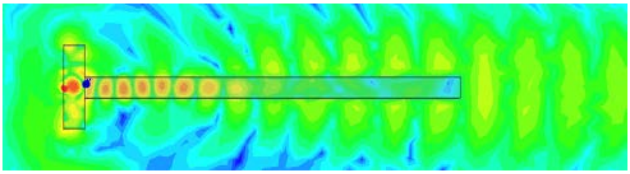

(a)

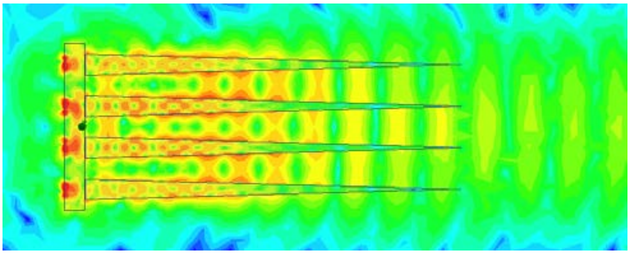

(b)

Figure 5.14: Field distribution in the H-plane (a) and E-plane (b) of the 1x4 DRW antenna prototype for a frequency of 150 GHz.

a maximum SLL of 10 dB is allowed, a scanning interval of ±24° (that is, a scanning angle of 48°) is obtained with a progressive phase shift of ±90°.

In the following section, a novel optically-controlled phase shifter for DRW technology is introduced.

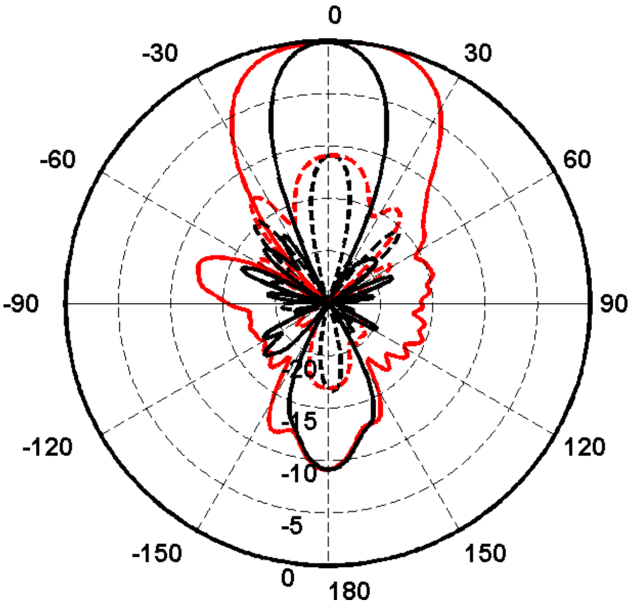

Figure 5.15: Measured radiation patterns of the 1x4 DRW antenna array at 150 GHz. Both E-plane ($\phi = 90°$, black) and H-plane ($\phi = 0°$, red) co-polar components (solid) are shown. Cross-polar (dashed) components are also displayed.

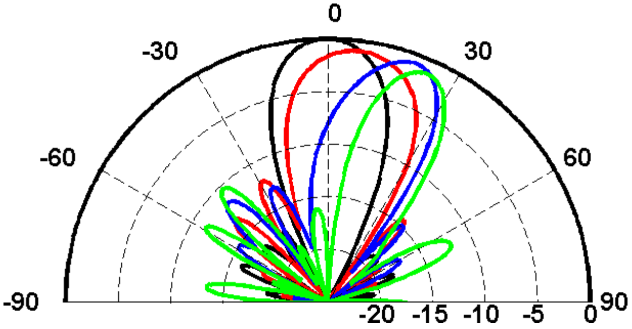

Figure 5.16: DRW antenna array scanning on the E-plane. A progressive phase shift β of 0° (black), 30° (red), 60° (blue), and 90° (green) is shown.

5.3 CNTs-based phase shifter

A phase shifter is a necessary component for electronically steerable arrays. In this section, the use of CNTs for DRW-based phase shifter is studied. Other technologies, such as microelectromechanical systems (MEMS)-based ones, have been already proposed [6]. Fig. 5.17 sketches a DRW (cyan) with a thin layer of CNTs (grey). It is matched to two WR-10 rectangular waveguides (red). A power-tunable optical source is used for illuminating the nanotubes layer (yellow).

CNTs were syntetized by aerosol chemical vapor deposition (CVD) method [7, 8]. Layers of CNTs of different optical transparency (measured at 550 nm) are then generated in a nitrocellulose filter. Deposition of nanotubes in the rod is done in a straightforward manner by simply pressing the nitrocellulose against the DRW wall, which makes this technology a cost-affordable alternative to others phase shifters for sub-millimeter and millimeter waves.

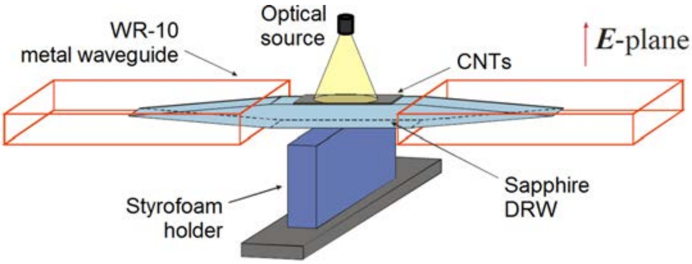

Figure 5.17: Schetch of a CNT-based phase shifter.

Since the DRW is an open transmission line (see Section 4.1), it is possible to modify the propagation constant by modifying the conditions in the waveguide walls, as authors do for their MEMS-based phase shifter.

During this thesis, experimental work was carried out for validating the use of thin CNT layers in optically controlled phase shifters. In this section, the most relevant results are shown. First, a sapphire rod is characterized. Then, it is loaded with a thin layer of CNT and measured with different illumination conditions.

- Unloaded DRW

A clean monocrystaline sapphire DRW with a cross section dimension of 1x0.5 mm^2 was characterized in the 75-100 GHz bandwidth by using an HP8530 VNA with two W85104A head extensions (see Section 3.4). The matching taper is 6 mm length, which ensures a good matching in the whole band (Fig. 5.18a). Fig. 5.18 shows that modulus of S parameters remains unchanged when modifying illumination conditions, which ensures that the substrate is not reacting to the light. Both a dark condition (red, solid) and an light intensity of 2.52 mW/mm^2 (blue, dashed) were created by using a tungsten lamp. Optical density of power was determined with a Sper Scientific 80011 Laser Power Meter.

- DRW with CNTs

Next, a layer of 60 % optical transparency was deposited on top of the DRW. The transmission parameter S_{21} is measured with different illumination conditions: for an optical power of ($P_0 = 0\,\text{mW/mm}^2$), of ($P_1 = 0.63\,\text{mW/mm}^2$) and ($P_o = 1.26\,\text{mW/mm}^2$). Fig. 5.19 shows the measured S_{21} parameter, both amplitude 5.19a and phase 5.19b.

For showing the achieved repetition in the experimental measurements, two samples of P_0 and three of P_1 were taken alternatively. Measurements are normalized with respect one of the P_0 samples. As it can be seen, there is no noticeable change on the amplitude of S_{21}. The phase is clearly dependent on the incident density of optical power. A maximum phase shift of 33 degree was achieved with a density of power of $1.26\,\text{mW/mm}^2$. With higher power optical sources, even wider phase shift ranges seems feasible.

At this point, the mechanism of this effect is not fully understood. With the results here presented it is not possible to determine whether there is optical interaction between light and nanotubes or there is heating due to light absorption in the CNT layer [9]. It seem that changes in the CNT layer conductivity are negligible, since S_{21} amplitude is almost independent of the optical power.

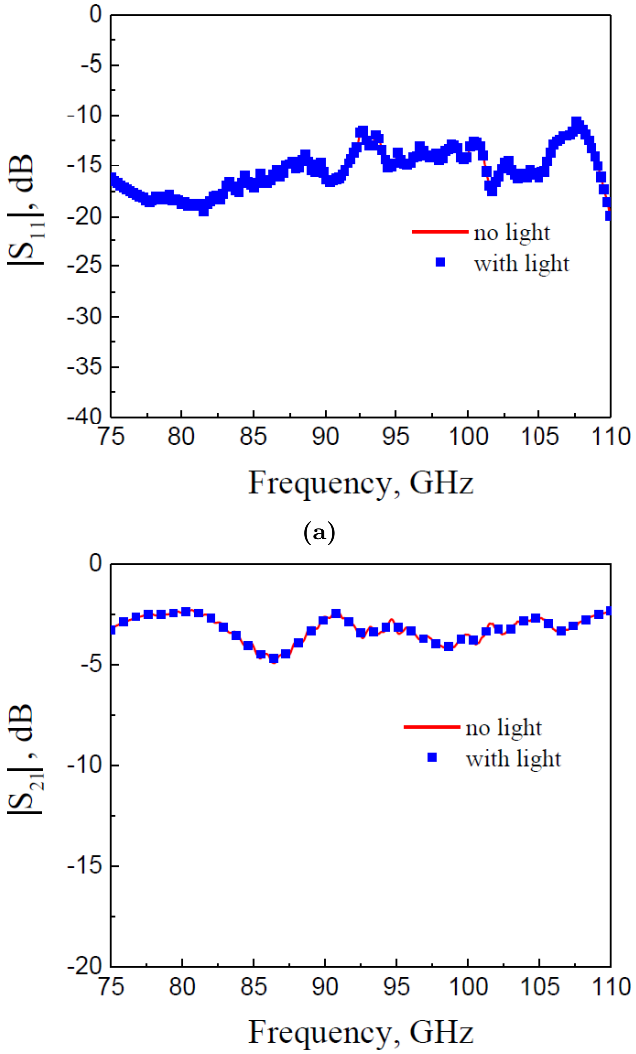

(a)

(b)

Figure 5.18: Measured S parameters (amplitude in dB) of an unloaded sapphire DRW without and with 2.52 mW/mm^2 light intensity illumination.

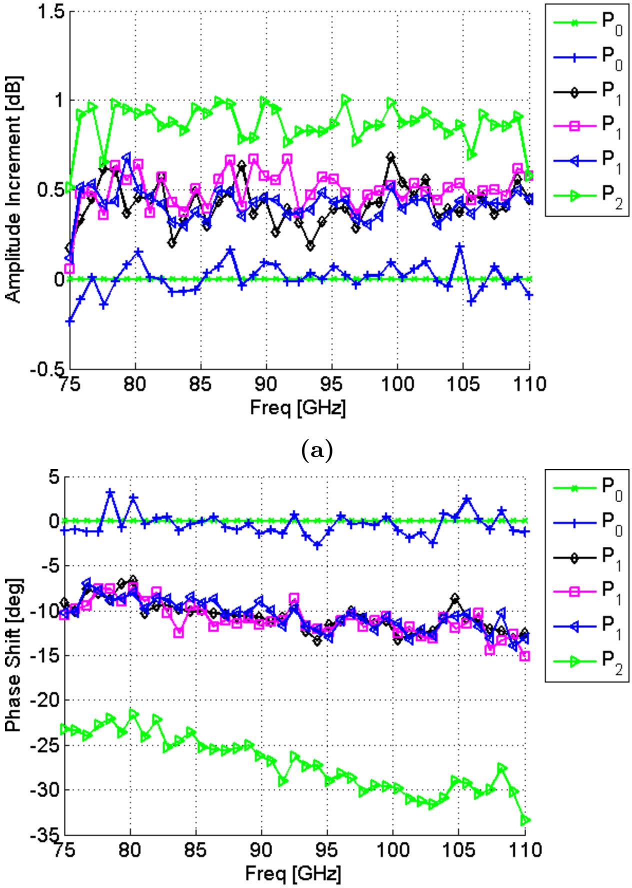

(a)

(b)

Figure 5.19: Amplitude (a) and phase (b) of the measured S_{21} parameter for three different light intensities: $P_0 = 0\,\mathrm{mW/mm^2}$, $P_1 = 0.63\,\mathrm{mW/mm^2}$ and $P_o = 1.26\,\mathrm{mW/mm^2}$.

5.4 Conclusions

In this chapter, the feasibility of using DRW antennas in arrays has been evaluated. To the best of our knowledge, only a 1x2 array has been reported [2]. A larger array of 4x4 elements was manufactured and fully characterized, which raised appealing characteristics such as low mutual coupling between elements, and a good XPD. It allows a more denser array of sources than it could be achieved with dielectric lenses.

The array was tested using a 4x4 WR-10 rectangular waveguide feeder. Full simulations were done for showing the concept feasibility when using arrays of AEs as the power source.

Finally, a novel phase shifter has been investigated. It is made by depositing a thin layer of CNT in one of the DRW walls. Despite further experimental work is needed in order to understand the observed phenomenon, a phase shift of 30 degree was obtained when illuminating the CNT layer with a tungsten lamp.

5.5 References

[1] A. Rivera-Lavado, L. E. García-Muñoz, G. Dohler, S. Malzer, S. Preu, S. Bauerschmidt, J. Montero-de Paz, E. Ugarte-Muñoz, B. Andrés-García, V. Izquierdo-Bermúdez *et al.*, "Arrays and new antenna topologies for increasing THz power generation using photomixers," *Journal of Infrared, Millimeter, and Terahertz Waves*, vol. 34, no. 2, pp. 97–108, 2013.

[2] J. P. Pousi, D. V. Lioubtchenko, S. N. Dudorov, and A. V. Räisänen, "High permittivity dielectric rod waveguide as an antenna array element for millimeter waves," *IEEE Transactions on Antennas and Propagation*, vol. 58, no. 3, pp. 714–719, 2010.

[3] D. V. Lioubtchenko, P. Pousi, S. N. Dudorov, A. V. Räisänen, A. Deleniv, V. Drakinskiy, and S. Gevorgian, "Millimetre-wave phase shifter based on dielectric rod waveguide," in *38th European Microwave Conference (EuMC)*, 2008, pp. 1204–1206.

[4] D. Lioubtchenko, S. Dudorov, J. Mallat, J. Tuovinen, and A. V. Räisänen, "Low-loss sapphire waveguides for 75-110 GHz frequency range," *IEEE Microwave and Wireless Components Letters*, vol. 11, no. 6, pp. 252–254, 2001.

[5] C. A. Balanis, *Antenna Theory: Analysis and Design.* John Wiley & Sons, 2005.

[6] D. Chicherin, M. Sterner, J. Oberhammer, S. Dudorov, D. Lioubtchenko, A. J. Niskanen, V. Ovchinnikov, and A. V. Räisänen, "Mems based high-impedance surface for millimetre wave dielectric rod waveguide phase shifter," in *European Microwave Conference (EuMC)*, 2010, pp. 950–953.

[7] A. K. Mishra, *Carbon Nanotubes: Synthesis and Properties.* Nova Publishers, 2013.

[8] M. Kumar and Y. Ando, "Chemical vapor deposition of carbon nanotubes: a review on growth mechanism and mass production," *Journal of Nanoscience and Nanotechnology*, vol. 10, no. 6, pp. 3739–3758, 2010.

[9] I. Nefedov and D. Lioubtchenko, private communications.

CHAPTER 6

DRW ANTENNA APPLICATIONS

According to the results shown in Chapter 4, silicons lenses offer better performance than DRW in terms of THz power radiated into the air. Applications where costs represent mayor highlights could justify the use of DRW instead of lenses. They can be used in arrays of CW terahertz sources for achieving high power, as discussed in Chapter 5.

There are others potential niches for DRW antennas, such as those where power must be coupled into a specific structure instead of being radiated to the free space. In this chapter, the use of DRW antennas as efficient near-field couplers for whispering gallery mode resonators (WGMRs) is proposed in THz up-conversion receivers. This family of receivers can potentially achieve the maximum sensitivity, which it is determined by the detection of a single THz photon. This systems are known as photon-counting receivers.

A WGMR is a dielectric resonator on which many successive total internal reflection (TIR) occur. Fig. 6.1 shows a circular WGMR, on which the angle of incidence in the interface of an inner ray (black) is always the same. n_1 is the refractive index of the dielectric. It is assumed to be surrounded by vacuum ($n_0 = 1$). By assuming that amplitude decreases exponentially according to a loss coefficient α, the ray amplitude can be calculated as a function of distance traveled inside the resonator x

$$I(x) = I_0 e^{-\alpha x} \tag{6.1}$$

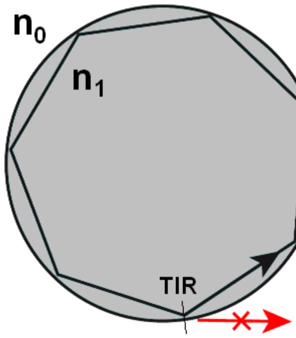

Figure 6.1: Sketch of a WGMR. Since $n_1 > n_0$ TIR can occur. The plotted ray (black) has multiple TIR and fulfill the phase matching conditions, so it becomes a resonance.

The loss coefficient takes into account many different effects, such as loses and scattering in the dielectric and radiative emission, which occurs when the resonator radius is comparable to the wavelength [1, 2]. The quality factor Q can be calculated from the loss coefficient

$$Q = \frac{2\pi n}{\lambda_0 \alpha} \tag{6.2}$$

In the terahertz frequencies, the material losses dominates, but quality factors up to 10^4 are feasible [3, 4]. In the optical domain, values of Q higher than 10^{10} has been demonstrated [5].

Fig. 6.1 shows a ray (black) that after many successive inner reflections, it completes a round with a total length

$$L = m\lambda_1 \tag{6.3}$$

where m is a integer number greater than zero and λ_1 is the wavelength inside the resonator. In this case, the system is in resonance for the specific frequency $f = c/\lambda_1$. By giving values to m from 1 to infinite, all resonance frequencies f_m can be obtained. The distance between two consecutive resonances is known as the free spectral range (FSR), which is the inverse of the roundtrip time $T = 1/FSR = n_1 L/c_0$, where c_0 is the speed of light in free space. The quality factor is inversely proportional to the linewidth, or full width at half maximum (FWHM). Fig. 6.2 shows the normalized reflection intensity for an incident signal that creates a whispering gallery mode (WGM) inside the resonator as a function of the total phase of a round trip, which takes into account both the optical length and the coupling phase shift. The system is assumed to be critically coupled, that is, the losses are compensated by the coupled signal, which keeps constant the power inside the resonator.

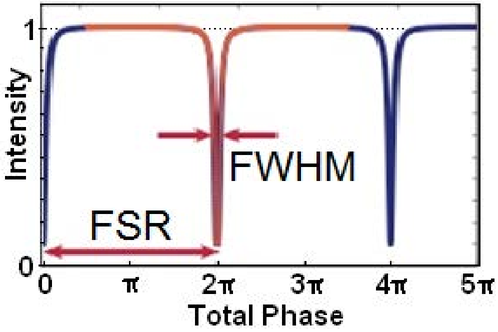

Figure 6.2: Reflected intensity as a function of the total phase of a round trip $\theta = 2\pi n_1 L$ inside the WGMR.

6.1 THz photon counting receiver

As said above, a photon counting receiver is a device that is able to detect a single photon of a specific frequency inside the working band. The sensitivity of the detector is determined by a quantum limit in opposition to conventional receivers, which are limited by thermal noise. In a photon-counting receiver [6]

$$k_B T \cdot B \cdot \tau < h\omega \cdot \eta \tag{6.4}$$

where $k_B T \cdot B$ is the *noise equivalent power (NEP)* and $h\omega$ the photon energy. τ is the detector's response time, B is its bandwidth, and η is its quantum efficiency. In the mm and sub-mm waves receivers must be cooled down for keeping the photon energy exceeding the *NEP* [7–10].

It is possible to reduce the thermal noise level by forcing $B\tau << 1$ [11,12], which relax the cooling requirements. In [12], Khan et al. achieve a *NEP* of 78 fW/$\sqrt{\text{Hz}}$ with a τ of 1 ns and a power conversion efficiency of 0.12%. A simplified sketch of their experiment is shown in Fig. 6.3 It is achieved by up-converting the signal to the optical domain in a GaAs crystal, which haves a high second-order nonlinear susceptibility $\chi^{(2)}$ [13]. Then, the signal is coupled into an optical fiber (black) and detected with a Geiger-mode avalanche photodiode (APD).

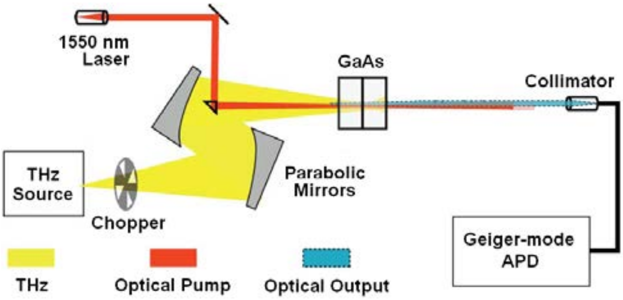

Figure 6.3: Sketch of the experimental setup of the photon-counting receiver presented in [12].

By using a WGMR as a non-linear medium, up-conversion efficiencies close to unity are theoretically possible [14]. A *NEP* of 1.6 fW/$\sqrt{\text{Hz}}$ with a conversion efficiency of 0.5 % is reported in [6], which outperforms the results published in [12]. In WGMRs, the mixing takes place if the phase matching, that is explained below, is satisfied and if sum or difference frequencies lie in another WGM. The interaction can be achieved in two ways: irradiating the THz signal just at the edge of an optical WGMR (single-resonant receiver): or by exciting another WGM at the THz frequency together with the optical mode (double-resonant receiver).

- Single-resonant receiver

In this receiver, only the optical signal excites a WGM. The only restriction is that the generated sidebands must lie in WGM resonances, that is

$$\omega_{THz} = N\Omega \tag{6.5}$$

where N is an integer number greater than zero and Ω is the FSR. If no further requirements are taken into account, the non-linear process becomes very inefficient, since it is restricted to a region smaller than wavelength [15] where optical WGM and THz signal overlap. In this case, it is said that the process is not phase-matched.

For the sum frequency generation (SFG), also called as up-conversion, in which $\omega_1 = \omega_2 + \omega_3$, it is said that the phase-matching condition is fulfilled if the wave numbers k_1, k_2, and k_3 satisfy the following

$$\Delta k = k_1 - k_2 - k_3 = 0 \tag{6.6}$$

where the wave number is defined as $k_i + \sqrt{\varepsilon_r}\omega_i/c_0$ and losses are not taken into account. Because of the dispersion, Ω changes with frequency as permittivity (normally, $\varepsilon_{r,1} > \varepsilon_{r,2}, \varepsilon_{r,3}$). This must be taken into account in both eqs. (6.5) and (6.6). For this kind of receiver, it is difficult to achieve phase-matching, which leads to a low conversion efficiencies. It is still possible by choosing the proper propagation directions of the different waves for anisotropic non-linear crystals [15]. A sensitivity of -145dBm/Hz is reported in [16].

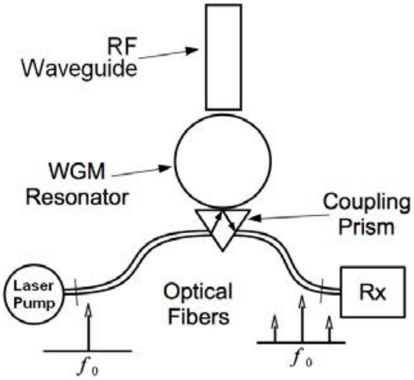

Figure 6.4: Sketch of the single-resonant receiver.

In [16], Ilchenko et al. achieved a sensitivity of -145 dBm/Hz with a conversion efficiency of 0.5 % (≈ -23 dB) for an operating frequency of 35 GHz and a FWHM of 10 MHz. The received thermal noise floor is $k_B T = -174$ dBm. Authors argue that it is possible to increase the sensitivity up to -170.5 dBm/Hz by reducing the relative intensity noise (RIN) in the photodiode. It could be done by adding a notch filter that removes the optical carrier, so only the sideband arrives to the photodetector. By doing so, the difference between sensitivity and thermal noise floor would be smaller to the photon-number conversion efficiency: Photon-counting is possible if the conversion efficiency is improved.

- Double-resonant receiver

In a double-resonant receiver, the phase matching condition is fulfilled, so the THz signal and optical pump overlap propagates around the resonator in WGMs. This allows theoretical conversion efficiencies close to unity [14]. In this thesis, the use of DRW antennas is proposed for efficient coupling of the THz signal into a WGM inside the resonator for such frequencies where phase matching condition is satisfied.

In [17], a proposal of a room-temperature sub-terahertz photon counting receiver is shown. It converts the received signal into optical domain by using a WGMR made of lithium niobate ($LiNbO_3$) (Fig. 6.5) on which the THz signal, the optical pump and the up-converted signal excites a WGM. Since the laser noise floor could outgrow the sideband THz signal, a brass filter is used between the laser source and the prism.

6.2 DRW antenna as a coupler to a WGMR

As shown in the previous subsection, efficient coupling of THz power into a WGM inside the resonator is critical for achieving photon-counting. In this subsection, DRW antennas are used for coupling to a spherical and a discoidal $LiNbO_3$ resonator. Fig. 6.6 sketches the measurement setup for measuring the spectrum of the reflected signal in the coupling. A CW photomixer-based terahertz source is pigtailed with a 75-110 GHz DRW antenna. The antenna emitter is a 1550 nm 3-period *n-i-pn-i-p* photodiode with a log-periodic antenna (see Chapter 2). The dielectric antenna is placed at a distance of 80 μm of a WGMR. The power that is not absorbed by the resonator is collected in a parabolic

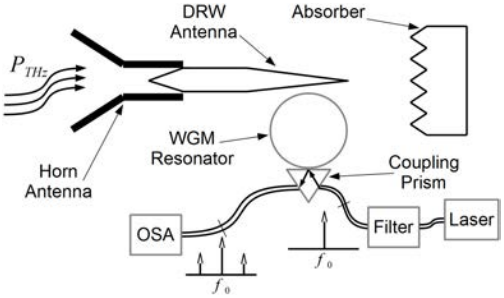

Figure 6.5: Receiver scheme. The sub-thz field is received in and antenna and then coupled to a DRW. Then, it is coupled to a WGMR via a DRW antenna. The laser pump and the up-converted signal is coupled through a prism. A Bragg filter is used for decreasing the laser noise floor, which could outgrow the sideband in the detector.

mirror and then focused to a detector by a second parabolic mirror. For both measurements, only the fundamental mode is propagating inside the DRW.

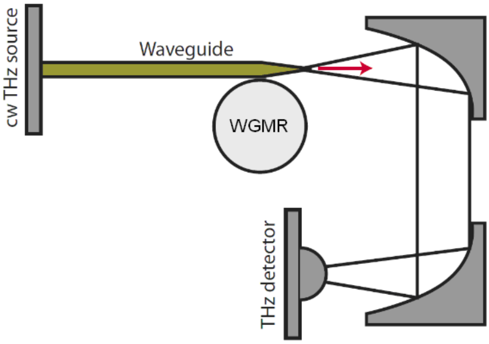

Figure 6.6: Schematic of the coupling setup. A GaAs DRW antenna is placed close to the WGMR.

- Spherical resonator

Fig. 6.7 shows the spectrum of the detected signal, normalized to a reference measurement without resonator. Two different mode families are excited. Insets shows the simulated E-field amplitude inside the resonator for both families. A photo of the WGMR is also displayed. It is a LiNbO$_3$ sphere of 5 mm diameter. It is placed approximately 150 μm off the DRW antenna. A FSR of 6 GHz is obtained.

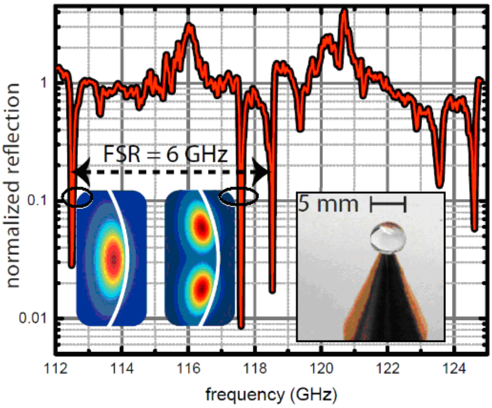

Figure 6.7: Normalized transmission spectrum of whispering gallery modes exited in a sapphire sphere by a DRW antenna. The spectrum shows at least two different family of modes, which repeats with a FSR of ≈ 6 GHz. The linewidth of the modes is approximately 100 MHz, which corresponds to a quality factor $Q > 1000$. Insets shows the simulated intensity cross sections of the resonator for the two families of modes.

- Discoidal resonator

Fig. 6.8 shows the measured and simulated spectra of the WGMR show in the inset. It is a LiNbO$_3$ disk with an outer radius of 2.95 mm and 0.35 mm high. Same DRW antenna as for the spheric resonator is used. The distance between the resonator and the antenna is 80 μm approximately.

The E-field distribution was calculated via full-wave simulation. It is shown in Fig 6.9 for 77.2 GHz (Fig. 6.9a) and 81.8 GHz (Fig. 6.9b). Both frequencies corresponds to two disk resonances, identified as $R1$ and $R2$ in Fig. 6.8. It can be seen how the modes degrades at higher frequencies. Other modes, such as bouncing ball modes, appear, which gives the triangular shape to the field distribution (Fig. 6.9b).

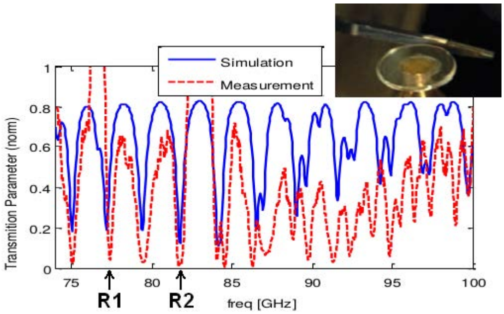

Figure 6.8: Simlated (blue) and measured (red) spectra of a discoidal WGMR.

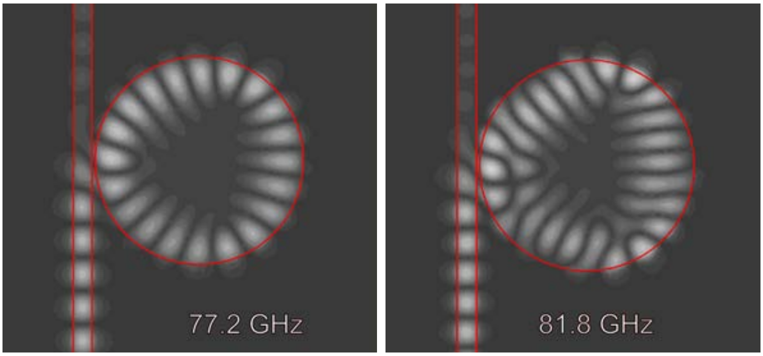

(a) **(b)**

Figure 6.9: Simlated E-field distribution at 77.2 GHz (a) and 81.8 GHz (b). The DRW antenna supporting only its fundamental mode efficiently couples it to the WGMR. A WGM is then generated inside the resonator. The limits of both the rod and the resonator are marked with red lines.

6.3 Conclusions

The use of DRW antennas as an efficient coupler of WGM in spherical and discoidal $LiNbO_3$ resonators has been validated. Full-wave simulations allow to obtain E-field distributions that confirms the type of excited modes. Experiments confirm the resonance frequencies of simulated modes.

As explained in Subsection 6.1, when exciting WGM the conversion efficiency increases, which would enable to achieve photo-counting up-converters at room temperature. Such a high sensitivity would be welcome in radioastronomy applications, where detected mm and sub-mm signals are at very low power levels. In [17], we proposed the use of the double-resonance receiver for detecting the B-mode of cosmic microwave background (CMB) [18,19]. This would offer an alternative way to detect gravitational waves. They were theoretically predicted in the General Theory of Relativity of Albert Einstein and detected in 2016 for the very first time [20].

WGMRs have many applications in the THz frequencies, which are interesting from the point of view of engineering. Some systems components can be implemented, such as filters, electrically controlled switches and modulators, among others [21]. Due to its high Q they can be used as a sensors for liquids and gas spectroscopy, since a small change in the surrounding environment affects the coupling between the rod and the resonator, which shifts the resonant frequency.

6.4 References

[1] C. Garrett, W. Kaiser, and W. Bond, “Stimulated emission into optical whispering modes of spheres,” *Physical Review*, vol. 124, no. 6, p. 1807, 1961.

[2] S. Preu, S. I. Schmid, F. Sedlmeir, J. Evers, and H. G. Schwefel, “Directional emission of dielectric disks with a finite scatterer in the THz regime,” *Optics Express*, vol. 21, no. 14, pp. 16 370–16 380, 2013.

[3] G. Carpintero, L. E. García-Muñoz, H. L. Hartnagel, S. Preu, and A. V. Räisänen (Editors), *Semiconductor Terahertz Technology Devices and Systems at Room Temperature Operation.* Wiley, 2015.

[4] A. Rivera-Lavado, S. Preu, L. E. García-Muñoz, A. Generalov, J. Montero-de Paz, G. Dohler, D. Lioubtchenko, M. Mendez-Aller, F. Sedlmeir, M. Schneidereit *et al.*, “Dielectric rod waveguide antenna as THz emitter for photomixing devices,” *IEEE Transactions on Antennas and Propagation*, vol. 63, no. 3, pp. 882–890, 2015.

[5] I. S. Grudinin, V. S. Ilchenko, and L. Maleki, “Ultrahigh optical q factors of crystalline resonators in the linear regime,” *Physical Review A*, vol. 74, no. 6, p. 063806, 2006.

[6] D. V. Strekalov, A. A. Savchenkov, A. A. Matsko, and N. Yu, “Towards microwave photon counting via frequency up-conversion,” in *2008 33rd International Conference on Infrared, Millimeter and Terahertz Waves*, 2008, pp. 1–2.

[7] B. S. Karasik, W. R. McGrath, H. G. LeDuc, and M. E. Gershenson, “A hot-electron direct detector for radioastronomy,” *Superconductor Science and Technology*, vol. 12, no. 11, p. 745, 1999.

[8] A. Sergeev, V. Mitin, and B. Karasik, “Ultrasensitive hot-electron kinetic-inductance detectors operating well below the superconducting transition,” *Applied Physics Letters*, vol. 80, no. 5, pp. 817–819, 2002.

[9] R. Schoelkopf, S. Moseley, C. Stahle, P. Wahlgren, and P. Delsing, “A concept for a submillimeter-wave single-photon counter,” *IEEE*

transactions on Applied Superconductivity, vol. 9, no. 2, pp. 2935–2939, 1999.

[10] A. Semenov, A. Engel, K. Il'in, G. Gol'Tsman, M. Siegel, and H.-W. Hübers, "Ultimate performance of a superconducting quantum detector," *The European Physical Journal Applied Physics*, vol. 21, no. 3, pp. 171–178, 2003.

[11] M. J. Khan, J. C. Chen, and S. Kaushik, "Optical detection of terahertz radiation by using nonlinear parametric upconversion," *Optics letters*, vol. 32, no. 22, pp. 3248–3250, 2007.

[12] M. J. Khan, J. C. Chen, Z.-L. Liau, and S. Kaushik, "Ultrasensitive, room temperature detection of THz radiation using nonlinear parametric conversion," *IEEE Journal of Selected Topics in Quantum Electronics*, vol. 17, no. 1, pp. 79–84, 2011.

[13] V. G. Dmitriev, G. G. Gurzadyan, and D. N. Nikogosyan, *Handbook of nonlinear optical crystals.* Springer, 2013, vol. 64.

[14] A. Matsko, D. Strekalov, and N. Yu, "Sensitivity of terahertz photonic receivers," *Physical Review A*, vol. 77, no. 4, p. 043812, 2008.

[15] P. E. Powers, *Fundamentals of nonlinear optics.* CRC Press, 2011.

[16] V. Ilchenko, J. Byrd, A. Savchenkov, P. Koonath, A. Matsko, D. Seidel, and L. Maleki, "Whispering-gallery mode based photonic rf receiver," in *IEEE MTT-S International Microwave Symposium Digest (MTT).* IEEE, 2010, pp. 744–747.

[17] G. Santamaria-Botello, A. Rivera-Lavado, L. E. García-Muñoz, and D. Segovia-Vargas, "Room-temperature photon-counting receiver scheme for cosmic microwave background polarization measurements," in *2016 Global Symposium on Millimeter Waves (GSMM) & ESA Workshop on Millimetre-Wave Technology and Applications*, 2016, pp. 1–4.

[18] A. Polnarev, "Polarization and anisotropy induced in the microwave background by cosmological gravitational waves," *Soviet Astronomy*, vol. 29, pp. 607–613, 1985.

[19] U. Seljak, "Measuring polarization in the cosmic microwave background," *The Astrophysical Journal*, vol. 482, no. 1, p. 6, 1997.

[20] B. Abbott, R. Abbott, T. Abbott, M. Abernathy, F. Acernese, K. Ackley, C. Adams, T. Adams, P. Addesso, R. Adhikari *et al.*, “Observation of gravitational waves from a binary black hole merger,” *Physical review letters*, vol. 116, no. 6, p. 061102, 2016.

[21] V. S. Ilchenko and A. B. Matsko, “Optical resonators with whispering-gallery modes-part ii: applications,” *IEEE Journal of Selected Topics in Quantum Electronics*, vol. 12, no. 1, pp. 15–32, 2006.

CHAPTER 7

SUMMARY AND CONCLUSIONS

The main goal of this thesis was the development of room-temperature, small-sized, broadband, efficient, low-noise, cost-affordable and high power THz sources. For this, a novel alternative to dielectric lenses has been deeply studied. It has been demonstrated how its emission efficiency (see Section 1.4.1) is close to electrically-large lenses. When consider its unitary costs they become an appealing alternative, specially for consumed-oriented applications.

DRW antennas can be ultra-wideband, when embedding dielectric planar lens into them. Despite not a successful manufacturing method for THz samples has been found, its complexity indicates higher costs per unit than conventional DRW antennas. Nevertheless, due to the possibility of manufacturing a large amount of lens-based rods at the same time unitary cost can predictably be much smaller than for silicon lenses.

Lenses have better emission efficiencies than DRW antennas only when they are electrically large. In such a case, DRW antennas are preferable to microlenses when considering arrays of AEs. For supporting all these statements, both a theoretical studies and full-wave simulation were done. The effect of semi-infinite subtrates and infinite dielectric slabs in the radiation properties of AEs has been considered.

Arrays of DRW antennas enables both high power generation and beam forming when a proper phase shifter is integrated in the DRW. A CNT-based phase shifter has been proposed.

7.1 Research stays

The experimental work described in this thesis was done mainly in three different European universities:

- Chair of Applied Physics, Fiedrich-Alexander Universität Erlangen-Nürnberg, Erlangen, Germany.
- Department of Radio Science and Enginnering labs (MilliLab), at Aalto University, Espoo, Finland.
- GREMA group THz lab, at Carlos III University of Madrid, Madrid, Spain.

during the following stays:

- Three weeks short visit at Fiedrich-Alexander Universität Erlangen-Nürnberg (February 2012).
- Four months exchange visit at Aalto University (from February 2013 to June 2013).
- Six months exchange visit at Aalto University (from February 2014 to August 2014). Granted by Newfocus exchange visit grant form European Science Foundation (ESF) research networking programme.
- Two weeks short visit at Aalto University (May 2015). Granted by Newfocus short-stay grant form ESF research networking programme.

7.2 Future lines

In this section, a list of proposed future research lines raised while working for this Ph.D dissertation is discussed.

- *Related with arrays of photomixing sources:*

- Assembly of an 1x3 array of DRW antennas fed by AEs (Fig. 7.1). The first attempt failed because two of three AEs were defective. The measured photocurrent was below 50 nA and below the noise level for these two devices, so assembly was stopped before gluing the optical fibers (Section 3.2). Two different attempts to improve the biasing connection were done. Same photocurrent levels were obtained.

(a) (b)

Figure 7.1: Assembled 1x3 DRW antenna array before adding the foam disc (a) and after doing biasing connections with silver ink (b).

- The wafer of photoconductive devices (see Section A.3) suffered from many delays during its manufacture, which made it impossible to have measurements done for this thesis. Two experiments are of particular interest for this research line: the 2D arrays of bow tie antennas and the 1x4 arrays of log-periodic AE. Single elements are also provided for comparing the array radiation pattern measurements with those calculated using the array factor.

- *Related with CNTs:*

- To determine the interaction mechanism between the tungsten lamp and the layer of CNT. It could be possible to do so by chopping the optical pump at a specific frequency (to be experimentally determined). By doing so, it would be possible to analyze phase changes in an S_{21} measurement setup (see Section 3.4). Slow changes in the DRW phase when chopping would suggest a thermal interaction. Fast changes would point to a photonic mechanism.
- To characterize the propagation constant change with incident density of power (or temperature) of DRW loaded with a thin layer of CNT by full wave simulations and propagation constant measurements.
- To validate the concept of beam forming with DRW antenna arrays by using CNT-based phase shifters. The 1x4 array designed and manufactured (Appendix A, Section A.3) is intended as a proof-of-concept of a 1D scanning array. They are design to be suitable for the assembly process described in Section 3.2.

- *Related with DRW antennas:*

- To manufacture and measure a lens-based DRW antenna in the sub-THz and THz frequencies. If a silicon powder with grains much smaller than wavelength can be obtained, it could be possible to mix them with epoxy glues. It could allow us to control the permittivity of the rod by modifying the density of silicon grains.

Appendices

APPENDIX A

LITHOGRAPHIC MASKS

This section describes the lithographic masks either processed or designed during this Ph.D. dissertation.

A.1 Mask of AE arrays and dielectric horns

This mask was designed by Belen Andrés Garcia as a part of her thesis work. It was processed in Fiedrich-Alexander Universität Erlangen-Nürnberg cleanroom during my short-visit there. It contains submasks for two different sets of experiments: different configurations of AEAs and well spaced AEs for doing dielectric horn antennas by etching around them.

AEs are *n-i-pn-i-p* devices (see Section 2.2). They are manufactured with two different sizes of log-periodic antennas. There is a total of three different arrays configurations:

- Rectangular array of 5x5 AE with large log-spiral antennas. Both horizontal and vertical pitch between elements is 320 μm.
- Array of 5x5 AE with small log-spiral antennas. Horizontal and vertical pitch is 145 μm.

- Array of 3x3 AE with small log-spiral antennas (Fig. A.1b). Horizontal and vertical pitch is 145 μm. Biasing pads are far from the array for assembly purposes. This array is design to be illuminated by an array of 3x3 fibers with phase shifters (see Section 2.3).

Measurements results were carried out in Fiedrich-Alexander Universität Erlangen-Nürnberg labs. They are presented in Section 2.3.

A.2 Logarithmic-periodic AE (LP5)

This design, named as *LP5* [1], was designed and processed in Fiedrich-Alexander Universität Erlangen-Nürnberg cleanroom and sent to Carlos III University of Madrid. The chip was cut splitting all devices at the Micronova Nanofabrication Centre of Aalto University in Espoo, Finland. Devices are InGaAs *n-i-pn-i-p* structures. They were grown over the InP substrate by the Materials Department of the University of Santa Barbara, California, USA.

The aim of this wafer is to reduce the limitations of the RC roll-off by reducing the devices size. Samples with a cross section of 27 μm^2, 42 μm^2, 82 μm^2 and 93 μm^2 are included in combination with log-periodic and log-spiral antennas. An additional set of experiments is included for measuring the I-V characteristics, the RF performance, the conductivity of both top and bottom contact layers and the doping concentration.

These AE prototypes were used in Carlos III University of Madrid for device packaging and DRW antenna assembly tests (see Fig. 3.13a).

A.3 Mask of photoconductive AE experiments

This mask was designed at Carlos III University of Madrid. It is a full wafer populated of different experiments. It was processed by Heinrich Hertz Institute (HHI) in Germany. It is manufactured in a InP substrate with a molecular beam epitaxy (MBE) grown of a multilayer set of LT-InAlAs/InGaAs [2]. This allows to achieves an E_{GAP} of 0.8 eV, that is, an operational wavelength 1.55 μm for the optoelectronic

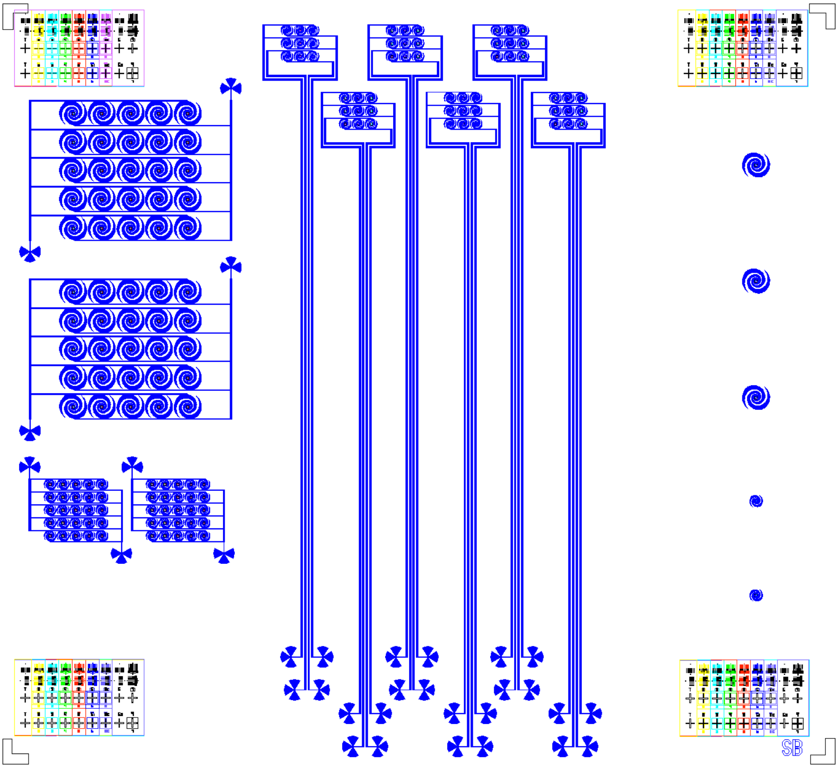

(a)

(b)

Figure A.1: Manufactured lithographic mask. Overall view (a) and detail of a 3x3 AE array (b).

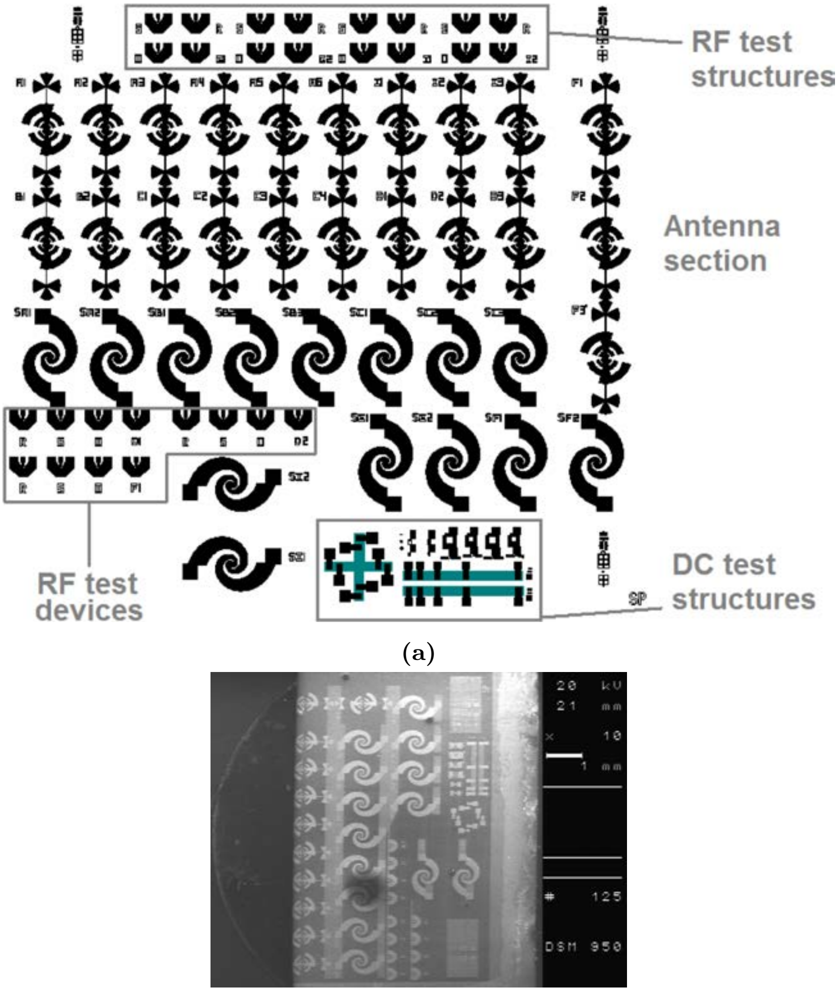

(a)

(b)

Figure A.2: Mask LP5 (a) and SEM image of part of the manufactured chip (b).

devices. Photoconductive devices are designed by HHI. The design here displayed includes the metalization layers for the antennas, bias pads, and alignment marks only.

Fig. A.3a shows the distribution of experiments in the wafer, as seen in the software *KLayout*. For ease of manufacture, wafer is divided in cells of 2 mm x 4 mm where all experiments are accommodated.

- Log-periodic AEs of different sizes: optimized for 100 GHz (starting at 50 GHz) and 200 GHz (starting at 100 GHz).
- Array of 1x4 Log-periodic AEs optimized for a frequency of 200 GHz.
- Bow tie AEs of different frequencies (100 GHz, 200 GHz, 300 GHz, 500 GHz and 1 THz).
- Bow tie AEAs of different frequencies (500 GHz, 1 THz, and 2 THz) and pitches between elements (150 μm and 300 μm, intended to be assembled with commercially available array of microlenses, see Section 2.3).
- Devices for DC characterization. Contact pads are designed taking into account the tolerances of the procedure described in Section 3.2.
- Meander dipoles of different lengths [3–5].

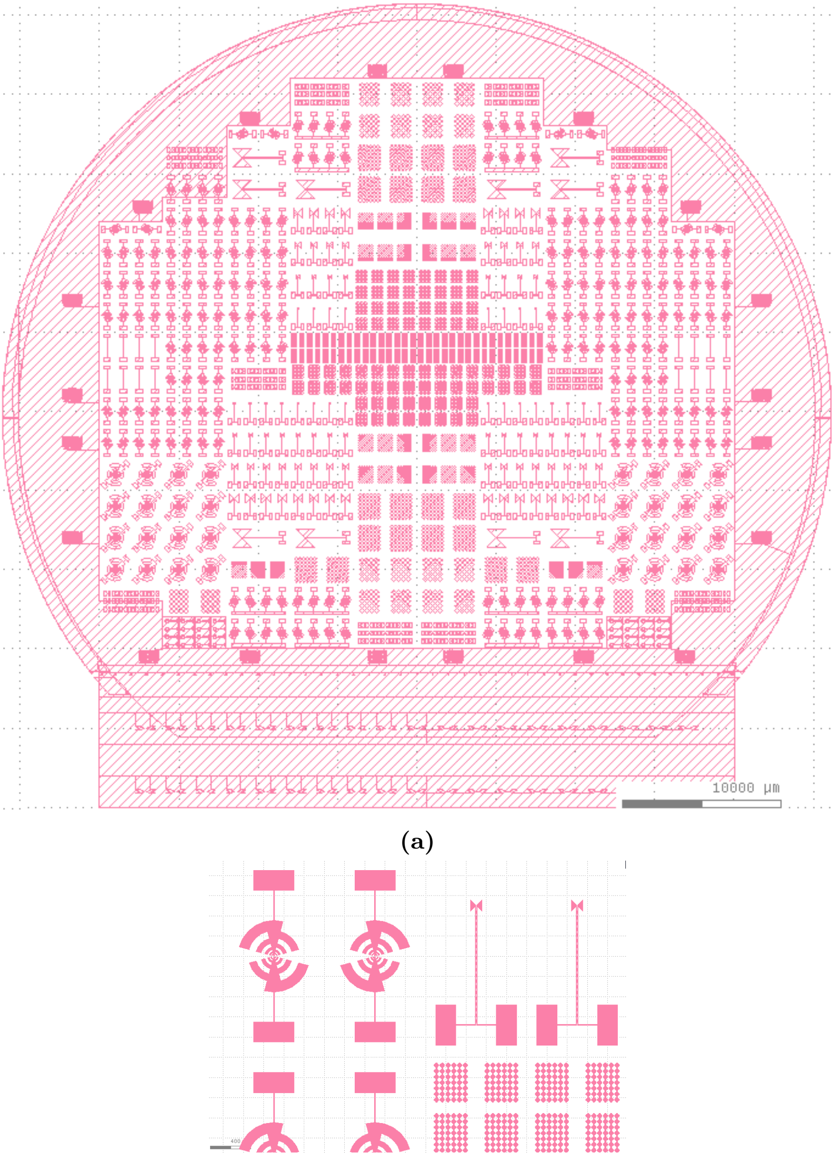

(a)

(b)

Figure A.3: Manufactured lithographic mask. Overall view (a) and detailed view showing 200 GHz log-periodic antennas, 1 THz bow ties antennas and 2 THz arrays of bow ties AEs (b)

A.4 References

[1] S. Preu, *Continuous-wave, Tunable THz n-i-pn-i-p Superlattice Photomixers and Applications.* MPL, 2009.

[2] B. Sartorius, H. Roehle, H. Künzel, M. Schlak, D. Stanze, H. Venghaus, M. Schell *et al.*, "All-fiber terahertz time-domain spectrometer operating at 1.5 μm telecom wavelengths," *Optics Express*, vol. 16, no. 13, pp. 9565–9570, 2008.

[3] T. Endo, Y. Sunahara, S. Satoh, and T. Katagi, "Resonant frequency and radiation efficiency of meander line antennas," *Electronics and Communications in Japan (Part II: Electronics)*, vol. 83, no. 1, pp. 52–58, 2000.

[4] K. Moon, H. Han, and I. Park, "Terahertz folded half-wavelength dipole antenna for high output power," in *International Topical Meeting on Microwave Photonics, 2005. MWP 2005.*, 2005, pp. 301–304.

[5] D. Segovia-Vargas, D. Castro-Galán, L. E. García-Muñoz, and V. Gonzalez-Posadas, "Broadband active receiving patch with resistive equalization," *IEEE Transactions on Microwave Theory and Techniques*, vol. 56, no. 1, pp. 56–64, 2008.

APPENDIX B

DRW MANUFACTURE

This section describes the manufacture process of DRW and DRW antennas used in Chapters 4, 5, and 6. They were developed at Micronova Nanofabrication Centre of Aalto University in Espoo, Finland.

B.1 Solid DRW antennas

The manufacture of DRW antennas on both silicon and GaAs substrates has been done by using a dicing saw (Fig. B.1). Next, the manufacturing of a rod of length L_{TAPER} and width W_{ROD} (see Fig. 4.8) is discussed.

This device is a computer-controlled tool. It is only possible to do straight cuts, so no concave shapes are achievable. A pith between a specified number of cuts can be programmed, since in-plane displacement are precise-enough. Fig. B.1 inset shows the cutting pattern. First, the red cuts are doing by programing the pitch P_R.

The wafer holder can be rotated a specific amount ($\theta_1 = \arctan(W_{ROD}/L_{TAPER})$, counterclockwise), but this feature is not sufficiently precise for sharp tips. Once the red cuts have been done, it is

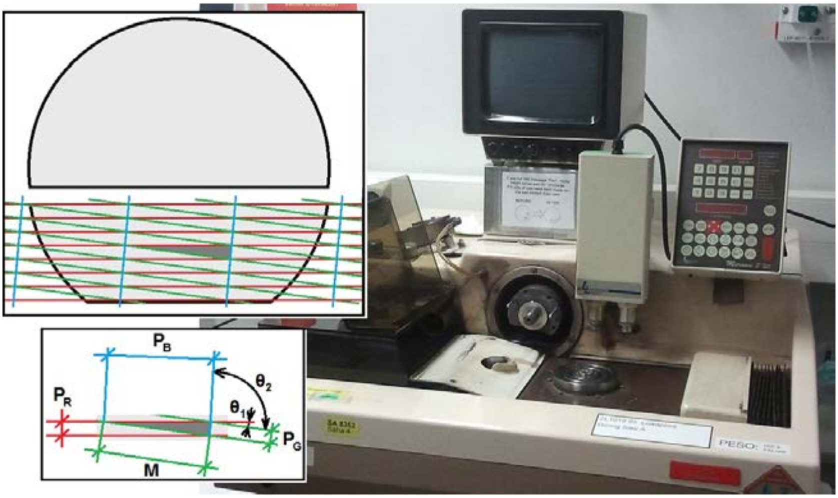

Figure B.1: Computerized dicing saw. The cutting pattern is shown in the upper inset. Dashed area shows a DRW antenna. Pitches, dimensions and angles are detailed in the lower inset.

possible to use them as alignment marks. By using the microscope cameras, a visual inspection allows us to determine the actual rotated angle by measuring the distance between two red cuts M. Successive compensation or the rotation angle allows us to reach the needed precision. Then, the green cuts are done after programming the pitch P_G.

Finally, blue lines with the cutting plane of the dicing saw by rotating the sample clockwise ($\theta_2 = 90^\circ + \theta_1/2$). Intersections between red and green cuts can be used for checking visually the rotated angle. All cuts marked in blue are done by programming the pitch P_B.

B.2 Lens-based DRW antennas

Lens-based DRW antennas requires to have two regions of different permittivities. This can be achieved by either using two different materials or by doing porosities in a solid DRW antenna. Fig. B.2 shows low-frequency prototypes manufactured with both strategies.

During this thesis, we tried to manufacture lens-based DRW antennas

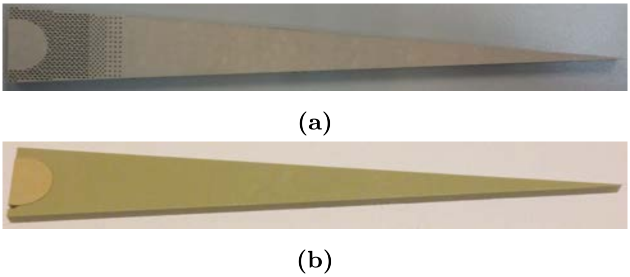

Figure B.2: Manufactured lens-based DRW antenna prototypes. In (a), permittivity around the lens is reduced by drilling holes. In (b), two materials of different permittivities (polypropylene and AD-1000) were used.

by doing porosities in a silicon rod. Porous silicon is a well-studied material [1,2] due to its many potential applications [2]. Its manufacturing procedures have been deeply studied for controlling size and morphology of pores [1]. Fig. B.3 sketches the etching process. A solid silicon wafer is placed between an aluminium ring and a Teflon recipient filled with a disolution of hydrogen fluoride (HF) (25 %) and water (75 %). The recipient has a window so the acid is in contact with the silicon. A Pt electrode is placed inside the acid. The Al plate acts as a second electrode so a voltage can be applied between both. By using a mask, the desired pattern is projected down the wafer for achieving a selective etching process.

The etching process was rather slow (about 1-2 μm/min) and not uniform. Fig. B.4 shows a picture of the sample after 10 minutes of etching. Both insets shows SEM pictures of the cross-section fro both the area intended to be porous (a) and solid (b). Since limits between both areas are not sharp enough, a protective mask (e.g. isolating silicon nitride, conducting platinum or gold, etc) should be used in the top surface. Not a functional sample was obtained during the realization of this thesis.

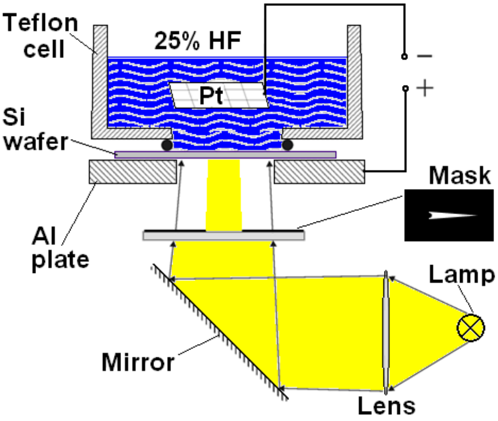

Figure B.3: Sketch of the HF etching process.

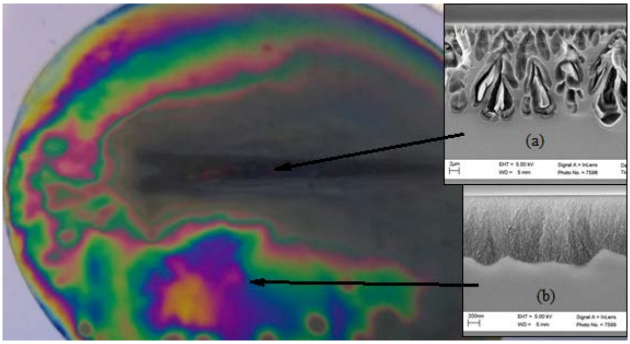

Figure B.4: Etching process result. Inset shows SEM pictures of the cross-section of the porous (a) and solid (b) regions. Scale of (a) is 2 μm. Scale of (b) is 200 nm.

B.3 References

[1] G. X. Zhang, “Porous silicon: morphology and formation mechanisms,” in *Modern Aspects of Electrochemistry.* Springer, 2006, ch. 2, pp. 65–133.

[2] Z. Gaburro, N. Daldosso, and L. Pavesi, “Porous silicon,” *Encyclopedia of Condensed Matter Physics*, pp. 391–401, 2005.

PUBLICATIONS

The work developed in this Ph.D. dissertation has led to several journals, and conference contributions. The complete list is detailed below.

Journal Papers

Related to chapter 1:

- L. E. García-Muñoz, E. Ugarte-Munoz, J. Montero-de Paz, A. Rivera-Lavado, and D. Segovia-Vargas, “Anomalous behavior in the radiation patterns,” *IEEE Transactions on Antennas and Propagation*, vol. 61, no. 2, pp. 973–976, 2013

Related to chapter 2:

- A. Rivera-Lavado, L. E. García-Muñoz, G. Dohler, S. Malzer, S. Preu, S. Bauerschmidt, J. Montero-de Paz, E. Ugarte-Muñoz, B. Andrés-García, V. Izquierdo-Bermúdez *et al.*, “Arrays and new antenna topologies for increasing thz power generation using photomixers,” *Journal of Infrared, Millimeter, and Terahertz Waves*, vol. 34, no. 2, pp. 97–108, 2013
- N. Khiabani, Y. Huang, L. E. García-Muñoz, Y.-C. Shen, and A. Rivera-Lavado, “A novel sub-thz photomixer with nano-trapezoidal electrodes,” *IEEE Transactions on Terahertz Science and Technology*, vol. 4, no. 4, pp. 501–508, 2014

Related to chapter 1 and 2:

- G. H. Dohler, L. E. García-Muñoz, S. Preu, S. Malzer, S. Bauerschmidt, J. Montero-de Paz, E. Ugarte-Munoz, A. Rivera-Lavado, V. Gonzalez-Posadas, and D. Segovia-Vargas, "From arrays of thz antennas to large-area emitters," *IEEE Transactions on Terahertz Science and Technology*, vol. 3, no. 5, pp. 532–544, 2013

Related to chapter 4:

- A. Rivera-Lavado, L. E. García-Muñoz, S. Preu, D. Lioubtchenko, S. Llorente-Romano, A. García-Lamperez, D. Segovia-Vargas, and A. V. Räisänen, "Planar lens-based ultra-wideband dielectric rod waveguide antenna," *To be submitted*, 2016

Related to chapter 4 and 6:

- A. Rivera-Lavado, S. Preu, L. E. García-Muñoz, A. Generalov, J. Montero-de Paz, G. Dohler, D. Lioubtchenko, M. Mendez-Aller, F. Sedlmeir, M. Schneidereit *et al.*, "Dielectric rod waveguide antenna as thz emitter for photomixing devices," *IEEE Transactions on Antennas and Propagation*, vol. 63, no. 3, pp. 882–890, 2015

Related to chapter 5:

- A. Rivera-Lavado, L. E. García-Muñoz, A. Generalov, D. Lioubtchenko, K.-A. Abdalmalak, S. Llorente-Romano, A. Garcia-Lamperez, D. Segovia-Vargas, and A. V. Räisänen, "Design of a dielectric rod waveguide antenna array for millimeter waves," *Journal of Infrared, Millimeter and Terahertz Waves*, 2016

Conference contributions

- L. E. García-Muñoz, J.-M. de Paz, A. Rivera-Lavado, I. Mayorga, R. Gusten, A. Generalov, D. Lioubtchenko, P. Gallardo, C. de Dios, R. Criado *et al.*, "Thz antenna array based on photomixers for radioastronomy applications," in *7th European Conference on Antennas and Propagation (EuCAP)*, 2013, pp. 450–453
- L. E. García-Muñoz, G. H. Dohler, J. Montero-de Paz, E. Ugarte-Munoz, A. Rivera-Lavado, S. Preu, S. Malzer, S. Bauerschmidt, V. Gonzalez-Posadas, and D. Segovia-Vargas, "New device for continuous-wave thz emission: Large area emitter," in *7th European Conference on Antennas and Propagation (EuCAP)*, 2013, pp. 529–532
- L. E. García-Muñoz, S. Preu, A. Rivera-Lavado, S. Malzer, G. H. Dohler, A. Generalov, M. Mendez Aller, D. Lioubtchenko, A. V. Räisänen, and D. Segovia Vargas, "New antenna topology coupled to a new waveguide structure for thz radiation and propagation," in *38th International Conference on Infrared, Millimeter, and Terahertz Waves (IRMMW-THz)*, 2013, pp. 1–1
- A. V. Räisänen, A. A. Generalov, D. V. Lioubtchenko, A. Rivera-Lavado, M. Mendez-Aller, L. E. García-Muñoz, D. Segovia-Vargas, and S. Preu, "Dielectric rod waveguide as an enabling technology for thz frequencies," in *8th European Conference on Antennas and Propagation (EuCAP)*, 2014, pp. 2638–2639
- A. Rivera-Lavado, S. Preu, L. E. García-Muñoz, A. Generalov, J. Montero-de Paz, G. H. Dohler, D. Lioubtchenko, M. Mendez-Aller, S. Malzer, D. Segovia-Vargas *et al.*, "Ultra-wideband dielectric rod waveguide antenna as photomixer-based thz emitter," in *8th European Conference on Antennas and Propagation (EuCAP)*, 2014
- A. V. Räisänen, D. Generalov, Andrey Lioubtchenko, , A. Rivera-Lavado, M. Mendez Aller, L. E. García-Muñoz, D. Segovia-Vargas, and S. Preu, "Dielectric rod waveguide antennas and their applications at mm-wave and THz frequencies," in *Global Symposium on Millimeter Waves GSMM2014*, 2014, best paper award

- M. Mendez-Aller, L. E. García-Muñoz, H. Schwefel, F. Sedlmeir, M. Schneidereit, A. Rivera-Lavado, and D. Segovia-Vargas, "Room temperature receiver based on whispering gallery mode resonators for radio astronomy applications," in *European Optical Society (EOS) Toptical Meeting on THz Science and Technology*, 2014
- L. E. García-Muñoz, J. Montero-de Paz, E. Ugarte-Munoz, A. Rivera-Lavado, M. Mendez-Aller, D. Segovia-Vargas, G. H. Dohler, S. Preu, S. Malzer, S. Bauerschmidt *et al.*, "On the finite semiconductor thickness effect applied to large area emitters devices for thz radiation," in *44th European Microwave Conference (EuMC)*, 2014, pp. 814–817
- M. Mendez-Aller, L. E. García-Muñoz, A. Rivera-Lavado, and D. Segovia-Vargas, "Optimum sub-THz room temperature radio astronomy receiver," in *URSI2014*, 2014
- A. Rivera-Lavado, J. Montero-de Paz, G. Dohler, L. E. García-Muñoz, S. Preu, S. Malzer, S. Bauerschmidt, and D. Segovia-Vargas, "An antenna-free device for continuous-wave thz emission: Vertical large area emitter," in *9th European Conference on Antennas and Propagation (EuCAP)*, 2015, pp. 1–2
- L. E. García-Muñoz, S. Preu, A. Rivera-Lavado, R. Guzman, C. Gordon, V. Corral, G. Carpintero, M. Salazar, and D. Segovia-Vargas, "Unlocking THz communication systems combining electronic and photonic technologies," in *URSI2015*, 2015
- A. Rivera-Lavado, L. E. García-Muñoz, D. Lioubtchenko, S. Preu, D. Segovia-Vargas, and A. V. Räisänen, "Increasing the bandwidth of dielectric rod waveguide antennas for terahertz applications," in *40th International Conference on Infrared, Millimeter, and Terahertz waves (IRMMW-THz)*, 2015, pp. 1–1
- A. Rivera-Lavado, S. Preu, L. E. García-Muñoz, A. Generalov, J. Montero-de Paz, G. Döler, D. Lioubtchenko, M. Mendez-Aller, S. Malzer, D. Segovia-Vargas, and A. V. Räisänen, "Array of dielectric rod waveguide antennas for millimeter-wave power generation," in *EuMW2015*, 2015

- G. Santamaría-Botello, A. Rivera-Lavado, L. E. García-Muñoz, and D. Segovia-Vargas, "Room-temperature photon-counting receiver scheme for cosmic microwave background polarization measurements," in *Global Symposium on Millimeter Waves GSMM2016*, 2016, best student paper award

- D. Lioubtchenko, A. Rivera-Lavado, I. Nefedova, I. Anoshkin, L. E. García-Muñoz, and A. V. Räisänen, "Novel type of phase shifter based on DRW loaded with CNT layers," in *10th European Conference on Antennas and Propagation (EuCAP)*, 2016

- D. Lioubtchenko, A. Rivera-Lavado, I. Nefedova, I. Anoshkin, L. E. García-Muñoz, and A. V. Räisänen, "Optically controlled millimetre wave phase shifter," in *Global Symposium on Millimeter Waves GSMM2016*, 2016

- G. Santamaría-Botello, A. Rivera-Lavado, S. Preu, F. Sedlmeir, D. Lioubtchenko, H. Schwefel, D. Segovia-Vargas, and L. E. García-Muñoz, "Sub-THz photon counting receiver working at room temperature for polarization measurements of the cosmic microwave background radiation," in *10th European Conference on Antennas and Propagation (EuCAP)*, 2016

- G. Santamaría-Botello, K. Atia-Abdalmalak, A. Rivera-Lavado, J. M. Serna-Puente, F. Tercero, J. A. Lopez-Perez, F. Colomer, J. A. Lopez-Fernandez, L. E. García-Muñoz, and D. Segovia-Vargas, "Radioastronomy instrumentation projects at Universidad Carlos III de Madrid," in *URSI2016*, 2016

- A. Rivera-Lavado, L. E. García-Muñoz, and D. Segovia-Vargas, "Terahertz dielectric rod waveguide antennas: developments and applications," in *URSI2016*, 2016

About the Author

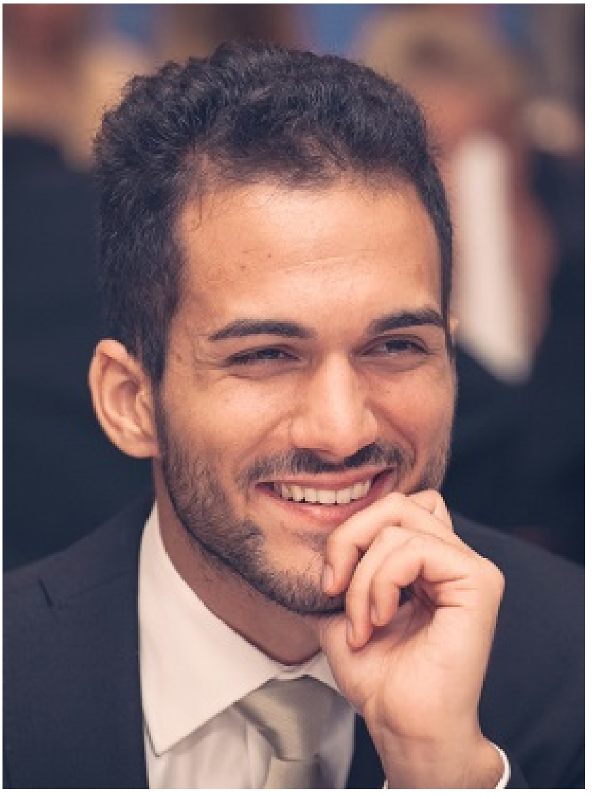

Alejandro Rivera-Lavado was born in Madrid, Spain, on Oct 24, 1984. He received the Engineer degree in telecommunications from Carlos III University, Madrid, Spain, in 2010, and the Master degree in Multimedia and Communications from Carlos III University, Madrid, Spain, in 2012. Since 2007 he is working with the Group of Radiofrequency, Electromagnetism and Antennas at Carlos III University. He has authored or co-authored 7 JCR journal papers and 27 conference contributions. He has been teacher of different Grade and Master level subjects at the university since 2010. His research lines are dielectric lenses, terahertz antennas and low-loss terahertz transmission lines.